UNIVERSITY OF TEXAS AT ARLINGTON

DEPARTMENT OF PHYSICS

PH.D. DISSERTATION

A Measurement of Electron-Neutrino Cross Section at MiniBooNE

By:

SEPIDEH SHAHSAVARANI

Advisor:

DR. AMIR FARBIN

Committee Members:

DR. HALEH HADAVAND

DR. JONATHAN ASSADI

DR. ZDZISLAW MUSIELAK

DR. BENJAMIN JONES

12-APRIL-2018

Acknowledgement

Well, I cannot believe it is finally over.

First and foremost, Mom and Dad, I cannot thank you enough for the emotional and financial support and love that you have given me without question over the years. Dad, I finally got my PhD in physics as I promised you when I choose it as my major in the university. I cannot forget the day that you drove me to Mashhad over the night to help me moving to the city far from the home. Mom, please still keep me on your prayer, without it I never achieve my goals. I still call you and say the same sentence "pray for me". Mom, I know, nothing is better than going home to family and eating good food and talking to the most lovely people in the world, but I left home with the search of future and make you proud at some point.

Arash jaan, I received your love when I really needed. Thanks for being so patient and kind to me. Life is better with the best friend that is why I married mine, I am so glad I have you next to me.

Jonathan Assadi, you are probably the only person who taught me neutrino physics. I met you first time at Fermilab in the neutrino lecture you presented. The UT Arlington was lucky to have you as the professor. More than others, I think, I was the luckiest one to see you here. I cannot thank you enough for all the help. I am finally graduating, you are off the hook, but I still plan to email and bug you.

And last, but certainly not least, to my advisor, Amir, thank you for guiding me on this path, allowing me to be goofy sometimes, and always encouraging me in everything that I have done. I never forget all of the help I have received from you.

Contents

List of Figures

List of Tables

1 Abstract

1.1 Plan and aim of Dissertation

This dissertation aims to make a electron neutrino elastic scattering cross section measurement on carbon. The previous measurements of this cross section was performed by counting experiment, where the neutrino electron sample counted in only signal region. In this dissertation the cross section is measured by χ^2-based analysis where the background only region is retained in the analysis to constraint the background events in signal region (details presents in chapter 7). In addition all the systematics errors on data computed in details and applied to the fit.

Neutrino cross section information in the MiniBooNE energy regime ($\approx 0.8\,GeV$) is important not only for next generation accelerator based neutrino experiments, but also for the search for dark matter produced in the Booster Neutrino Beamline in MiniBooNE detector. MiniBooNE was chosen to search for Dark Matter (DM) because it was already well understood after it had run for about a decade before doing the dedicated DM search. As neutrinos are the biggest background in the search for dark matter we need to have a careful measurement of neutrino cross section and understand the results with their uncertainties very well.

1.2 Layout of this document

Part one of this thesis starts with introduction of the SM of particle physics along with some details on the weak interaction, and the limitations on SM, also discusses some aspects of neutrino physics, and opens up the introduction of the MiniBooNE detector, and DM search at MiniBooNE. Chapter 3 focuses on the neutrino electron elastic scattering interactions and derives the theoretical neutrino electron elastic cross section formulae, moreover presents some previous measurements. Chapter 4 presents a description of the MiniBooNE experimental setup, in terms of either the hardware and software; This chapter also provides the details of the reconstruction algorithm and the particle identification. Chapter 5 provides information on the Monte Carlo simulation with an emphasis on

the models used to generate neutrino electron elastic scattering along with some of the most dominated background channels in the analysis.

Part two of this thesis presents the analysis and their results. Chapter 6 discusses the analysis of the process $\nu + e^- \rightarrow \nu + e^-$ with the selections applied on data to extract it. Chapter 7 presents the methods of measuring uncertainties. All sources of uncertainties on the data included, the measurement of the neutrino electron elastic scattering computes by fitting the Monte Carlo to the data, and the results are presented at the end.

2 Introduction

The Standard Model (SM) of particle physics was postulated in order to understand and explain all of the basic matter and the fundamental interaction among them. The model provides a precise description of the fundamental particles and how they interact. Although this model is a successful scientific theory and can explain what we know about the universe in most aspect, it seems to be inaccurate in a few components. For example, the SM fails to explain the origin of flavor mixing [10]. Therefore, extensions beyond the SM are needed to explain the missing parts, and investigations of these extensions are what make the field of experimental particle physics so interesting.

This chapter presents a brief overview of the SM with focusing on neutrinos and some limitation on the SM which are related to neutrino physics.

2.1 Standard Model Particles

A list of spin 1/2 particles in the SM is shown in Table 2.1. These particles, called fermions, arranged in doublets in increasing order of mass and forming three generations (I, II, and III). The most of the known universe is made of the particles from the first generation. The second and third generation particles are created at particle accelerators or cosmic rays and decay quickly into the particles of the first generation. The leptons, light particles, do not interact via the strong force while the quarks can interact with matter through any of the fundamental forces: strong, weak, or electromagnetic (EM). Moreover the neutral leptons, or neutrinos, are more restricted in interaction with matter, the neutrinos interact only via the weak force.

A different type of particle with spin 1, called Bosons, are force carrier (intermediate) particles. They are listed in Table 2.2 with their basic forces of interaction. The photon and the gluons (force carrier of the electromagnetic and strong interaction respectively) are massless, and the weak bosons (force carrier of weak interaction) are massive; $M_{W^{\pm}} \approx 80 GeV$ and $M_{Z^0} \approx 91 GeV$).

Classification	Particles			Forces
	I	II	III	
Quark	$\begin{pmatrix} u(up) \\ d(down) \end{pmatrix}$	$\begin{pmatrix} c(charm) \\ s(strange) \end{pmatrix}$	$\begin{pmatrix} t(top) \\ b(bottom) \end{pmatrix}$	$Strong, Weak, EM$
Lepton	$\begin{pmatrix} \nu_e \\ \text{e} \end{pmatrix}$	$\begin{pmatrix} \nu_\mu \\ \mu \end{pmatrix}$	$\begin{pmatrix} \nu_\tau \\ \tau \end{pmatrix}$	$Weak$ $Weak, EM$

Table 2.1: A partial list of Standard Model particles with their broad classifications (left column), names (center column, grouped by family), and forces by which they interact (right column).

Force	Participants	Mediator Particle(s)
EM	all fermions except ν	γ
Weak	all fermions	$W^{\pm}$, Z^0
Strong	only quarks	glouns

Table 2.2: Mediator particles of Standard Model with their basic force of interaction.

A list of all the quantum numbers of the quarks (leptons) are given in Table 2.3 (Table 2.4).

Quarks	Q	I_3	S	C	B	T	Mass
u	$+\frac{2}{3}$	$+\frac{1}{2}$	0	0	0	0	$2.3^{+0.7}_{-0.5} MeV$
d	$-\frac{1}{3}$	$-\frac{1}{2}$	0	0	0	0	$4.8^{+0.7}_{-0.3} MeV$
c	$-\frac{1}{3}$	0	-1	0	0	0	$1.275 \pm 0.025 GeV$
s	$+\frac{2}{3}$	0	0	+1	0	0	$95 \pm 5 MeV$
t	$-\frac{1}{3}$	0	0	0	-1	0	$173.5 \pm 0.6 \pm 0.8 GeV$
b	$+\frac{2}{3}$	0	0	0	0	+1	$4.18 \pm 0.03 GeV$

Table 2.3: List of quarks with their quantum numbers and mass. Q: electric charge, I_3: 3rd component of isospin, S: strangeness, C: charmness, B: bottomness, T: topness. These quantum numbers change their signs for anti-quarks. The values for the masses are from Ref. [8].

Leptons	Q	L_e	L_μ	L_τ	Mass
e	-1	+1	0	0	$0.511MeV$
ν_e	0	+1	0	0	$< 3eV$
μ	-1	0	+1	0	$106MeV$
ν_μ	0	0	+1	0	$< 0.19MeV$
τ	-1	0	0	+1	$1.78GeV$
ν_τ	0	0	0	+1	$< 18.2MeV$

Table 2.4: List of leptons with their quantum numbers and mass. Q: electric charge, L_e: electron number, L_μ: muon number, L_τ: tau number. These quantum numbers change their signs for anti-leptons. The values for the masses are from Ref. [8].

There is one more particle postulated in the SM, Higgs boson (H) with spin 0. The Higgs field (the Higgs's corresponding field which was proposed before the Higgs boson itself) is responsible for giving mass to all Dirac particles in the SM. When particles interact with the Higgs field, they feel the field by absorbing and emitting "virtual Higgs" (mediated Higgs). The real Higgs particle appears when the field's energy is flared up in a certain point.

After postulating of existing the Higgs boson, detecting it became the next goal. Since the theory did not predict the mass of the Higgs boson, the amount of energy needed to create it was a mystery. After years of planning the Large Hadron Collider (LHC), an massive experiment to potentially detect the theory of the Higgs boson, designed and started taking data. The existence of the Higgs has been reported recently by the ATLAS and CMS experiments at the LHC, they reported the mass in about $125\ GeV$ [11, 12].

Moreover, cosmological observations suggest that our universe contains dark matter (DM), although we have no measurements of its microscopic properties. DM first proposed by Fritz Zwicky in 1933 [13]. Zwicky calculated the mass to light ratio of the Coma cluster by combining the Hubble's and van Maaen's results, his study showed the total matter density needed to be about hundreds times the amount given by luminous matter to explain the Hubble's and van Maanen's results. In order to explain the result Zwicky suggested the existence of a dark particle. Three years later, in 1936, Sinclair Smith did a similar study for the Virgo cluster [14]. However it took more than 30 years for the physicists to accept DM as a real particle. Although the evidence of DM has been proved from a wide range of cosmological scales such as galaxies, clusters, cosmic microwave background (CMB), and gravitational lensing, its interaction with the SM particles is still a mystery.

2.2 Neutrino in Standard Model Particles

in 1930, after observing the missing energy in radioactive nuclear beta decay ($n \rightarrow p + e^- + \bar{\nu}_e$), Wolfgang Pauli suggested the existence of invisible parti-

cle coming along with the electron and carrying the missing energy. This particle has to interact with matter extremely weakly in order to explain why it had not been observed in experiments [15]. In 1954, Reines and Cowan designed the first experiment and successfully detected the Pauli particle during the inverse beta decay ($\bar{\nu} + p \rightarrow n + e^{+}$) [16]. The two other flavors of neutrino, which were postulated in the SM, have been observed directly in the following years. In 1963 , muon neutrino discovered from pion decay [17] at Brookhaven National Laboratory and in 2000, tau neutrinos discovered from decay of charmed mesons by the DONUT experiment at Fermilab [18].

After detecting the proposed neutrinos in the SM, the next step was to explain its interaction with particles. Neutrino interactions occur restrictedly through weak interaction via exchanging of two massive bosons: $W^{\pm}$ and Z^{0}, as shown in Table 2.2. Exchange of a Z^{0} is called a Neutral Current (NC) interaction, and exchange of a W^{+} or W^{-} is called a Charged Current (CC) interaction. When a $W^{\pm}$ is mediated the interaction, charge conservation requires that a charged lepton exit the interaction, while the NC interaction can occur for any fermions.

Another unusual nature of neutrinos, in addition to the restricted interaction, is its handedness. Handedness is related to helicity. Helicity is defined as the projection of a particle's spin (σ) along its direction of motion $\hat{p}$. The helicity gets positive (negative) value when spin aligned along (opposite) the direction of motion. Therefore the sign of the particle's helicity is frame dependent means that by boosting the particle to a frame which moving faster than speed of particle the sign of the momentum will change but the spin will not, this makes the helicity flips the sign.

In the case of massless particle like SM neutrinos, where boosting the frame is impossible, handedness is identical to helicity. A massless fermion is either entirely LH or RH. On the other hand, since the helicity is not an "intrinsic" property of massive particles, a property exists, called Chirality, which is equivalent to helicity in the massless limit and frame independent to the massive particle. The Chirality projection component matrices (RH (P_R) , and LH (P_L)) are related to $\gamma^5 = \gamma_5 = i\gamma^0\gamma^1\gamma^2\gamma^3$ matrix

$$P_R = \frac{1+\gamma^5}{2} \tag{2.1}$$

$$P_L = \frac{1-\gamma^5}{2} \tag{2.2}$$

It is alway possible to split a spinor field u into its chiral LH and RH component such that

$$u = u_R + u_L \quad \text{where} \quad u_R = P_R u \quad \text{and} \quad u_L = P_L u \tag{2.3}$$

By substituting the spinor field with the LH and RH components in the Dirac Lagrangian, the LH and RH components get independent kinetics terms but they couple by the mass term. This demonstrates that the space-time evolution of the chiral fields u_R and u_L are related by mass.

The details on Hamiltonian of weak interaction presents in section 3.1.

2.2.1 Limitation on Standard Model

There have been some experimental observations which show the SM predictions are incompleted - like the muon anomalous magnetic moment [8] and the phenomenon of neutrino oscillations and its consequence, i.e., massive neutrinos [19].

After discovery of neutrinos, physicists were looking for their physical properties like masses. The experiments have directly searched for neutrino masses have only been able to set upper/lower limits, the current bounds show in Table 2.4. Since the ν_e is consistent with the massless particle (Pauli particle) massless neutrinos added to the SM. However, after observing missing solar neutrino in some experiments the final hypothesis postulated neutrinos as massive particles. The mass of the particles make them able to transform from one type to another over the space-time in a phenomenon known as neutrino oscillations. Next section

provides some details on this phenomenon.

2.3 Neutrino Oscillation

The phenomenon of neutrino oscillation postulated to explain a mystery of the solar neutrino problem. In 1968 Davis et al. performed the first in a series of experiments to measure a deficit in the number of neutrinos observed coming from the sun as compared to the solar models [20]. Other experiments were designed in the following years with the same purpose, In 1988 Kamiokande experiment observed the same deficit in solar neutrino [21]; in 1998, after suggesting that neutrino are oscillated in flavor, Super-Kamiokande designed to become sensitive to other flavors of neutrinos [22]; and finally after the Sudbury Neutrino Observatory (SNO) experiment, the first detector sensitive to all three neutrino flavor, published the results in 2002 [23] Ray Davis received the noble prize on solar neutrino observation. In 2003, the reactor-based KamLAND experiment provided some explanation of the neutrino oscillation parameters. In addition, accelerator-based experiments (K2K [24] and MINOS [25]) have also confirmed the atmospheric neutrino oscillations.

Neutrino oscillation is a quantum mechanical phenomenon in which a neutrino of a specific lepton flavor oscillates in its flavor after traveling some distance. The oscillation in short (long) scale means neutrino has definite flavor (masses), but three or more possible masses (flavors). In principal, each flavor eigenstate (ν_e, ν_μ, and ν_τ) is a coherent superposition of the mass eigenstates (ν_1, ν_2, and ν_3), and their mixing is represented by the Maki-Nakagawa-Sakata (MNS) matrix - similar to the CKM matrix in the quark sector [8]

$$\nu_l = \sum_{m=l}^{3} U_{lm}\nu_m \quad \text{where} \quad l = e, \mu, \tau. \tag{2.4}$$

U is the unitary MNS matrix; it is a 3×3 matrix relating the three flavor eigenstates

with the three mass eigenstates:

$$U = \begin{pmatrix} U_{e1} & U_{e2} & U_{e3} \\ U_{\mu 1} & U_{\mu 2} & U_{\mu 3} \\ U_{\tau 1} & U_{\tau 2} & U_{\tau 3} \end{pmatrix}$$

$$= \begin{pmatrix} 1 & 0 & 0 \\ 0 & c_{23} & s_{23} \\ 0 & -s_{23} & c_{23} \end{pmatrix} \begin{pmatrix} c_{13} & 0 & s_{13}e^{-i\delta} \\ 0 & 1 & 0 \\ -s_{13}e^{-i\delta} & 0 & c_{13} \end{pmatrix} \begin{pmatrix} c_{12} & s_{12} & 0 \\ -s_{12} & c_{12} & 0 \\ 0 & 0 & 1 \end{pmatrix} \begin{pmatrix} e^{\frac{i\alpha_1}{2}} & 0 & 0 \\ 0 & e^{\frac{i\alpha_2}{2}} & 0 \\ 0 & 0 & 1 \end{pmatrix} \tag{2.5}$$

where the three mixing angles can be defined by , $c_{ij} = cos\theta_{ij}, s_{ij} = sin\theta_{ij}$, and δ is the CP phase. α_1 and α_2 are non-zero if neutrinos are not Dirac particles [26]. The probability of oscillation between two flavor states, in vacuum, is given by:

$$\begin{aligned} P_{\nu_a \to \nu_b} = \delta_{ab} - 4 \sum_{i>j} Re(U^*_{ai} U_{bi} U_{aj} U^*_{bj}) sin^2\big(\Delta m^2_{ij} \frac{L}{4E_\nu}\big) \\ +2 \sum_{i>j} Im(U^*_{ai} U_{bi} U_{aj} U^*_{bj}) sin^2\big(\Delta m^2_{ij} \frac{L}{4E_\nu}\big), \end{aligned} \tag{2.6}$$

where δ_{ab} is the Kronecker delta, U_{aj} is the lepton mixing matrix element with flavor index a and mass eigenstate index j, $\Delta m^2_{ij} = m^2_i - m^2_j$ is the mass squared difference between the mass eigenstates ν_i and ν_j, L is the distance between the source and the detection of the neutrino, and E_ν is the neutrino energy.

Considering the simple case of two generation mixing with the assumption of Dirac particle neutrinos makes investigating the probability easier. The mixing

matrix in this simplified case is:

$$\begin{pmatrix} \nu_e \\ \nu_\mu \end{pmatrix} = \begin{pmatrix} cos\theta & sin\theta \\ -sin\theta & cos\theta \end{pmatrix} \begin{pmatrix} \nu_1 \\ \nu_2 \end{pmatrix} \tag{2.7}$$

and the oscillation probability formula is reduced to

$$P_{\nu_a \to \nu_b} = \begin{cases} 1 - sin^2 2\theta sin^2\left(1.27\Delta m^2 \frac{L}{E}\right) & \text{if} \quad a = b \\ sin^2 2\theta sin^2\left(1.27\Delta m^2 \frac{L}{E}\right) & \text{if} \quad a \neq b \end{cases} \tag{2.8}$$

In the above equation we use in standard units for neutrino oscillation experiments

$$\frac{\Delta m^2_{12} L}{4E} \frac{c^3}{\hbar} = \Delta m^2_{12}(kg^2) \frac{L(m)}{4E(J)} \frac{c^3}{\hbar} = 1.27 \frac{\Delta m^2_{12}(eV^2) L(m)}{E(MeV)} \tag{2.9}$$

In addition to dependency on neutrino mixing angel (θ) and the mass differences (Δm^2), the probability to see oscillations also depends on two experimental parameters, L, the distance from the neutrino source to the detector, and E, the neutrino energy. In the experiment which designed very close to the neutrino source, the probability of observing the oscillations will be very low. In principle, the experiments are designed in terms of neutrino energy and the distance from the neutrino source in a way that can probe the interesting region of Δm^2 and $sin^2 2\theta$.

The current values of neutrino oscillation mixing parameters from the Particle Data Group in 2012 [8] present in Table 2.5.

2.4 The MiniBooNE Oscillation Search

The Mini Booster Neutrino Experiment (MiniBooNE) at Fermilab was designed to test the Liquid Scintillator Neutrino Detector (LSND) signal [27]. The details of the experiment will be discussed in Chapter 4, but a brief overview presents here along with the predicted oscillation sensitivity.

Parameter	best-fit ($\pm 1\sigma$)
Δm^2_{12}	$7.58\ ^{+0.22}_{-0.26} \times 10^{-5} eV^2$
$\lvert\Delta m^2_{32}\rvert$	$2.35\ ^{+0.12}_{-0.09} \times 10^{-3} eV^2$
$\sin^2\theta_{12}$	$0.306\ ^{+0.018}_{-0.015}$
$\sin^2\theta_{23}$	$0.43\ ^{+0.08}_{-0.03}$
$\sin^2\theta_{13}$	0.025 ± 0.0034

Table 2.5: Current values of neutrino oscillation mixing parameters.

MiniBooNE, like LSND, is an accelerator-based oscillation experiment. The neutrino beam is created by directing $8\ GeV$ protons from the Fermilab Booster onto a beryllium target installed inside the magnetic horn. Proton interacts with Beryllium target and produces a secondary beam of mesons. Mesons sign selected and go to decay region where decay to neutrino and produce the beam with mean energy of $\approx 750\ MeV$. The detector is located $541m$ from a neutrino source in the Booster Neutrino Beamline (BNB). This design results in an experimental $\frac{L}{E}$ of $\approx 0.72m/MeV$ which is similar to that of LSND ($\frac{L}{E} \approx 0.75m/MeV$). The two experiments are sensitive to the same ranges in oscillation parameter space.

2.5 Dark Matter Beyond The Standard Model of Particles

As mentioned earlier, dark matter was not predicted in the SM of particles, and the properties of its interaction is not well understood. But observations show that our universe contains dark matter. Using neutrino detectors to search for low-mass DM is logical due to the similarity of the DM and neutrino signatures in the detector.

The MiniBooNE experiment has produced the first proton beam-dump light DM search results by steering the boosted proton beam to off-target and reduced the neutrino flux. Moreover running in off-target mode made the neutrino energy

spectrum softer compared to neutrino mode running (details on the neutrino mode flux presents in section 5.1). Using DM scattering from nucleons, MiniBooNE did not observed any significant excess over the background. 90% confidence limits were set over a large parameter space in the vector portal light dark matter model [28], testing the vector portal model with MiniBooNE off-target data showed that MiniBooNE for the DM mass (m_χ) between $100\ MeV$ to $400\ MeV$ excludes new parameter space in comparison with previous direct detection results.

Also, in order to test of other theories, a model independent DM rate was extracted (by performing the general excess search). Moreover, MiniBooNE tested the Leptophobic light DM model. The model is defined by adding a baryonic current to the vector portal model Lagrangian, which suppressed the lepton interactions, and setting the kinetic mixing angle between the dark sector and SM particles to zero.

It should be noted that experiments on proton fixed target have high sensitivity to the Leptophobic light dark matter model by searching for neutral current elastic (NC-Els) and inelastic Δ signatures in their detectors. In the Leptophobic light dark matter model MiniBooNE excluded a large range of new parameter space. The details of this study on MiniBooNE DM, and the off-target flux can be found in Ref. [29].

3 Electron Neutrino Elastic Scattering

After Wolfgang Pauli proposed the existence of the neutrino in 1930 [15], Enrico Fermi was the first physicist to work out the theory of the interaction by analogy with the electromagnetic interactions. His interaction Lagrangian with no propagator equivalent to,

$$L_{weak} = \frac{G_F}{\sqrt{2}}\big(\overline{p}\gamma^{\mu}n\big)\big(\overline{e}\gamma_{\mu}\ \nu\big) \tag{3.1}$$

where γ^{μ} are the Dirac gamma matrices and G_F is the Fermi constant.

Fermi predicted a value for G_F for the first time, which is now known to be $1.166 \times 10^{-5} GeV^{-2}$. His theory works fine in low energy region but breaks down in high energy, so, the modification was necessary in his simplified theory.

In 1956 T.D. Lee and C. N. Yang [30] after investigating of the decay paths of strange mesons τ and θ, which seemed to be identical particles, observed that they decayed differently (τ to an parity odd state(π^+, π^+, and π^-) and θ to a parity even state (π^+, π^0, and π^0)). So, they suggested that parity may be violated in the weak interaction. One year later C.S. Wu et al. [31] experimentally proved that left-handed and right handed electron behave differently in the nuclear beta-decay of ^{60}Co, and concluded that parity is violated in weak interaction.

In 1958 Sudarshan and Marsak modified the Fermi theory in order to insert the observed parity violation ($V - A$ model (vector minus axial vector)) [32]. In the same year, Feynmann and Gell-Mann [33] independently arrived at the same conclusion. The proposed interaction Lagrangian with their modification written as following:

$$L_{weak} = \frac{G_F}{\sqrt{2}}\big(\overline{p}\gamma^{\mu}(1-\gamma_5)n\big)\big(\overline{e}\gamma_{\mu}\ (1-\gamma_5)\nu\big) \tag{3.2}$$

where $\gamma_5 \equiv i\gamma_0\gamma_1\gamma_2\gamma_3$.

In this chapter, the general weak interaction Hamiltonian is presented, then it

is used to calculate the electron neutrino elastic scattering cross section. The kinematics of the interaction is shown to get the interaction's essential characteristics.

3.1 Weak Interactions Hamiltonian

The modern view of the weak interaction is mediated by the exchange of massive W and Z bosons. In most experiments, even in high-energy region, the energy of the process is much smaller than the masses of weak mediator particles (W and Z which are of the order of 100 GeV [34]). In this low energy process, the gauge boson propagators in momentum, is far off shell, can be approximated to the point like in Feynman diagram, which results in an effective four-fermion interaction. The general Hamiltonian governing the process $\nu f \rightarrow l/\nu + f'$ can be written as

$$H_{weak} = \frac{4G_F}{\sqrt{2}} \big[\overline{l}/\overline{\nu}\gamma_\mu \frac{1-\gamma_5}{2}\nu\big] \big[\overline{f'}\gamma^\mu \big(g_L \frac{1-\gamma_5}{2} + g_R \frac{1+\gamma_5}{2}\big) f\big] + h.c \quad (3.3)$$

where f, f', l and ν stand for an initial and final state fermion, lepton and neutrino respectively, g_L and g_R are the weak Neutral Current chiral couplings, γ_μ are the standard Dirac matrices and $\gamma_5 \equiv i\gamma_0\gamma_1\gamma_2\gamma_3$. This modern Hamiltonian does include parity violation which one can not find in Fermi's theory. The factor $\frac{1-\gamma_5}{2}$ is a projection operator for left-handed states of fermions and right-handed states of anti-fermions. This furnished Hamiltonian, also, indicates neutrino participating in weak interaction is entirely left-handed.

The above Hamiltonian of weak interaction can be used to compute the cross section of both NC and CC interaction. Noting that the parity is maximally violated in CC interaction, however in the case of NC interaction the couplings are in terms of the electromagnetic and weak couplings, from the electroweak unification theory, with the value of the weak Neutral Current chiral couplings for each fermion coupling specified in Table 3.1. Note the right-handed neutrino has no weak couplings, neither in the neutral nor the charged current, which makes it unique among the fermions.

Z coupling	g_L	g_R	g_V	g_A
ν	$1/2$	0	$1/2$	$1/2$
e,μ,τ	$-1/2+\sin^2\theta_W$	$\sin^2\theta_W$	$-1/2+2\sin^2\theta_W$	$-1/2$
u,c,t	$1/2-(2/3)sin^2\theta_W$	$-(2/3)sin^2\theta_W$	$1/2-(4/3)sin^2\theta_W$	$1/2$
d,s,b	$-1/2+(1/3)sin^2\theta_W$	$(1/3)sin^2\theta_W$	$-1/2+(2/3)sin^2\theta_W$	$-1/2$

Table 3.1: Value of g_L, g_R, g_V, and g_A for fermions where θ_W is the weak mixing angle or Weinberg angle [9].

3.2 Electron Elastic Scattering Cross Section

With explanation of the weak interaction in previous section, we are ready to calculate a electron neutrino scattering cross section. In this section, the physical cross section of the interaction are calculated using on the Feynman diagram associated to it.

3.2.1 Feynman diagram

The simplest and cleanest neutrino interaction that can be considered is electron elastic scattering, where an incoming neutrino interacts with a free fundamental particle, electron, causing the electron to recoil but leaving no other experimental signatures. The Feynman diagrams for electron elastic scattering is shown in Figure 3.1.

The amplitude for NC interaction gives by the equation below,

$$M_{NC} = -i\frac{g^2}{4cos\theta_W M_Z^2}\left[\overline{u_3}(g_V^\nu\gamma^\mu - g_A^\nu\gamma^\mu\gamma^5)u_1\right]\left[\overline{u_4}(g_V^e - g_A^e\gamma_\mu\gamma^5)u_2\right] \quad (3.4)$$

On the other hand, for CC elastic interaction that can occur for ν_e, by considering the different mediator and coupling gives by the amplitude below,

$$M_{CC} = -i\frac{g^2}{8M_W}\left[\overline{u_3}(\gamma^\mu - \gamma^\mu\gamma^5)u_1\right]\left[\overline{u_4}(\gamma_\mu - \gamma_\mu\gamma^5)u_2\right] \quad (3.5)$$

in which

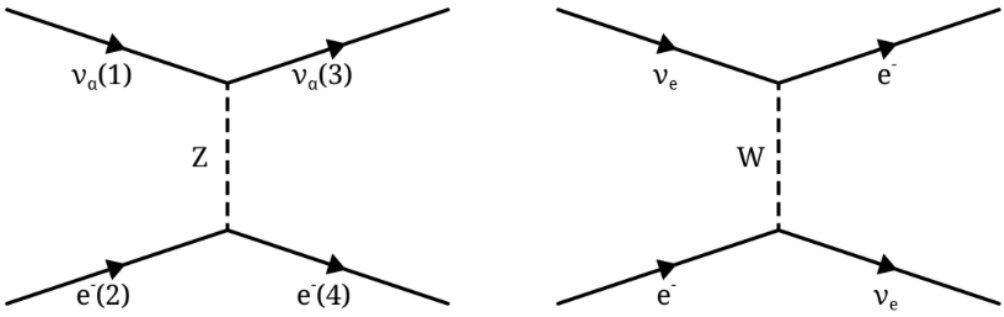

Figure 3.1: Feynman diagrams for electron elastic scattering. (left) All three neutrino flavors ($\alpha = e, \mu, \tau$) can undergo NC scattering off an electron. (right) For ν_e there is an additional CC mode.

- u is Dirac spinors (it has both left-handed, and right-handed handedness components $u = u_R + u_L$. The separated Dirac spinor is given in Table 3.2;
- g is coupling-strength;
- M_Z (M_W) mass of Z (W) boson;
- g_A, and g_V are axial-vector and vector vertex factors (Table 3.1). Their relation to the handedness coupling are given by $g_V = g_L + g_R$, $g_A = g_L - g_R$;

Particle	Anti-Particle
$u_L = \frac{1}{2}(1-\gamma^5)u$	$\nu_L = \frac{1}{2}(1+\gamma^5)\nu$
$u_R = \frac{1}{2}(1+\gamma^5)u$	$\nu_R = \frac{1}{2}(1-\gamma^5)\nu$
$\overline{u}_L = \frac{1}{2}\overline{u}(1+\gamma^5)$	$\overline{\nu}_L = \frac{1}{2}\overline{\nu}(1-\gamma^5)$
$\overline{u}_R = \frac{1}{2}\overline{u}(1-\gamma^5)$	$\overline{\nu}_R = \frac{1}{2}\overline{\nu}(1+\gamma^5)$

Table 3.2: Dirac spinors separated out using the chiral projection operators γ^5

The averaged amplitude of NC(CC) interaction equation(3.4)(equation(3.5)) over incoming spin states, and the summation of it over outgoing spin sates($\langle|M|^2\rangle$) gives the cross section of the process.

Form the point like Feynman diagram approximation of the low-energy process (by considering the effective four-particles with single vertex) we can obtain the relation between Fermi constant and the coupling constant of NC and CC in-

teractions

$$\text{CC:} \quad \frac{G_F}{\sqrt{2}} = \frac{g^2}{8M_W^2} \tag{3.6}$$

$$\text{NC:} \quad \frac{G_F}{\sqrt{2}} = \frac{g^2}{8M_Z^2 cos\theta_W^2} \tag{3.7}$$

These notations allow us to write the low-energy Lagrangian of the electron neutrino elastic scattering events (Figure 3.1) in the compact form

$$L_{(\nu_\alpha e^- \to \nu_\alpha e^-)} = -\frac{G_F}{\sqrt{2}}[\bar{\nu}_\alpha \gamma^\rho (1-\gamma^5)\nu_\alpha][\bar{e}\gamma_\rho (g_V^l - g_A^l \gamma^5)e] \quad \text{where}(\alpha = e, \mu, \tau) \tag{3.8}$$

$$L_{(\nu_e e^- \to \nu_e e^-)} = -\frac{G_F}{\sqrt{2}}[\bar{\nu}_e \gamma^\rho (1-\gamma^5)\nu_e][\bar{e}((1+g_V^l) - (1+g_A^l)\gamma^5)e] \tag{3.9}$$

After tedious calculation, the differential cross section of the process $\nu_i + e_i \to \nu_f + e_f$ is equivalent to,

$$\frac{d\sigma}{dQ^2} = \frac{G_F^2}{\pi}\big[g_1^2 + g_2^2(1 - \frac{Q^2}{2p_{\nu i}.p_{ei}})^2 - g_1 g_2 m_e^2 \frac{Q^2}{2(p_{\nu i}.p_{ei})^2}\big] \tag{3.10}$$

where Q^2 is negative four-momentum transfer ($Q^2 = -q^2$ where $q = p_{\nu i} - p_{\nu f}$), $p_{\nu i}$, p_{ei}, $p_{\nu f}$ and p_{ef} are initial and final momentum of neutrino and electron, and quantities of g_1 and g_2 depend on weak mixing angle as shown in Table 3.3.

	ν_e	$\bar{\nu}_e$	$\nu_{\mu,\tau}$	$\bar{\nu}_{\mu,\tau}$
g_1	$\frac{1}{2} + sin^2\theta_W$	$sin^2\theta_W$	$-\frac{1}{2} + sin^2\theta_W$	$sin^2\theta_W$
g_2	$sin^2\theta_W$	$\frac{1}{2} + sin^2\theta_W$	$sin^2\theta_W$	$-\frac{1}{2} + sin^2\theta_W$

Table 3.3: Value of g_1, g_2 for different neutrino flavor in the general differential cross section equation (3.10).

In the laboratory frame where $\overrightarrow{p_{ei}} = 0$, we can have $Q^2 = 2m_e T_e$, where T_e is the kinetic energy of the recoil electron. The differential cross section as a function of the energy of recoil electron can be written as

$$\frac{d\sigma}{dT_e}(E_\nu, T_e) = \frac{2G_f^2 m_e}{\pi}\big[g_1^2 + g_2^2(1 - \frac{T_e}{E_\nu} - g_1 g_2 \frac{m_e T_e}{E_\nu^2})\big]. \tag{3.11}$$

From the energy-momentum conservation in laboratory frame we can have the energy of the recoil electron in terms of electron scattering angle (shows in Figure 3.2)

$$T_e = \frac{2m_e E_\nu^2 cos^2\theta}{(m_e + E_\nu)^2 - E_\nu^2 cos^2\theta} \tag{3.12}$$

therefore the differential cross section as a function of electron scattering angle is

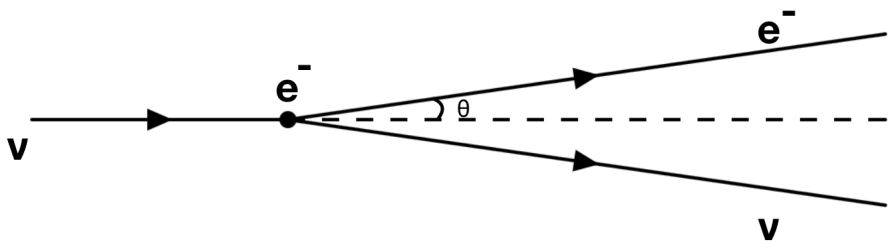

Figure 3.2: Geometry of the neutrino scattered off electron.

given by

$$\frac{d\sigma}{dcos\theta}(E_\nu, cos\theta) = \frac{2G_F^2 m_e^2}{\pi}\frac{4E_\nu^2(m_e + E_\nu)^2 cos\theta}{[(m_e + E_\nu)^2 - E_\nu^2 cos^2\theta]^2}\big[g_1^2 + g_2^2(1 - \frac{2m_e E_\nu cos^2\theta}{(m_e + E_\nu)^2 - E_\nu^2 cos^2\theta^2})^2 - g_1 g_2 \frac{2m_e^2 cos^2\theta}{(m_e + E_\nu)^2 - E_\nu^2 cos^2\theta}\big] \tag{3.13}$$

3.2.2 Total Cross Section

The results of total electron neutrino/antineutrino elastic scattering for different neutrino/antineutrino flavor at the tree level Feynmann diagram with the assumption of negligible neutrino masses ($m_\nu \approx 0$) and sufficiently high energy interaction, where the electron mass is small compare to the total energy of the process ($s = (E_{\nu i} + E_{ei})^2|_{\overrightarrow{p_{ei}}=0} = 2m_e E_\nu$; where $E_\nu \gg m_e$), are shown in Table 3.4. Adding the loop Feynmann diagram integrates to an approximately 1% effect on the total cross section.

Process	Total cross section ($\times 10^{-45} cm^2$)
$\nu_e + e^-$	$(G_F^2 m_e E_\nu/2\pi)\left[(1+2sin^2\theta_W)^2 + \frac{4}{3}sin^4\theta_W\right] \approx 9.5E_\nu/MeV$
$\bar{\nu}_e + e^-$	$(G_F^2 m_e E_\nu/2\pi)\left[\frac{1}{3}(1+2sin^2\theta_W)^2 + 4sin^4\theta_W\right] \approx 4.0E_\nu/MeV$
$\nu_{\mu,\tau} + e^-$	$(G_F^2 m_e E_\nu/2\pi)\left[(1-2sin^2\theta_W)^2 + \frac{4}{3}sin^4\theta_W\right] \approx 1.5E_\nu/MeV$
$\bar{\nu}_{\mu,\tau} + e^-$	$(G_F^2 m_e E_\nu/2\pi)\left[\frac{1}{3}(1-2sin^2\theta_W)^2 + 4sin^4\theta_W\right] \approx 1.3E_\nu/MeV$

Table 3.4: Total electron neutrino/antineutrino elastic scattering cross section where $E_\nu \gg m_e$ for different neutrino/antineutrino flavor

The electron neutrino elastic scattering in the MiniBooNE is simulated at the tree level with standard model assumption. The purpose of this thesis is to find the total cross section of ν_μ scattering off the electron in the experiment.

3.3 Kinematic of The Electron Neutrino Elastic Scattering

As mentioned earlier in previous section, the energy of electron recoil in laboratory gives by the equation 3.12, from this equation the electron scattering angle then can be written as

$$cos\theta = \sqrt{\frac{T_e}{Te + 2m_e}}\frac{m_e + E_\nu}{E_\nu} \tag{3.14}$$

When $E_\nu \gg m_e$, which is a realistic assumption with boosted neutrino, $cos\theta \approx 1$, means that the final state electron of the elastic scattering $\nu_\alpha + e^- \rightarrow \nu_\alpha + e^-$ is emitted in very forward direction with respect to the incident neutrino beam. This criteria is crucial to the selection of this channel (chapter 6).

3.4 Experimental methods

As already pointed out, electron neutrino elastic scattering demonstrates experimentally as a single forward scattered electron. This signature and the small cross section ask for the experiment and devices with specific characteristics. First, an intense neutrino beam and a large target mass are required to overcome small event rates. Second, good electron identification and reconstruction are extremely vital. Especially an angular resolution in the same order of magnitude as the small scattering angles requires to make it possible to detect the very forward recoil electron. Third, the detector should have a good discrimination power to distinguish irreducible background events (single photon).

3.5 Previous Measurement

Muon neutrino electron scattering

The study of muon neutrino electron scattering was only possible when intensive muon neutrino beams could be provided. At high energy accelerators the source of neutrinos are weak decays of kaons and pions produced by protons in an external target. The mesons are focussed and charge selected by magnetic lenses (horns) before entering a decay region where part of them decay mainly into muons and muon-neutrinos. The surviving hadrons and muons are stopped in massive shielding. Changing the polarity of the magnetic lenses leads to either neutrino or antineutrino beams. However muon neutrino beams are not pure (details are presented in section 5.1).

Electron neutrino electron scattering

Compared to the muon neutrino sector the number of experimental results in electron neutrino electron scattering is still rather poor. This has two reasons, first

pure electron neutrino beams are more difficult to produce than muon neutrino beams and second ν_{e^-} and $\bar{\nu}_{e^-}$ beams are much lower in energy, so that large event rates are difficult to achieve.

Table 3.5 summarized the results from some neutrino electron scattering experiments.

Experiment	$\sigma(\nu_\mu e)/E_\nu(\times 10^{-45} cm^2 MeV^{-1})$
Gargamelle (PS) [35]	< 1.4
Aachen-Padova (PS) [36]	1.1 ± 0.6
Gargamelle (SPS) [35]	$2.4^{+1.2}_{-0.9}$
VMWOF (FNAL) [37]	$1.4 \pm 0.3 \pm 0.4$
BNL-COL (AGS) [38]	1.67 ± 0.44
CHARM (SPS) [39]	$2.2 \pm 0.4 \pm 0.4$
BNL E734 (AGS) [40]	$1.8 \pm 0.2 \pm 0.25$
CHARM-2 [41]	$1.53 \pm 0.04 \pm 0.12$
	$\sigma(\nu_e e)/E_\nu(\times 10^{-45} cm^2 MeV^{-1})$
LAMPF E225 (LAMPF) [42]	$10.0 \pm 1.5 \pm 0.9$

Table 3.5: Total cross section for all electron neutrino scattering experiments

4 The MiniBooNE Experiment

As mentioned earlier in Section 2.4, the Mini Booster Neutrino Experiment (MiniBooNE) located at Fermi National Accelerator Laboratory in Batavia, Illinois, was designed with the same distance over energy as LSND ($(\frac{L}{E_\nu})_{MiniBooNE} \approx (\frac{L}{E_\nu})_{LSND}$) in order to test the LSND experiment with the same sensitivity to oscillation parameter space (Δm^2 vs. $sin^2(2\theta)$). On the other hand, MiniBooNE is operated in higher neutrino energy (E_ν) (to increase the cross section of the interaction) and longer baseline with different oscillation signature and different systematic uncertainties as they were for LSND.

MiniBooNE collected more than 1 million neutrino interactions on pure mineral oil (CH_2) with the primary purpose of answering LSND signal. Moreover the high statistics data enabled the experiment to study on non-oscillation physics such as the cross section measurement which this thesis presents.

This chapter starts with describing the detailed setup for generating the neutrino/antineutrino flux. Next it gives a description of the detector. Finally it presents the prediction for both the neutrino flux and the detector response.

4.1 The MiniBooNE Experiment

Figure 4.1 shows a schematic representation of the experiment. The $8\,GeV$ kinetic energy protons, from Fermilab's proton synchrotron (Booster), hit the Beryllium target which is installed in a device called a horn. Horn uses a toroidal magnetic field to focus the charged mesons created in the proton-Beryllium interactions.The magnetic field inside the horn selects the positive (negative) sign of the mesons in neutrino (anti-neutrino) mode. The sign-selected mesons directed to a 50 meter decay region where most of the mesons decay to create the tertiary beam of neutrinos. Any mesons that do not decay in this region are stopped by an absorber at the end of the decay region. The tertiary beam, mostly muons and neutrinos, travel through ≈ 500 meters of earth to reach the detector (the details of each of stages presents in following section). Since the earth stops all charged particles, the beam is purely neutrinos by the time it reaches the detector. The detector

consists of a $610cm$ radius spherical tank made of carbon steel. It is located in a cylindrical concrete structure that is below ground; the top of the detector is at grade level, but it is covered by 3 meters of earth to reduce cosmic rays entering the detector.

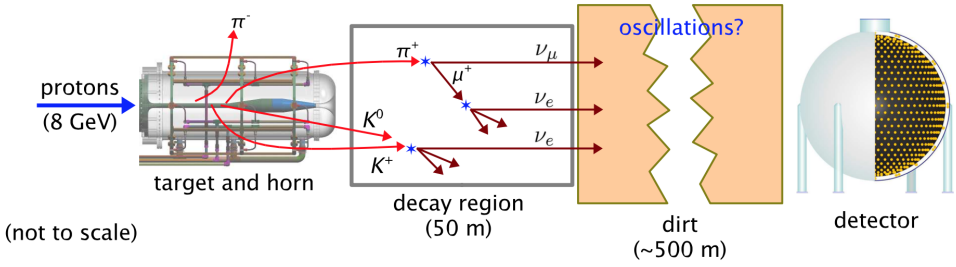

Figure 4.1: A schematic representation of the MiniBooNE beam-line and detector.

The detector is facilitated with photomultiplier tubes (PMT) and filled with 800 tons of mineral oil. It is separated into two optically isolated regions: the inner "tank" (signal) region and the outer "veto" region.

The neutrinos may interact with nucleons/electrons in the detector medium and produce both Cerenkov radiation and scintillation light as the charged particles from the interactions travel through the material inside the tank. The light is detected by the PMT, and the pattern of light in the tank region is used to tag the type of the particles. The veto region detects charged particles entering or exiting the tank region; it is primarily used to reject cosmic muons. Additionally, the veto region facilitates the identification of the events that create from interactions outside the detector (in the dirt) but find the way to enter inside the detector.

4.2 The MiniBooNE Neutrino Beam

4.2.1 Primary Proton beam

The primary protons generate from hydrogen gas which is ionized into H_2^- ions and accelerated by the $750\ keV$ electrostatic gap at the Cockroff-Walton generator. The accelerated H_2^- ions are directed to the linear accelerator (LINAC) and leave

it with $400\ MeV$ kinetic energy. The H^- ions pass through a stripping foil which converts them into H^+ ions (protons) then enter into the next accelerator, the Booster. Note that the negative hydrogen ion has chosen as the particle to create proton beam in accelerator facilities because the charge exchange interaction to convert H_2^- to proton can double the accelerating voltage and create high current proton beams. Moreover the ion's charge polarity can be inverted by removing two electrons as it passes through a thin stripping foil and generating a bare proton. The proton beam kinetic energy is boosted to $8.89\ GeV$ in Fermilab Booster, a $468m$ circumference synchrotron, and sent to the Main Injector. Beam is extracted from a single turn, done by a kicker magnet, in the Booster ring. Figure 4.2 shows the Booster neutrino beam-line (BNB).

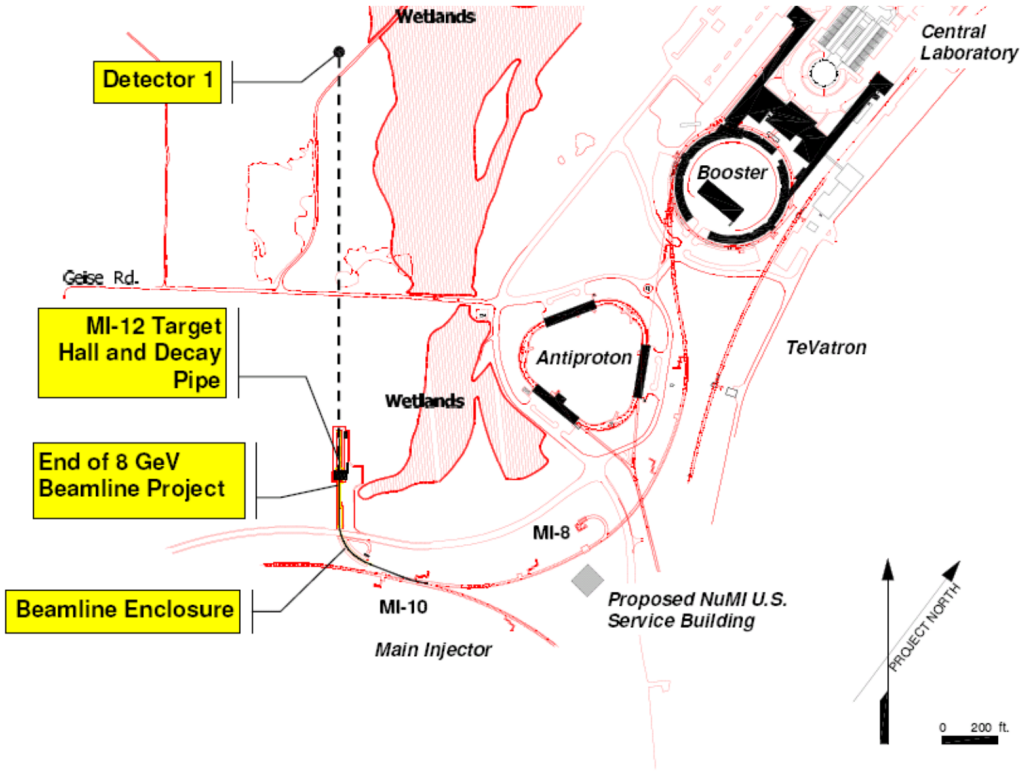

Figure 4.2: The Booster neutrino beam-line. Figure appears in Ref [1].

The spill, each extracted collection of protons, has the average of 4×10^{12} protons with an uniform structure. Figure 4.3 shows the schematics of the structure of the beam. in the microstructure the protons are divided into 81 bunches with approximately $6ns$ wide and $19ns$ apart, the macrostructure of the beam is the combination of 81 bunches which creates approximately $1.6\mu s$ wide proton beam within a $19.2\mu s$ window.

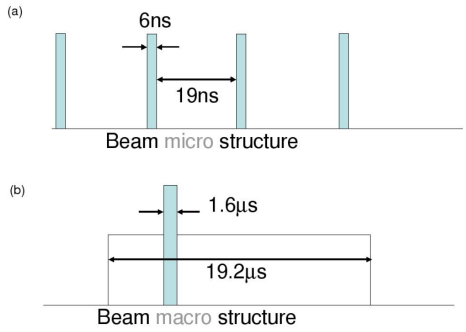

Figure 4.3: The microstructure (a) and macrostructure (b) of the proton beam.

The spill of boosted proton beam leads to the MiniBooNE target hall, a device in which a series of dipole and focusing-defocusing magnets use to focus the meson beam produced by the proton-Beryllium interaction. The beam position and width is known to within $0.1mm$ due to the beam position monitor (BPM) and a multi-wire chamber. The beam current is measured by two toroids upstream of the target. Together they can measure the number of protons on target (POT) to within 2 to 3%.

4.2.2 Secondary meson beam

The Boosted protons strike a $71cm$ Beryllium target, some of the properties of Beryllium are listed in Table 4.1, located inside the magnetic focusing horn, but physically separate from the horn assembly to allow extracting it without removing the horn. Proton interactions in the target produce short-lived hadrons (mostly pions (π^+ and π^-) and kaons (K^+, K^-, and K^0) as well as protons and neutrons). The MiniBooNE horn is designed by Bartoszek Engineering [2]. The

precise design carefully satisfys the requirements, such as the correct focusing characteristics, tolerate stresses due to target heating and cooling, and radiation damage. The horn's total length is 73-inch ($185.4cm$). The radius of the inner conductor varies from 0.87-inch ($2.2cm$) to 2.58-inch ($6.54cm$); the inner radius of the outer conductor is 11.81-inch ($30cm$). Current flows along the inner conductor and back along the outer conductor (the polarity can be reversed to select neutrino/anti-neutrino mode) to produce a toroidal magnetic field that is contained in the volume between the two coaxial horn conductors. The optimization of the shape of the inner conductor and the magnitude of the current has been done by GEANT simulation [43]. These physical properties of the horn has been chosen to maximize the ν_μ flux between 0.5 and $1\ GeV$ at the detector and simultaneously minimize flux above $1\ GeV$.

The target is air cooled by circulating air via the tubes which open into the target assembly. The horn is cooled with water (from radioactive water (RAW) system) that is sprayed onto the inner conductor through vibration-isolated nozzles attached to the outer conductor. The whole target assembly and cooling system shows in Figure 4.4.

Properties of Beryllium	
Density	$1.85gr/cm^3$
Interaction length	$40.7cm$
Specific energy loss (MIP)	$1.59MeV/cm$
Specific heat	$3.3J/(cm^3K)$
Young's modulus	$3.1 \times 10^{11}GPa$

Table 4.1: Properties of Beryllium.

4.2.3 Tertiary neutrino beam

The focused positively (negatively) charged mesons in MiniBooNe neutrino (anti-neutrino) mode travel into a $50m$ long decay pipe of 36-inch radius, is filled with air and closed at both ends, where the mesons decay in flight (DIF) to neutrinos. At the end of the decay pipe there is a steel and concrete absorber to stop all parti-

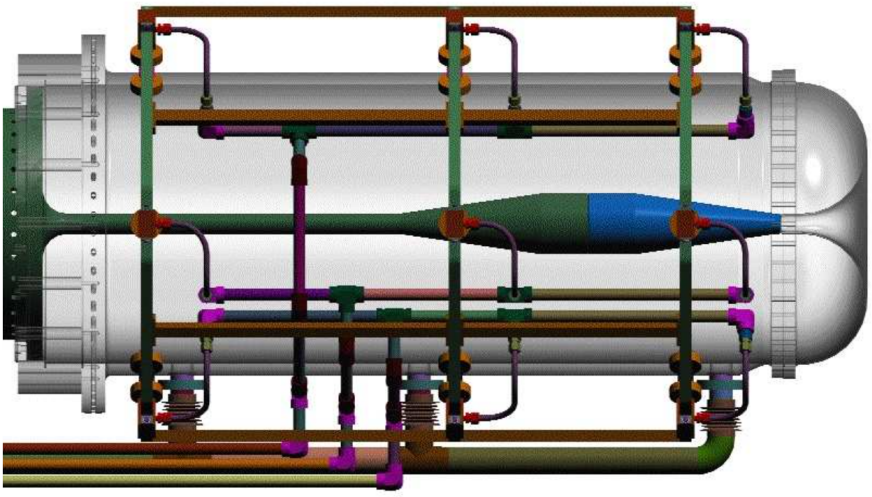

Figure 4.4: The MiniBooNE magnetic focussing horn. Also seen are the plumbing for water cooling. Figure from Ref. [2]

cles except neutrinos. The neutrinos travel through into $540m$ of dirt in which the neutrino oscillation can happen; the neutrino beam then goes into the MiniBooNE detector.

It is important to note that higher energy neutrinos have a larger interaction cross section which provide a larger number of neutrino events, but also a larger number of background events. Therefore in the design of an experiment the optimization must be made between large numbers of interactions and low average energy (in order to reduce the background events). The most dominated background events in the oscillation analysis are intrinsic ν_e in the beam (from decay of pions and kaons) and π^0 misidentification in the detector.

4.3 The MiniBooNE Detector

The MiniBooNE is a spherical Cherenkov detector with $610cm$ radius. The inner/tank (outer/veto) region is lined with 1280 (240) PMTs pointed inwards (pointed along the circumference). The tank region is painted black to minimize reflec-

tions. Reflection of light can produce Cerenkov light to appear isotropic and delayed, like scintillation light. On the contrary the veto region is painted white in order to maximize light collection at the PMTs. The entire tank is filled with 807 tons of pure mineral oil; the usable volume for physics analyses is approximately 445 tons.

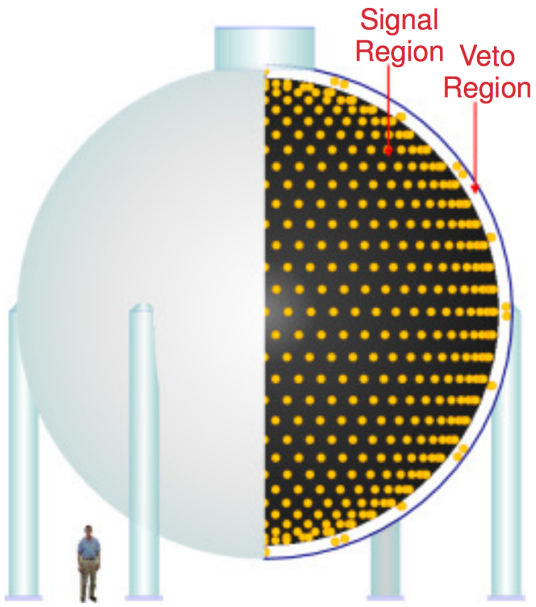

Figure 4.5: A schematic of the MiniBooNE detector. From Ref. [3].

Figure 4.6 shows a snapshot of the tank and veto regions of the detector, which also illustrates the PMT orientations in the two volumes.

The tank access and electronics area which is assembled directly above the detector vault and provides an open space for access, shown in Figure 4.7. The detector building also contains the preamplifier electronics for the PMTs along with the data acquisition electronics. A cage structure, that surrounds the top access opening, provides a shielded area for the PMT signal cables.

As it mentioned earlier, the MiniBooNE detector building is covered by an earth soil and rock in order to keep the cosmic ray muon rate under $10\ kHz$. Due to the pulsed neutrino and known arrival time of the beam the earth shielding from

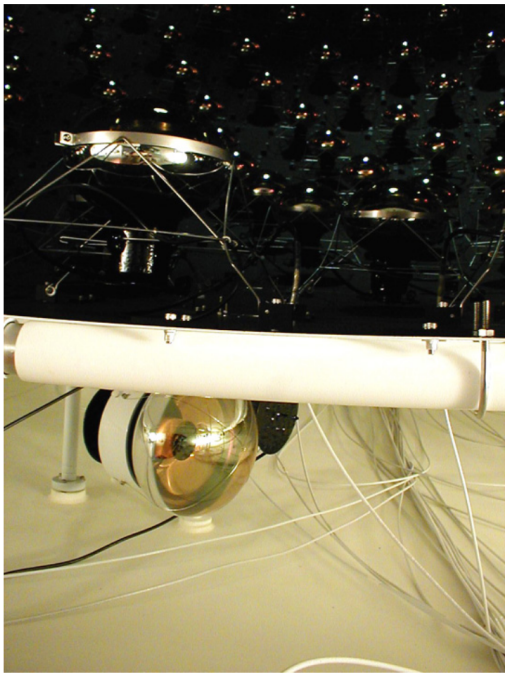

Figure 4.6: A snapshot of the tank and veto regions. Note the orientations of the PMTs in the two regions and the colors of the two regions.

cosmic rays is only one in MiniBooNE detector.

4.3.1 Mineral Oil

$\approx 95\%$ of the detector volume is oil, the rest 5% contains the volume of PMTs, their cables, and detector steel. By applying the fiducial volume selection the interactions with these other possible nuclear targets and the dirt becomes so small and can be negligible. The detector is filled with 807 tons of Light Mineral Oil (Industrial NF grade) with following properties:

- Density: A more dense oil provides more interactions in the detector.
- Viscosity: The oil must be recirculated which imposed an upper limit on the viscosity of the oil (and an implicit maximum density).
- Color: it was important that the oil be clear to the light detected by the PMTs

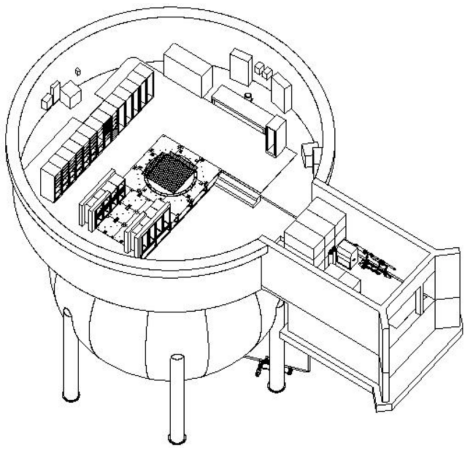

Figure 4.7: MiniBooNE detector plant [4]. Covering structures and earth overburden are not shown.

(wavelengths from $320nm$ to $600nm$) [44], implying a minimum attenuation length.

Based on these specifications and the results of testing performed, Marcol 7, an Exxon/Mobil product manufactured by Penreco, was chosen for the MiniBooNE detector. The results of measurements of the relevant oil properties are shown in Table 4.2. Details of all studies performed on the MiniBooNE mineral oil can be found in Ref. [45].

Density	$0.845 \pm 0.001 g/cm^3$
Refractive index(at = 589.3nm, temp=20.0^0C)[]	1.4684 ± 0.0002
Attenuation length (at 400 nm)	$14 \pm 2m$

Table 4.2: Results of some of the tested properties of MiniBooNE oil, Marcol 7.

Nitrogen gas is continuously bubbled through the oil so as to clean it of oxygen. Mineral oil needs no continuous purification; it cleaned for the first time and any remaining impurities will either float to the surface or sink to the bottom of the detector. In order to deal with any thermal expansion of the oil MiniBooNE is facilitated with an overflow tank.

4.3.2 The Photomultiplier Tubes

The inner region's PMTs collect light from neutrino interactions occurring in the tank detector region. The outer veto region's PMTs are located to capture the charged particles entering from outside the detector (cosmic rays, and the particles from the interactions outside the detector in dirt which pass through inside). Of the 1520 PMTs in the MiniBooNE detector in total, 1197 are inherited from LSND and the other 323 were purchased from Hamamatsu [46]. The LSND PMTs are 8-inch diameter, 9-stage, Hamamatsu model $R1408$ PMTs; the new PMTs are 8-inch, 10-stage, Hamamatsu model $R5912$ PMTs (an upgraded version of the $R1408$). The technical specifications for both of these types of photomultiplier tubes may be found in Ref. [47].

The charge, timing response and proper operating voltage of each PMT was tested before installation [47]. All LSND PMTs ($R5912$) and those $R1408$ PMTs whose test results showed the best performance are lined in the main tank region, and the remaining PMTs of $R1408$ installed in the veto region. A wire frame attached each PMT in its location in the tank region and make the phototube support structure (PSS). A schematic diagram of a PMT in its wire frame is shown in Figure 4.8.

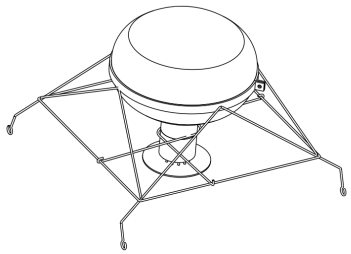

Figure 4.8: The wire support frame used to attach PMTs in the main tank region of the detector [4].

The PMTs are arranged in the detector in the pattern shows in Figure 4.9.

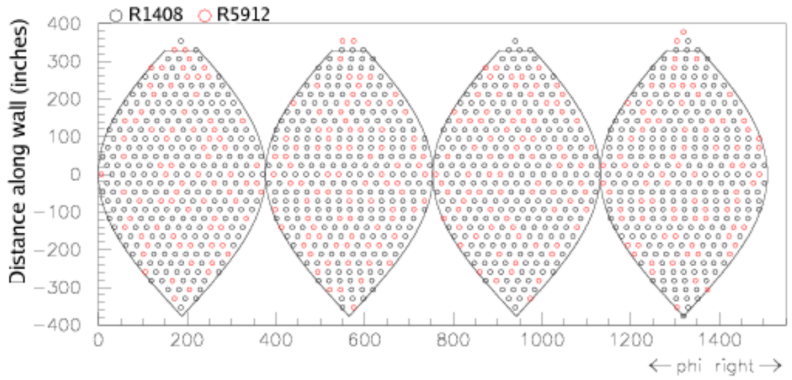

Figure 4.9: Map of PMT locations in main tank. LSND PMTs ($R1408$) shown in black, new PMTs ($R5912$) in red.

4.3.3 Data Acquisition (DAQ), Digitization and Trigger

The MiniBooNE data acquisition system (DAQ) is built from existing LSND hardware, but has been modified to meet the different requirements of MiniBooNE.

A schematic representation of the digitization for one channel shows in Figure 4.10. The pre-amplified PMT signal, V_{pmt}, is integrated in a capacitive circuit located on a charge/time board (QT board), generating a second signal, V_q. If V_{pmt} crosses a threshold corresponding to approximately 0.25 photoelectrons, a discriminator is fired, starting a linear time ramp (V_t). The time signal is also digitized to allow a precise determination of the time at which the PMT signal crossed the threshold. This is necessary since MiniBooNE event reconstruction requires better than $100ns$ time accuracy. Two clock ticks after the PMT signal crosses threshold, the time ramp is reset to baseline.

The charge and time ADC (Analog-to-Digital Converter) values are stored in $204.8\mu s$ circular dual port buffers. If the trigger system (explained below) responds to the stored charge and time, the values are passed on to storage, otherwise they are overwritten. For each PMT hit four consecutive values of V_q and V_t (each of them therefore called a quad) are stored in the buffer. These quads are later used to calculate the charge and time of the hit PMT's, if the event is read out.

4.3.4 The Trigger System

The trigger system collects information from three external triggers (two from the accelerator and one from the calibration systems) and seven comparators (different levels of PMT hit multiplicities) in a 200 ns window. Detail of MiniBooNE external triggers and comparator settings list in Table 4.3.

Input	PMT hits	Purpose
External1	NA	Beam to MiniBooNE
External2	NA	Strobe,NuMI, Debuncher
External3	NA	Calibration Event
Comparator1	Tank hits ≥ 10	Activity Monitor
Comparator2	Tank hits ≥ 24	Michel electron
Comparator3	Tank hits ≥ 200	High-Energy Neutrino
Comparator4	Tank hits ≥ 100	Neutrino candidate
Comparator5	Tank hits ≥ 60	Supernova Neutrino candidate
Comparator6	Veto hits ≥ 6	Cosmic Veto
Comparator7	Veto hits ≥ 4	Cosmic Activity

Table 4.3: MiniBooNE trigger inputs and comparator settings. From Ref. [4].

By setting this trigger any activity in the detector before and after the beam spill is recorded. When the MiniBooNe beam trigger is set, $19.2\mu s$ of data are recorded, beginning $4.6\mu s$ before the beam reach the MiniBooNE target; therefore the detector recorded the total beam-off data $17.6\mu s$ in before and after $1.6\mu s$ beam time. There are also a number of special purpose triggers for calibration (such as the Michel electron, laser, or strobe trigger) or to record various physics event samples (such as the NuMI or supernova trigger). Additionally, there is also a cosmic trigger (Comparator 6 in Table 4.3) which is used to ignore cosmic ray contaminated data during beam up-time.

4.4 The MiniBooNE Calibration Systems

The DAQ system records raw times and charges for each hit in an event without any effects of smearing associated with the DAQ itself. This smearing makes it

necessary to have a calibration system to provide information on PMT charge and time response as well as energy response of the detector. it is critical that the PMTs be properly calibrated in order to determine a particle's energy from the number of photoelectrons detected by the PMTs. The calibration, also, can provide the the relative time response of PMTs and the variation of time response with pulse height (time slewing). This information is crucial for the event reconstruction and particle identification algorithms.

MiniBooNE employs two calibration tools: a laser calibration system and a cosmic ray Muon calibration system. This section describes these methods in some detail.

4.4.1 Laser Calibration System

The primary purpose of the laser system is to calibrate the PMT, electronics, and monitoring the oil property during the MiniBooNE lifetime. The raw charge and time information for each PMT, as described in the previous section, are converted to calibrated charge and time (called gains and time offsets, respectively) using the information provided by analysis of the pulsed laser data, with the known wavelength and intensity.

The laser calibration system consists of a pulsed diode laser and four dispersion flasks, installed at various locations in the detector. Optical fibers connect the laser to the dispersion flasks through which short light pulses ($\leq 100ps$) is transmitted. The dispersion flasks with $10cm$ in diameter, are filled with Ludox colloidal silica to disperse light uniformly. In addition to the four flasks there is also a bare optical fiber that emits light in a cone of about 10^0 opening angle lighting up PMTs in a small circle near the bottom of the detector. Figure 4.11 shows the schematics of MiniBooNE laser calibration system. More detail can be found in Ref. [48].

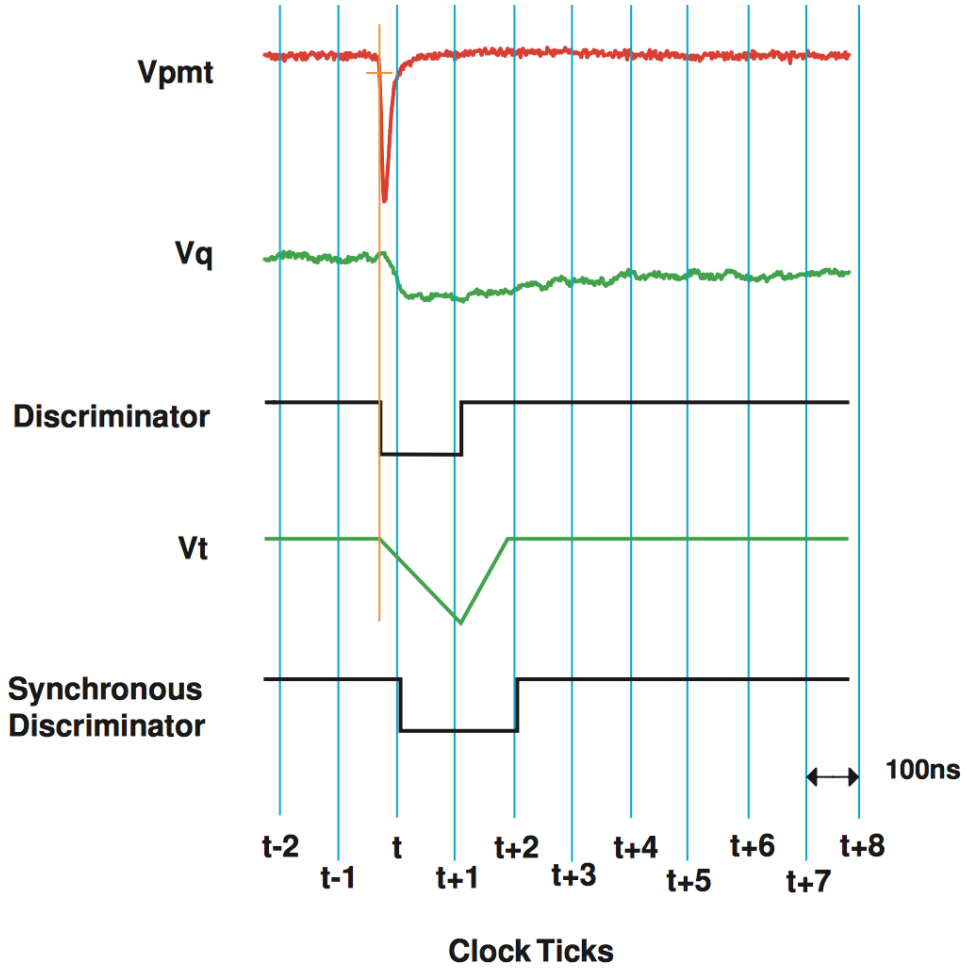

Figure 4.10: Schematic representation of MiniBooNE PMT charge and time digitization []. V_{pmt} is incoming anode signal. Its integral, convolved with an exponential decay, is V_q. The vertical orange line shows the time the discriminator fired. V_t time ramp are started when the anode pulse pass the threshold, and resets after two clocktick passes. DAQ records the four V_q and V_t values at clockticks t-1, t, t+1, and t+2.

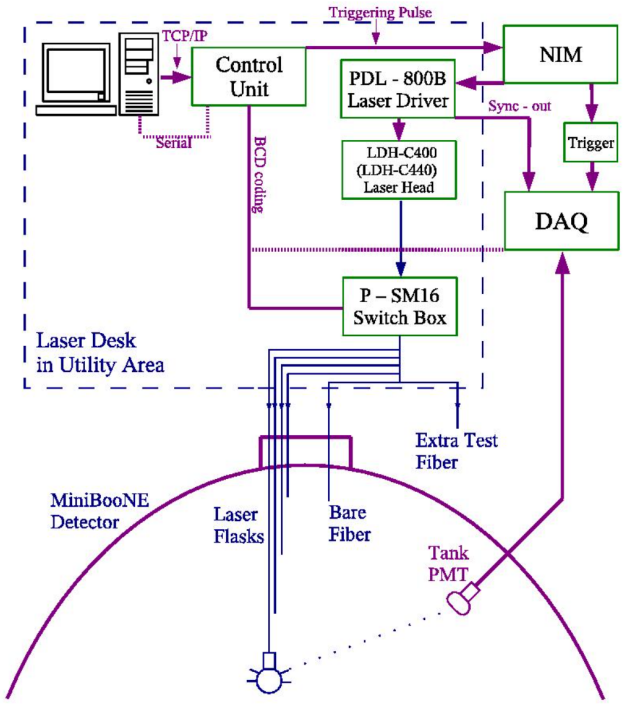

Figure 4.11: MiniBooNE laser calibration system [5].

4.4.2 Cosmic Ray Muon Calibration System

The Cosmic Ray Muon Calibration System provides a precise calibration of the energy, direction, and position of muons for the range of muon energies of primary interest to the experiment (60 to 800 MeV). This calibration system consists of a muon tracker located above the detector, and scintillator cubes located inside the detector. This system uses through-going muons as well as stopping muons and their decay electrons. The stopping muons providing a sample with known origin, direction and path length (thanks to the scintillator cubes).

The muon tracker is a two layer scintillator hodoscope that can provide the information of positions and directions of muons entering the detector. The hodoscope has two layers of plastic scintillator, providing two sets of coordinates by which the position and direction may be determined. Seven optically isolated cubes made of scintillator are situated at various positions in the main volume of the detector, providing additional information for those muons which travel through or stop in them. An optical fiber joined to each scintillator cube is attached at its other end to a 1-inch PMT located outside of the detector for readout. Figure 4.12 shows a schematic diagram of the system for a muon which passes through the muon tracker, stops in a scintillation cube, and decays.

The Cherenkov light produced by the muon is seen by the PMTs as well as the scintillation cube. The decay electrons are also seen by the tank PMTs. Those events where the location and momentum of the muon and the origin of the electron can be determined by the muon hodoscope help in tuning and verifying the reconstruction algorithms.

Absolute Energy Calibration

Muon decay ($\mu^- \rightarrow e^- + \bar{\nu_e} + \nu_\mu$ or $\mu^+ \rightarrow e^+ + \nu_e + \bar{\nu_\mu}$) is a known process. The electron from muon decay (*Michel electrons*) has known shape energy spectrum, MiniBooNE uses this spectrum to determine both the energy scale and energy resolution for low energy electrons. Michel electrons sample, from both stopping cosmic ray muons and muons produced in neutrino interactions, have been collected and analyzed. The measured energy resolution from this large dataset is 14.8% at $52.8\ MeV$.

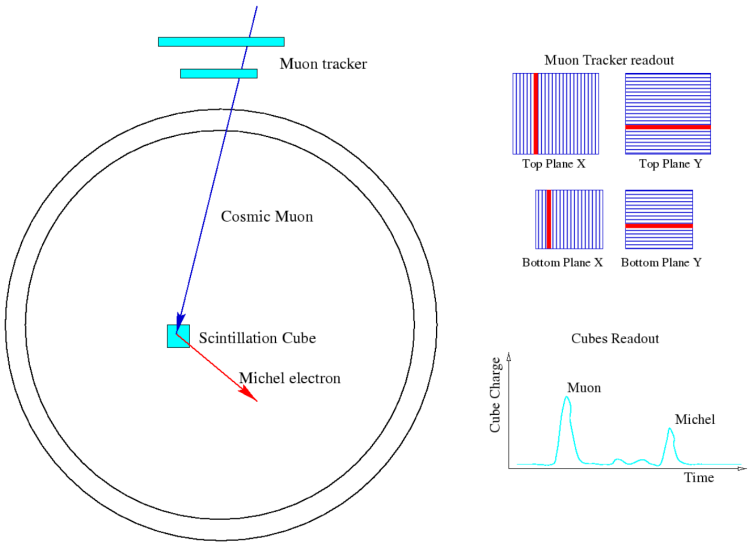

Figure 4.12: A schematic diagram of the muon tracker and a scintillation cube.

Oil Optical Model

The cosmic muon calibration system also is useful to study the detector oil optical model. It provides a clean sample of muons whose exact event topologies are known through measurements that are independent of the PMTs in the detector. This independent information of the muon allows a careful study of the space and timing characteristics of photon emissions from muons spanning a broad range of energies ($15 - 800\ MeV$).

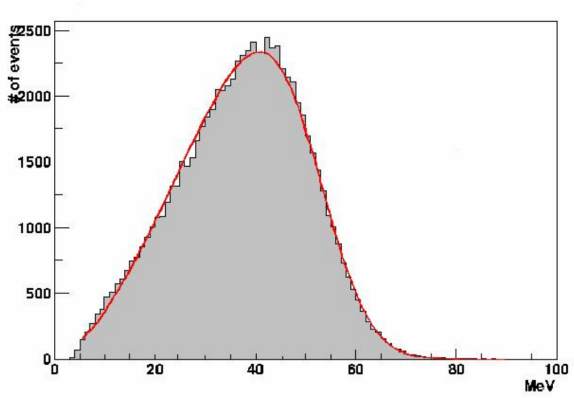

Figure 4.13: Michel electron reconstructed energy spectrum (gray) and the best fit (red), obtained by smearing the Michel electron theoretical energy spectrum with a Gaussian of width proportional to $\sqrt{E}$.

4.5 The MiniBooNE Optical Model

The photomultiplier tubes detect both *Cherenkov* and *scintillation* photons produced by charged particle interactions in the detector. They are sensitive to photons in the wavelength range $280 - 650nm$ as Figure 4.14 shows.

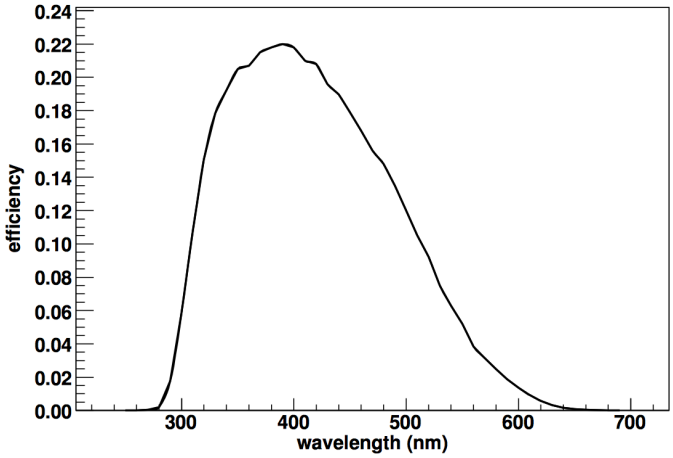

Figure 4.14: Quantum efficiency of $R5912$ PMT obtained from Hamamatsu measurements.

4.5.1 Light production

Chrenkov Light

Cherenkov light is produced in a medium with index of refraction n, when a charged particle travels faster than the speed of light in that medium. Since the speed of light in a medium is dependent upon its index of refraction, the particle must travel with speed $\beta > 1/n$, where $\beta = v/c$, the speed of the particle (v) divided by the speed of light in vacuum (c). In these circumstances, a cone of light is emitted with this property $cos(\theta_c) = \frac{1}{n\beta}$. A schematic of Cherenkov radiation is shown in Figure 4.15. The particle velocity can be expressed by its kinetic energy (T),

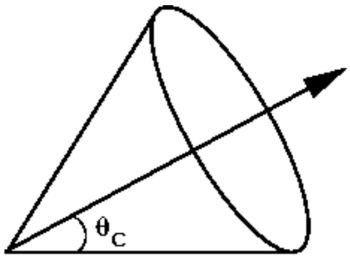

Figure 4.15: Cherenkov radiation

$$cos(\theta_c) = \frac{1}{n\beta} = \frac{1}{n}\Big(\frac{(T+m)^2}{(T+m)^2 - m^2}\Big)^{\frac{1}{2}} \tag{4.1}$$

m is the rest mass of the particle. The minimum kinetic energy to produce Cherenkov light is obtained where $\beta = 1/n$, which gives the Cherenkov kinetic energy threshold as

$$T_{ch} = m\Big(\frac{n}{\sqrt{n^2-1}} - 1\Big) \tag{4.2}$$

with the target oil in the MiniBooNE detector the minimum kinetic energy to produce Cherenkov light is $T_{ch} \approx 350MeV$.

Scintillation Light and Fluorescence

In addition to the Cherenkov light, charged particles traveling through mineral oil can deposit energy and excite the oil molecules. The isotropic, delayed light that is emitted during de-excitation of the molecules is called scintillation light.

Fluorescence is a related process, where the molecules are excited by optical photons instead of charged particles. Like scintillation light, the fluorescence light produced during the de-excitation of the target molecules is isotropic and delayed. The outgoing photons have lower energy than the initial optical photons that excited the molecule.

The characteristics of scintillation and fluorescence (the wavelength spectra and emission spectra) are determined by the chemical composition of the mineral oil. Scintillation and fluorescence light in mineral oil do not follow the dE/dx energy loss distribution which are expected from particles passing through matter.

Instead, the energy loss is higher due to recombination and quenching effects between excited molecules [49]. Birk's law is used to convert ionization energy loss per unit length per unit medium density, dE_{sic}/dx,

$$\frac{dE_{sci}}{dx} = \frac{dE/dx}{1 + k_B(dE/dx)} \tag{4.3}$$

where k_B = 0.014 g/(MeV cm^2) is Birk's constant for mineral oil [50].

4.5.2 Light Transmission

The propagation or transmission of photons in MiniBooNE occurs through processes such as scattering, fluorescence, and absorption.

Scattering

When an optical photon interacts with a target molecule and is deflected and changes its polarization state, the process is known a s scattering. Scattering measurements in the MiniBooNE oil were done externally [51] and are due to Rayleigh and Raman scattering.

Fluorescence

Fluorescence is when optical photons (created by both Cherenkov and scintillation) are absorbed and reemitted later by target molecules at a different wavelength and/or direction. Details of the measurements which was done at Johns Hopkin University are given in Ref. [52].

Absorption

The difference between the total extinction rate and the sum of attenuation due to scattering and fluorescence results into the absorption of photons in oil. Photon attenuation in mineral oil, due to either fluorescent emission, scattering, or absorption, was measured at Fermilab with different experimental setups and over a wide photon wavelength range. The difference between the attenuation rate curve as a function of wavelength obtained by these measurements and the sum of the fluorescence and scattering rates (discussed above), determines the photon absorption in mineral oil.

Scattering, fluorescence, and absorption, were measured and included in the

MiniBooNE GEANT3 simulation [52, 53].

4.6 Event Reconstruction

The process of extracting the information of the event vertex, direction, energy, and time from the times and charges recorded in the PMT is called event reconstruction. In the track based analysis an analytic model (of the light production and propagation in the tank) predicts the probability distribution for charge and time on each PMT which used to construct the likelihood for different particle hypothesis. Prediction has been done to calculate seven track parameters: vertex (x,y,z), time, energy, and direction (θ, and ϕ). MiniBooNE particle track fitter either uses the single track fitter (for electron, muon, and single photon) with 7 fit parameters or two track fitter (π^0), which is actually electron track with double-duty, with 12 fit parameters (two γ from common vertex). In the case of two track fitter MiniBooNE track fitter applied two options of fixed-mass (actual π^0 hypothesis) and free-mass (to calculate π^0 mass reconstruction).

In this section first two simple variables, which are applied to do the event selection, are introduced, then the event reconstruction is discussed briefly, for more details see the Ref. [6].

4.6.1 Hits

Although the information about particle energies is determined by the charge measured by each PMT, the number of PMT fired in each event, called hits, is a good estimate of the total energy deposited in the tank.

4.6.2 Subevent

One event in the data stream corresponds to one beam trigger, or the sequence of the time and charge information from all PMTs in the 19.2μs DAQ window. Since individual particle events in the tank create a group of hits with clustered time values, it is convenient to define a "subevent", or well-separated timing cluster,

to sort out a particular data event into primary and non-primary particles in one event.

4.6.3 Particle track fitter

The charge and time information as well as topological information from individual PMT hits provides particle track information, that can be used to identify the particle in the detector. MiniBooNE uses two reconstruction software packages, the S-Fitter or Stancu fitter and the P-Fitter.

S-Fitter starts with the assumption that the light produced in the detector is due to a point-like source. A chain of reconstruction algorithms providing a number of levels of reconstruction for each event. The three stages of reconstruction are:

- ***StancuFastFit***- The first stage of event reconstruction; a fast single track fitter which provides a rough estimate of the event time and vertex based on a timing likelihood.

- ***StancuFullFit***: The second stage of event reconstruction; a refined single track fitter. The result of the StancuFastFit algorithm is used as input, and the event timing and vertex are more precisely determined using a time and charge likelihood.

- ***StancuPi0Fit***: The third stage of event reconstruction is a two track fitter. The time and vertex information determined by the StancuFullFit algorithm is used as the starting point for this algorithm. Each event is fit under the assumption of two γ rings from the decay of a π^0 with the common vertex. The π^0 meson (with a rest mass of $135\ MeV$) decays after being produced almost immediately (decay time 8.4×10^{-17}s) via two modes of $\gamma\gamma$ (branching fraction 98.987%) and $\gamma e^- e^+$ (branching fraction 1.198%). The resulting photons generate electromagnetic shower in the detector and can emit both Cherenkov and scintillation light. Minimizations can be performed with a constraint on the invariant mass by removing energy of the second photon as a free parameter and setting it via

the relation below:

$$E_2 = \frac{M_{\pi^0}}{2E_1(1 + cos\theta_{\gamma\gamma})} \tag{4.4}$$

where $\theta_{\gamma\gamma}$ is the angle between the photon tracks. This fixed-mass mode is the actual π^0 hypothesis, while the free-mass mode allows for mass reconstruction. All of these algorithms were written by Ion Stancu; all details of each algorithm may be found in the technical notes listed in Ref. [54].

P-Fitter introduces the emission density to go from point-like approximation to track-based fitter. The P-Fitter is better equipped for reconstructing muon tracks than the S-Fitter, and has better resolution in distinguishing π^0 events from electrons, although it runs much slower (≈ 10 times). Both fitters reconstruct electrons with similar resolution.

4.6.4 Particle Identification

Particle identification (PID) comes from ratios of likelihoods from fits to different parent particle hypothesis. The magnetic shock wave conical Cherenkov light produces the ring of light which intersects with the sphere of the PMTs and creates the pattern that are specific to each particle (Figure 4.16). Figure 4.17 is an example of actual event display of a stopping muon candidate event.

Track-Based Particle Identification

The track-based PID algorithm, which is an extension of the P-Fitter (section 4.6.3), fits for electron, muon and pion track parameters and compute likelihood variables L_e, L_μ, and L_{π^0} for each event type based on the ring profiles produced by them (Figure 4.16). In particular, the likelihood ratio is simple, but powerful estimator for particle ID under a hypothesis.

The separation of electrons from muons, or electrons from pions, is achieved by setting a limit on the two PID variables: $\log(L_e/L_\mu)$ and $\log(L_e/L_{\pi^0})$. Moreover, the pion mass cuts required in MiniBooNE to further decrease the background contamination due to process generating π^0 in the final states. 50% signal efficiency and 1% π^0 misidentification rate are obtained by requiring both $log(L_e/L_{\pi^0})$ and $M_{\gamma\gamma}$ in the MiniBooNE $\nu_\mu \rightarrow \nu_e$ oscillation analysis [55]. The

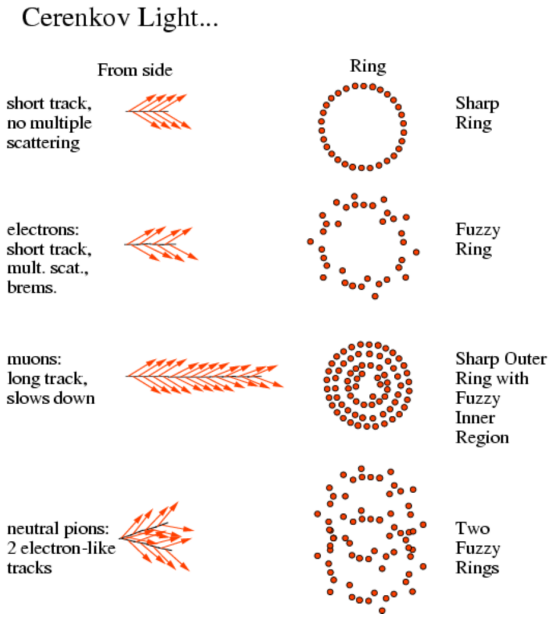

Figure 4.16: A cartoon illustrating PID. PID is done utilizing the features of tracks, originated in the charge, time, and the topological information from all PMTs.

values of the cuts are the quadratic functions in the energy obtained from the single track fitter,

$$log(L_e/L_\mu) > a_0 + a_1 E_e + a_2 E_e^2 \tag{4.5}$$

$$log(L_e/L_{\pi^0}) > a_0 + a_1 E_e + a_2 E_e^2 \tag{4.6}$$

$$M_{\gamma\gamma} < a_0 + a_1 E_e + a_2 E_e^2 \tag{4.7}$$

the coefficients were selected to optimized the oscillation sensitivity, such that the estimated oscillation sensitivity near $\Delta m^2_{12} = 1.0\ eV^2$ and $sin^2 2\theta_{12} = 0.004$ is maximized. The details on computing the oscillation sensitivity can be found in Ref [56].

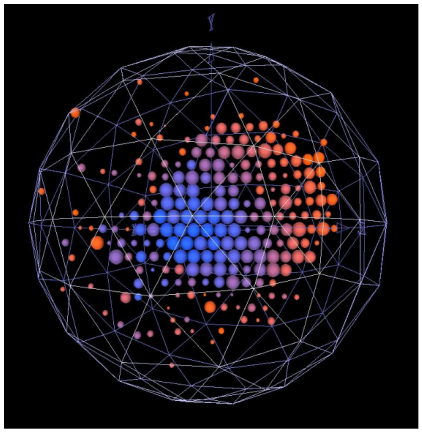

Figure 4.17: An event display for a muon candidate event. Each sphere represents a hit from a PMT, and the size and the color show charge and time information. As described in Figure 4.16, a stopping muon is characterized with sharp edge and filled circle shape hits.

	a_0	$a_1(GeV)$	$a_2(GeV^2)$
$\log(L_e/L_\mu)$	1.3546×10^{-2}	3.4667×10^{-2}	-8.259×10^{-3}
$\log(L_e/L_{\pi^0})$	2.47072×10^{-3}	4.11512×10^{-3}	-2.73785×10^{-2}
$M_{\gamma\gamma}$	3.2033×10^{-2}	7.42657×10^{-3}	2.73787×10^{-5}

Table 4.4: Optimized PID cuts coefficients

The left panel of Figure 4.18 is the scatter plot of $log(L_e/L_\mu)$ as a function of the reconstructed energy of the electron, the black curve indicates the maximized cut value that separates a simulation of ν_e Charge current Quasi Elastic (CCQE) events (blue) from a simulation of ν_μ Charge current Quasi Elastic (CCQE) events (red). The right panel is the scatter plot of $log(L_e/L_{\pi^0})$ as a function of the reconstructed energy of the electron, the black curve indicates the maximized cut value that separates a simulation of ν_e CCQE events from a simulation of Neutral Current process which generating π^0 in the final state (ν_μ NCπ^0). Figure 4.19 shows

the scatter plot of reconstructed mass of π^0 as a function of electron energy with the cut value in black curve that separates a simulation of ν_e CCQE events from a simulation of ν_μ NCπ^0.

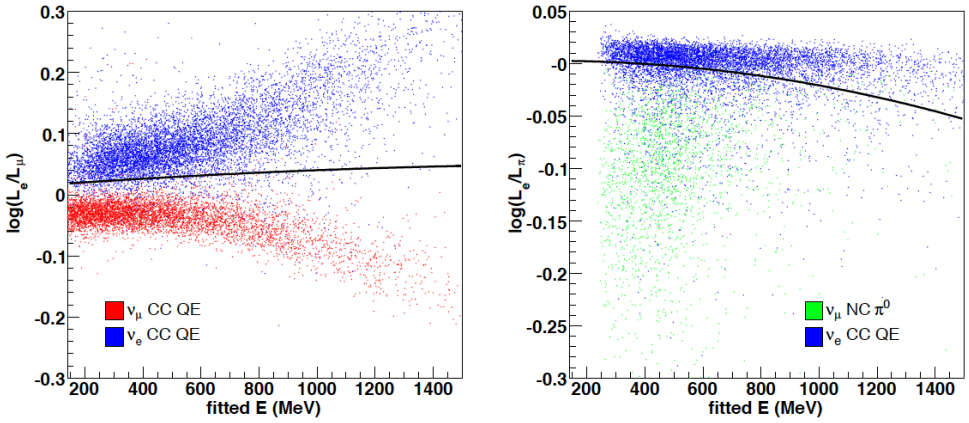

Figure 4.18: On the left, the scatter plot of $log(L_e/L_\mu)$-electron energy used to separate a Monte Carlo simulation of ν_e CCQE events from a simulation of ν_μ CCQE events. On the right, a simulation of ν_e CCQE events is separated from a simulation of ν_μ NCπ^0 events using the PID $log(L_e/L_{\pi^0})$ as a function of electron energy. The value of the cuts selected to optimize the oscillation sensitivity, plots are taken from Ref. [6].

The efficiency of these PID selection of the electron as a function of neutrino energy on ν_eCCQE channel shows in Figure 4.20. It demonstrates how electron identification selection efficiency decrease as a function of neutrino energy.

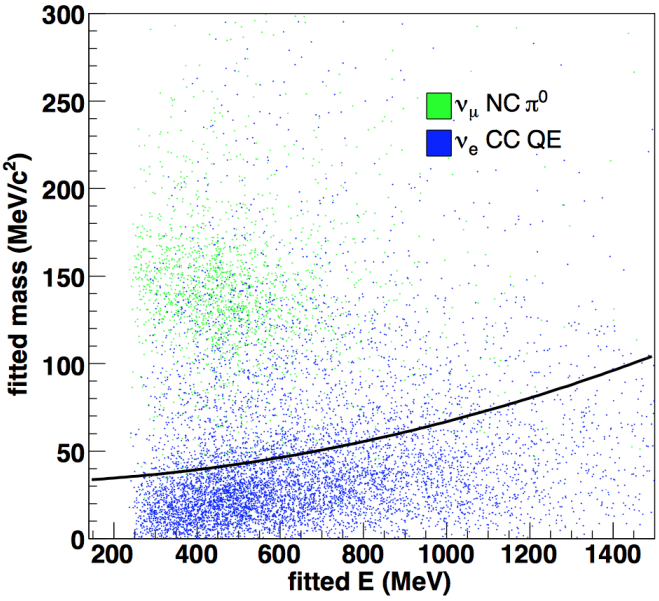

Figure 4.19: The scatter plot of reconstructed mass of π^0 as a function of electron energy used to further decrease the π^0 events in the sample. The black curve shows the cut value to separate the electron of CCQE events from π^0 of NCπ^0 events, plot is taken from Ref. [6].

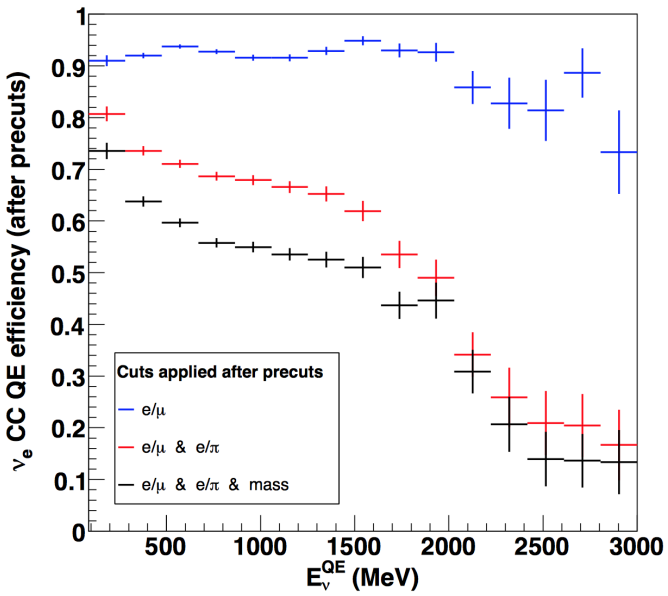

Figure 4.20: The PID and π^0 mass selections efficiency as a function of energy, Ref. [6].

5 The MiniBooNE Simulation

Simulation of measured data in MiniBooNE is performed in several Monte Carlo (MC) steps. First, **BooNEG4Beam** models particle production in proton-beryllium collisions in the MiniBooNE target, secondary particle propagation, and decay to neutrinos.

Second, The neutrino fluxes predicted by BooNEG4Beam are input to **NUANCE** [57], which simulates the neutrino cross sections and generates events.

Third, the interactions modeled by NUANCE are fed into the detector MC simulation with two separated MC, detector simulation (**BoodetMC**) and dirt simulation (**BoodirtMC**). The only difference between detMC and dirtMC is the size of the volume the neutrinos interact; BoodetMC (BoodirtMC) used a radius of $610.6cm$ ($14m$).

Finally, the output of BoodetMC/BoodirtMC passes to a simulation of the data acquisition electronics, **MCthroughDAQ**, where the MC events are output in a form that is identical to MiniBooNE detector data.

This chapter presents the details in various stages of generating events in MiniBooNE detector.

5.1 Beam Monte Carlo

Neutrino flux predictions for all neutrinos relevant to MiniBooNE ($\nu_\mu, \bar{\nu_\mu}, \nu_e, \bar{\nu_e}$) are generated by BooNEG4Beam which is a GEANT4-based MC simulation [58]. In the first step, this program models the geometry and materials (in target hall and decay region) along with the physics processes of mesons production and propagation. In second step, the output of the GEANT4 is fed into another MC program that generates kinematic distributions for the neutrinos from meson decays and generates the final neutrino fluxes at the MiniBooNE detector (Figure 5.1). For more details on the MiniBooNE neutrino flux predictions see Ref. [59].

MiniBooNE neutrino flux is mostly dominated by ν_μ, although some intrinsic ν_e flux is unavoidable. It is important to keep the relative amount of the intrinsic ν_e background as small as possible. The predicted energy dependence of this

intrinsic ν_e background (in Figure 5.1) is different than the energy dependence an oscillation signal (ν_e's with a ν_μ's like energy dependence). The shape difference between the two samples helped much in the oscillation search.

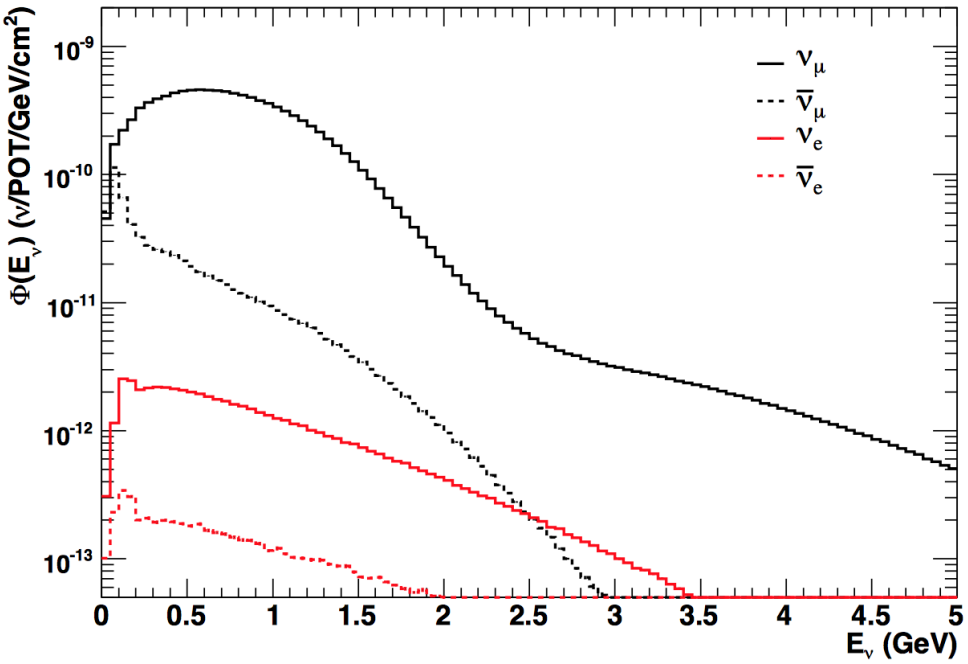

Figure 5.1: The ν-Mode flux as a function of true ν energy predicted by the GEANT4 simulation package. Figure from Ref. [7]

5.2 Neutrino Cross section Model

Neutrino interaction in the MiniBooNE detector are simulated using a neutrino event generator which is based on the NUANCE v3 [57], but it has been tuned to the latest known cross section information from their measurements in MiniBooNE experiments, Table 5.2 lists the cross section parameters used to customize the simulation to MiniBooNE detector. The neutrino flux prediction is fed into the NUANCE generator and it simulates 99 distinct neutrino/antineutrino interactions

in the mineral oil target (CH_2 with a density of $0.845\frac{g}{cm^3}$). Tables 5.1 list the interaction processes simulated by NUANCE along with the channel numbers.

Grouping NUANCE channels

To make it easier to illustrate the background and signal channel in the analysis, 99 NUANCE interactions grouped into 16 channels which show in Table 5.3.

#	CC / NC	Reaction
Cabibbo–allowed quasi–elastic scattering from nucleons		
1	CC	$\nu_\mu n \to \mu^- p$ $(\overline{\nu}_\mu p \to \mu^+ n)$
(Quasi–)elastic scattering from nucleons		
2	NC	$\nu_\mu n \to \nu_\mu n$ $(\overline{\nu}_\mu n \to \overline{\nu}_\mu n)$ $\nu_\mu p \to \nu_\mu p$ $(\overline{\nu}_\mu p \to \overline{\nu}_\mu p)$
Resonant single pion production		
3	CC	$\nu_\mu p \to \mu^- p\pi^+$
4	CC	$\nu_\mu n \to \mu^- p\pi^0$
5	CC	$\nu_\mu n \to \mu^- n\pi^+$
6	NC	$\nu_\mu p \to \nu_\mu p\pi^0$
7	NC	$\nu_\mu p \to \nu_\mu n\pi^+$
8	NC	$\nu_\mu n \to \nu_\mu n\pi^0$
9	NC	$\nu_\mu n \to \nu_\mu p\pi^-$
10–16		Corresponding $\overline{\nu}_\mu$ processes
Multi–pion resonant processes		
17	CC	$\nu_\mu p \to \mu^- \Delta^+ \pi^+$
18	CC	$\nu_\mu p \to \mu^- \Delta^{++} \pi^0$
19	CC	$\nu_\mu n \to \mu^- \Delta^+ \pi^0$
20	CC	$\nu_\mu n \to \mu^- \Delta^0 \pi^+$
21	CC	$\nu_\mu n \to \mu^- \Delta^{++} \pi^-$
22	NC	$\nu_\mu p \to \nu_\mu \Delta^+ \pi^0$
23	NC	$\nu_\mu p \to \nu_\mu \Delta^0 \pi^+$
24	NC	$\nu_\mu p \to \nu_\mu \Delta^{++} \pi^-$

#	CC / NC	Reaction
25	NC	$\nu_\mu n \to \nu_\mu \Delta^+ \pi^-$
26	NC	$\nu_\mu n \to \nu_\mu \Delta^0 \pi^0$
27	NC	$\nu_\mu n \to \nu_\mu \Delta^- \pi^+$
28–38		Corresponding $\overline{\nu}_\mu$ processes
39	CC	$\nu_\mu p \to \mu^- p\rho^+(770)$
40	CC	$\nu_\mu n \to \mu^- p\rho^0(770)$
41	CC	$\nu_\mu n \to \mu^- n\rho^+(770)$
42	NC	$\nu_\mu p \to \nu_\mu p\rho^0(770)$
43	NC	$\nu_\mu p \to \nu_\mu n\rho^+(770)$
44	NC	$\nu_\mu n \to \nu_\mu n\rho^0(770)$
45	NC	$\nu_\mu n \to \nu_\mu p\rho^-(770)$
46–52		Corresponding $\overline{\nu}_\mu$ processes
53	CC	$\nu_\mu p \to \mu^- \Sigma^+ K^+$
54	CC	$\nu_\mu n \to \mu^- \Sigma^0 K^+$
55	CC	$\nu_\mu n \to \mu^- \Sigma^+ K^0$
56	NC	$\nu_\mu p \to \nu_\mu \Sigma^0 K^+$
57	NC	$\nu_\mu p \to \nu_\mu \Sigma^+ K^0$
58	NC	$\nu_\mu n \to \nu_\mu \Sigma^0 K^0$
59	NC	$\nu_\mu n \to \nu_\mu \Sigma^- K^+$
60–66		Corresponding $\overline{\nu}_\mu$ processes
67	CC	$\nu_\mu n \to \mu^- p\eta$
68	NC	$\nu_\mu p \to \nu_\mu p\eta$
69	NC	$\nu_\mu n \to \nu_\mu n\eta$
70–72		Corresponding $\overline{\nu}_\mu$ processes
73	CC	$\nu_\mu n \to \mu^- K^+ \Lambda$
74	NC	$\nu_\mu p \to \nu_\mu K^+ \Lambda$
75	NC	$\nu_\mu n \to \nu_\mu K^0 \Lambda$

#	CC / NC	Reaction
76–78		Corresponding $\overline{\nu}_\mu$ processes
79	CC	$\nu_\mu n \to \mu^- p\pi^+\pi^-$
80	CC	$\nu_\mu n \to \mu^- p\pi^0\pi^0$
81	NC	$\nu_\mu p \to \nu_\mu p\pi^+\pi^-$
82	NC	$\nu_\mu p \to \nu_\mu p\pi^0\pi^0$
83	NC	$\nu_\mu n \to \nu_\mu n\pi^+\pi^-$
84	NC	$\nu_\mu n \to \nu_\mu n\pi^0\pi^0$
85–90		Corresponding $\overline{\nu}_\mu$ processes
Deep Inelastic Scattering		
91	CC	$\nu_\mu N \to \mu X$
92	NC	$\nu_\mu N \to \nu_\mu X$
93–94		Unused
95	CC	Cabibbo–supp. QE hyperon production: $\overline{\nu}_\mu p \to \mu^+ \Lambda$ $\nu_\mu n \to \mu^+ \Sigma^-$ $\overline{\nu}_\mu p \to \mu^+ \Sigma^0$

#	CC / NC	Reaction
Coherent / diffractive π production		
96	NC	$\nu_\mu A \to \nu_\mu A\pi^0$ $(\overline{\nu}_\mu A \to \overline{\nu}_\mu A\pi^0)$
97	CC	$\nu_\mu A \to \mu^- A\pi^+$ $(\overline{\nu}_\mu A \to \mu^+ A\pi^-)$
ν–e elastic scattering		
98	–	$\nu_\mu e \to \nu_\mu e$ $(\overline{\nu}_\mu e \to \overline{\nu}_\mu e)$
ν–e inverse μ decay		
99	CC	$\nu_\mu e \to \mu^- \nu_e$

Table 5.1: Processes available within NUANCE (continued from the previous page). The numbers in the left most column indicate the assigned reaction code (channel number) in NUANCE.

Parameter	Value
M_A for QE events on carbon	1.2341 GeV
Binding energy for carbon	34.0 MeV
Fermi momentum for carbon	220.0 MeV
Δs, the axial vector iso-scalar term	0.0
M_A for CC and NC single pion events	1.1 GeV
M_A for CC and NC multiple pion events	1.3 GeV
Scale factor for NC coherent π^0 events	1.302
Scale factor for NC and CC Δ radiative events	1.00
Scale factor for deep inelastic scattering events	1.0
Pauli blocking scale factor, κ	1.0220
M_A for for CC single coherent events (not coherent NCπ^0)	1.030GeV
Scale factor for NC resonant π^0 events	1.00
M_A for QE events on hydrogen	1.13GeV

Table 5.2: Cross-section parameters used in the MiniBooNE MC. Here the abbreviations are: QE = quasi-elastic, NC = neutral current, and CC = charge current.

Channels	description
NCπ_0	Neutral current generate π^0 in the final state
CCπ_0	Charge current generate π^0 in the final state
NC$\pi^{\pm}$	Neutral current generate π^+ or π^- in the final state
CCπ^+	Charge current generate π^+ in the final state
NCπ^+ π^-	Neutral current generate π^+ and π^- in the final state
CCπ^+ π^-	Charge current generate π^+ and π^- in the final state
NCπ_0's	Neutral current generate more than one π^0 in the final state
CCπ_0's	Charge current generate more than one π^0 in the final state
NC>2π	Neutral current generate more than two πs in the final state
CC >2π	Charge current generate more than two πs in the final state
NC-DIS	Neutral current deep inelastic scattering
CC-DIS	Charge current deep inelastic scattering
NC-Els	Neutral current elastic scattering
CCQE	Charge current Quasi Elastic
resonant processes >2π	resonant processes generate more than two πs in the final state
Signal	electron - ν elastic scattering

Table 5.3: Grouping 99 NUANCE channels to 16

NUANCE Neutrino Cross Section Model

The relevant physics models that are implemented by NUANCE list as following:

- the Llewellyn-Smith expression for the quasi-elastic cross section on free nucleons [60],
- the Rein and Sehgal resonance cross sections [61],
- the Bodek-Yang [62] deep inelastic scattering (DIS) cross section at large invariant mass, W , and momentum transfers, Q^2,
- the Smith-Moniz relativistic Fermi gas model for quasi-elastic scattering from nucleons bound inside a nucleus.

We discuss only some sets of the interaction types briefly here, with concentrating on those which consist of the most dominated background populations in this analysis. A full description of these and other interactions modeled in NUANCE can be found in Ref. [57].

5.2.1 Charged Current Elastic Scattering (CCQE)

NUANCE channel$\#1$ corresponds to CCQE interactions which make up $\approx 29\%$ of the final sample for this analysis (Table 6.3). The neutrino CCQE interaction happens off neutrons ($\nu_\mu + n \rightarrow \mu^- + p$) in the bound carbon atom, so the Smith-Moniz relativistic Fermi gas model used to generate it. On the other hand the antineutrino CCQE happens off protons ($\bar{\nu_\mu} + p \rightarrow \mu^+ + n$) which are both free Hydrogen atom and bound Carbon atom, so a combination of the Llewellyn-Smith and Smith-Moniz formalism is used.

The vector form factors are taken from Ref. [63], while other form factors are customized for MiniBooNE (Table 5.2); the axial vector mass for the bound (free) nucleons $M_A = 1.2341(1.13)\ GeV$ increased from the original values to cover the data excess observed in CCQE cross section measurement; on the other hand, a Pauli blocking scaling parameter $\kappa = 1.022$ is used here to fix the data deficit in low energy events, it modifies the shape of the CCQE cross section at low values of momentum transfer by scaling the energy of initial nucleon. See Ref. [64] for details.

5.2.2 NC Single Pion Production

NUANCE channel$\#6-9(10-16)$ for neutrino (antineutrino) corresponds to NC single π interactions, among these seven interactions NCπ^0 is major background for this analysis with $\approx 15\%$ of the final sample (Table 6.3). The simulation of single pion production is based on Rein and Sehgal's model. In neutrino-nucleus interactions single pion production happens when a nucleon is excited to a resonant state and decays to a pion and a nucleon. One difference between the original Rein and Sehgal paper and the NUANCE implementation is that the NUANCE model has been further updated to include improved the baryon masses and additional non-strange resonances up to $2\ GeV$ [57]. Additionally, there are extra reaction included that reduce the number of pions produced in the final state. The pions may experience absorption in the nucleus through final state interactions (FSI) in which case the final product of the interaction is a nucleon, similar to the NC-Els interaction. MiniBooNE has tuned NUANCE to assign a probability of about 20% that the outgoing pion is absorbed.

5.2.3 Multiple Pion Production

NUANCE channel$\#17-90$ for neutrino and antineutrino corresponds to interactions in which multiple pions are produced in the final state. These interactions are simulated in NUANCE using a combination of resonant and DIS production mechanisms. Resonant states are treated by the Rein and Sehgal model up to $\approx 2\ GeV$. Deep inelastic scattering events follow the Bodek-Yang theory. All of the reactions in this category present in Table 5.1. Among all of the resonant productions the baryonic resonance interaction is the primary source of one pion production for MiniBooNE,

$$\nu_\mu + p \rightarrow \Delta^{++} \rightarrow \mu^- + \pi^+ + p$$
$$\nu_\mu + n \rightarrow \Delta^{+} \rightarrow \mu^- + \pi^+ + n, etc\ldots$$

The original code of NUANCE was modified to take into account the pion angular distribution due to the spin structure of the resonance states [65]. All resonant

interactions are used to contribute to the invariant mass $W < 2\ GeV$, but the $\Delta(1232)$ resonance dominates at this energy scale.

5.2.4 Final State Interactions (FSI)

Particles produced in neutrino interactions with CH_2 have the chance to re-interact before exiting the nucleus. The "final state interactions" (FSI) is used here to describe interactions that might transform the topology of an event. NUANCE simulates FSI by tracking hadrons through the nucleus in steps of $0.2fm$, calculating an interaction probability at each step. The probability for interaction is based on measured π-N cross sections and angular distributions. This effect results in several interaction of particles and their interaction products before exiting the nucleus. The final state interactions modeled by NUANCE that change the pion production include:

- **absorption**: a pion disappears inside the nucleus,
- **charge exchange**: include one of these interaction - $\pi^+ n \rightarrow \pi^0 n, \pi^0 n \rightarrow \pi^+ n, \pi^0 n \rightarrow \pi^- p, \pi^- p \rightarrow \pi^0 n$,
- **elastic and inelastic (re)scattering**: a pion maintains its identity, but is deflected,
- **recoiling nucleon scattering**: a nucleon may rescatter and produce pions in the final state, or rescatter several times until it reaches the surface of the nucleus, producing multiple nucleons in the final state,
- **nuclear de-excitation**: the nucleus is excited to a higher energy level; it decays electromagnetically to its ground state via the emission of a few-$MeV\gamma$.

Among all the FSI, charge exchange and nuclear de-excitation are the most important processes contributing to the uncertainty in this analysis, because they results may mimic the same final state as electron neutrino elastic scattering with low energy electron in which only one photon distinguished as the electron. The contamination of this process in the final selection presents in section 6.5.

5.3 The MiniBooNE Detector Monte Carlo

The simulation of the MiniBooNE detector (a GEANT3-based program [43]) takes the events generated by NUANCE to model particle propagation. BoodetMC assigns a density-weighted interaction vertex, once the vertex location is decided, the simulation takes the final state particles generated by NUANCE and steps them through the detector, accounting for the detector and tracked particles properties along with the oil optical model parameters. Some modifications to the standard routines include an improved model for decay ($\pi^0 \rightarrow e^- e^+ \gamma$), muon decay ($\mu \rightarrow e\nu\nu$), and the possibility of μ^- capture by carbon. the default hadronic interactions in GEANT(GHEISHA) modified to GFLUKA hadronic interaction model.

Among all oil optical model parameters and PMT parameters here is the list of the most effective ones:

- Reflection coefficients for white and black surfaces
- PMT quantum efficiency parameters: from Hamamatsu, corrected for air-glass reflection
- PMT relative efficiency as a function of angle relative to the PMT axis
- Oil refractive index and group velocity parameters
- Oil attenuation length from $250 - 650nm$ in steps of $5nm$
- Polarization-dependent Rayleigh scattering
- Scale rates and lifetimes of individual fluorophores

The number of Cherenkov and scintillation photons and their hit times are recorded for each final state particle. These quantities feed to the reconstruction algorithms. Also, the "truth" information for each final state particle (like 4-momentum, vertex, creation time, interacting neutrino type) is recorded for the cross check and computing the systematic errors.

The final step, a FORTRAN program called MCthroughDAQ, smears hit times and charges to determine these quantities at the PMT anode. This last step generates simulated events just like the true detector data. The details on the data acquisition electronics discussed in section 4.3.3 of previous chapter.

6 Data Reduction and Event Selection

6.1 Introduction

This chapter describes the selection processes that yields the event sample used to calculate a neutrino electron elastic scattering cross section in MiniBooNE. As we mathematically showed in section (3.3) the relative small mass of electron to neutrino's energy results in the outgoing electrons scattering in the extremely forward direction with low energy. Figure 6.1 shows the reconstructed electron energy and direction distribution of simulated neutrino electron elastic scattering channel in MiniBooNE, illustrating these features. Furthermore, due to small cross section of the interaction (details in section (3.2)) the number of signal events are a small fraction of the overall number of neutrino events collected, so background rejection is very important to identify the signal. Therefore the goal of the selection is to refine the sample to enhance the signal based on the interaction features and the properties of the detector.

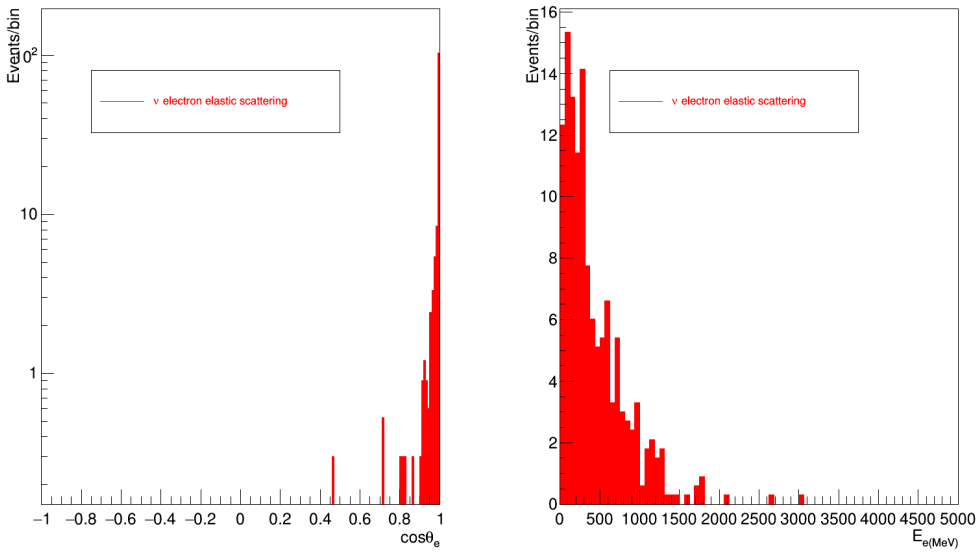

Figure 6.1: On the left (right) shows the electron angle (energy) distribution

6.2 Data Sample

Figure 6.2 shows the neutrino per POT stability plot while MiniBooNE collecting data from 2001 to 2017.

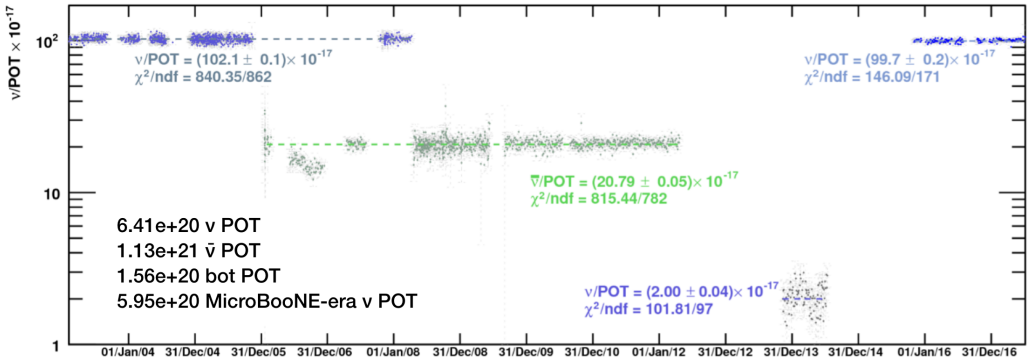

Figure 6.2: Neutrino pre POT stability plot from 2001 to 2017 (the period of 2013 to 2014 shows the bot POT, where MiniBooNE was running on off-target mode).

The MiniBooNE experiment began collecting data in 2001 and reported the neutrino mode oscillation ($\nu_\mu \rightarrow \nu_e$) search result in 2007 [66]. In the first ν-mode run it collected 6.41×10^{20} Proton On Target (POT).

Subsequently it ran in the antineutrino mode looking for $\bar{\nu}_\mu \rightarrow \bar{\nu}_e$ oscillations, which was a search to confirm the LSND result [67]. The initial antineutrino mode results were published in 2010 [68]. MiniBooNE continued running in antineutrino mode till 2012 and collected 1.13×10^{21} POT. Running for a decade in both neutrino and antineutrino mode, MiniBooNE successfully accomplished its primary goals and produced measurements that confirmed the oscillation analysis of the LSND signal.

Since systematic uncertainties dominated the total measurement errors more statistics in either neutrino or antineutrino mode may not provide significant new information on the question of oscillations. On the other hand, MiniBooNE detector had the capability for continued stable operation for many years, so the collaboration decided to take advantage of the stability of detector and started running on off-target (dark matter) mode as the first proton beam-dump light dark

matter search to look for light sub-GeV dark matter. it collected 1.86×10^{20} POT from 2013 to 2014, in this mode.

MiniBooNE ran on off-target mode till MicroBooNE began operation, then it switched to neutrino mode along with MicroBooNE running (MicroBooNE-era). This second ν-mode run resulted in 5.95×10^{20} POT (the data was processed in two separated set based on the year of collection, 2.92×10^{20} POT till August 2016, and 3.03×10^{20} POT till August 2017). The data used in this thesis is all the ν-mode data which are collected from the first run and the MicroBooNE-era run with the total 12.36×10^{20} POT. As mentioned earlier the small fraction of the signal events compare to overall number of neutrino events in MiniBooNE makes this analysis sensitive to statistical fluctuations, but this last ν-mode run with adding twice more data eases the problem.

The data collected in MiniBooNE-era ν-mode run, after dark matter mode, had the same configuration as the first run. The stability of data demonstrates in Figure 6.3, by showing that the electron angle (energy) distribution of observed data collected in two ν-mode did not change.

6.3 Analysis Cuts

In order to isolate a sample of electron neutrino elastic scattering events we perform a series of analysis cuts. The selections are on the experimental variables, like PMT charge, time or reconstructed electron angle, which differentiates the electron neutrino elastic scattering events from other events in the MiniBooNE sample. In order to keep the consistency with the electron oscillation analysis we maintain the same selection cuts in this dissertation. The cross section of signal process ($\nu_\mu \, e^- \rightarrow \nu_\mu \, e^-$) has a strong dependency on the reconstructed angle and energy of electrons (details in chapter 3). Therefore It is crucial to monitor the distribution of reconstructed angle and energy after applying the selection cuts to insure that we are not shaping the distributions.

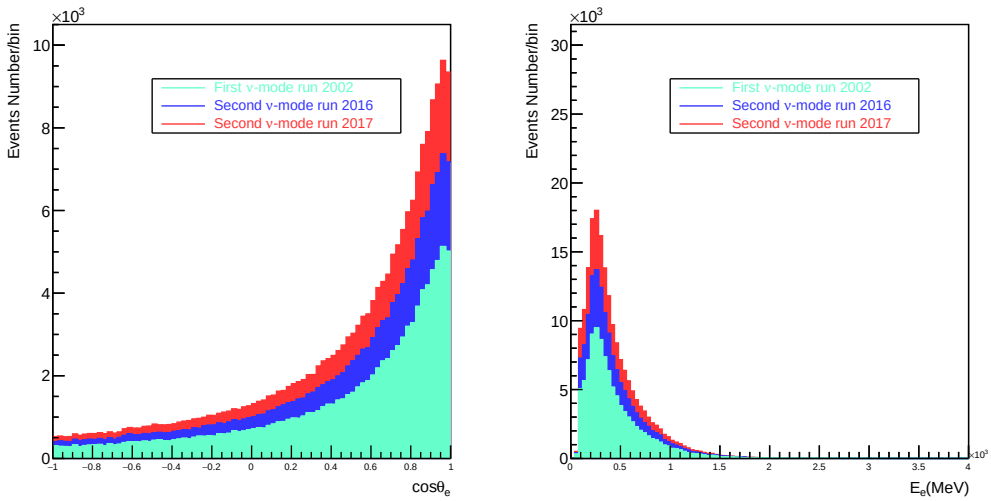

Figure 6.3: The electron angle (energy) distribution of observed data on the left (right) after applying the preselection cuts except for direction.

6.3.1 Event Preselection

The selection of neutrino electron elastic scattering events from the beam data starts with a set of precuts to identify potential electrons in the forward direction. Table 6.1 shows the expected number of events from beam related background, dirt background and signal channels after applying the preselection cuts one-by-one sequentially.

	onese AND (cosθ > 0.9)	Thit	Vhit	Time Window	$R_{electron}$
Signal	126.93	103.07	103.07	103.07	76.7
Beam-Background	6.11×10^4	4.01×10^4	4.01×10^4	4.01×10^4	3.34×10^4
Dirt	1.06×10^4	1.25×10^3	925.10	879.83	390.55
Data	NA	NA	NA	NA	3.7×10^4

Table 6.1: Number of events after applying the preselection cuts subsequently.

The preselection cuts are listed bellow:

1. ***Single subevent (onese)***
   One subevent is a criteria (section 4.6.2) which applied to reject electrons from muon decay when the electron and muon both produce electron subevent in the beam window. Since we expect to observe only the electron from the ν_μ $e^- \rightarrow$ ν_μ e^- interaction this cuts can rejects the electron in the second subevent.
2. ***Direction cut*: $\cos\theta_e$ > 0.9**
   The direction cut is motivated by the kinematic of the electron neutrino elastic scattering, the details discussed in section 3.3, equation 3.14 shows that electron neutrino events are strongly peaked at low angle.
3. ***Tank hit (Thit) > 200***
   The tank hits cut requires to ensures that the event is sufficiently energetic. The left panel of Figure 6.4 shows the tank hit distribution for various channels in the analysis, it demonstrates how adding tank hit to one subevent and direction cuts reduces the Neutral Current Elastic Interactions (NC-Els) events with high efficiency. The right panel shows dependency of the tank hit variable on the electron energy. It presents how this selection cuts the events with the energy less than $50\ MeV$. Since the Michel electron spectrum stops at the average energy of $52.8\ MeV$ (Figure 4.13), the tank hit cut excludes virtually all Michel electron events.
4. ***Veto hit (Vhit) < 6***
   The veto hit (the number of hits in the veto region) cut is to demand that the events contained within the main tank volume is consistent with a neutrino interaction inside the tank. By requiring that the veto hits is less than 6, we can rejects almost all of the particles that leave the fiducial volume.
5. ***Beam trigger window***
   The beam trigger window cut is based on the observed time distribution for the CCQE process. Figure 6.5 shows the Monte Carlo simulation in time distribution of the CCQE first subevent, it shows that most beam related interactions occur between 4550 ns and 6250 ns. Using as narrow a time window as possible helps reduce the rate of cosmic ray events in the data sample.

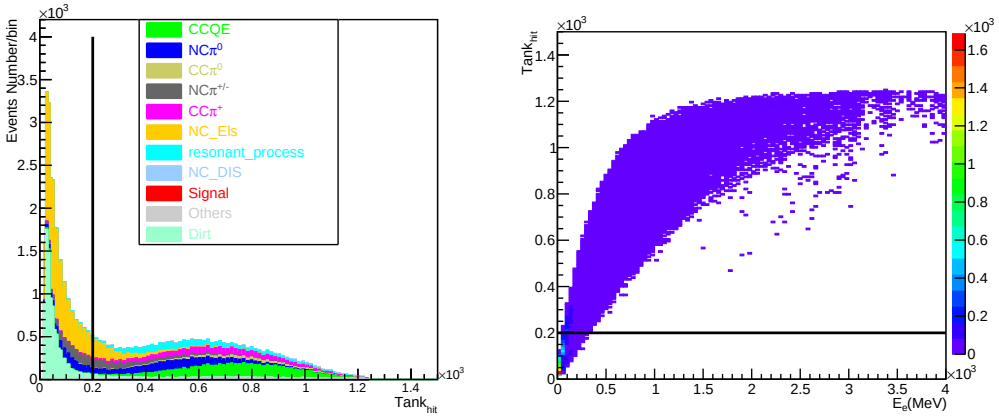

Figure 6.4: Left panel shows tank hit distribution of various channels in MiniBooNE, right panel shows how the tank hit depends on electron energy. The distributions presents the events number after applying the single subevent and direction cuts

6. ***Electron event vertex cut*** $R_{electron} < 500cm$

   The radial location of the reconstruction electron event vertex ($R_{electron}$) cut keeps events away from the tank edge. The $500\ cm$ requirement is the usual fiducial cut used in MiniBooNE to ensure that events are contained in the detector, within the region where they can be accurately reconstructed.

The last column of Table 6.1 presents the expected number of events in comparison with the observed data events after applying all preselection cuts, the preselection cuts results in $8.5 \pm 0.02\%$ more observed data events than what is expected from Monte Carlo. In the next chapter we show this excess is due to the overall flux error in the analysis. Figure 6.6 shows the stack electron angle (energy) distribution after applying the preselection cuts.

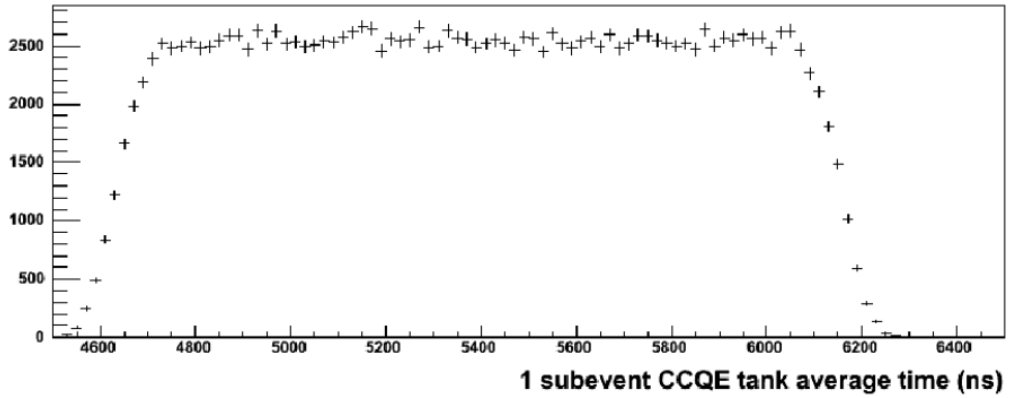

Figure 6.5: The time distribution of the CCQE first subevent is shown to be between 4550 and 6250 ns. We expect this situation to be identical for ν_μ e^- events.

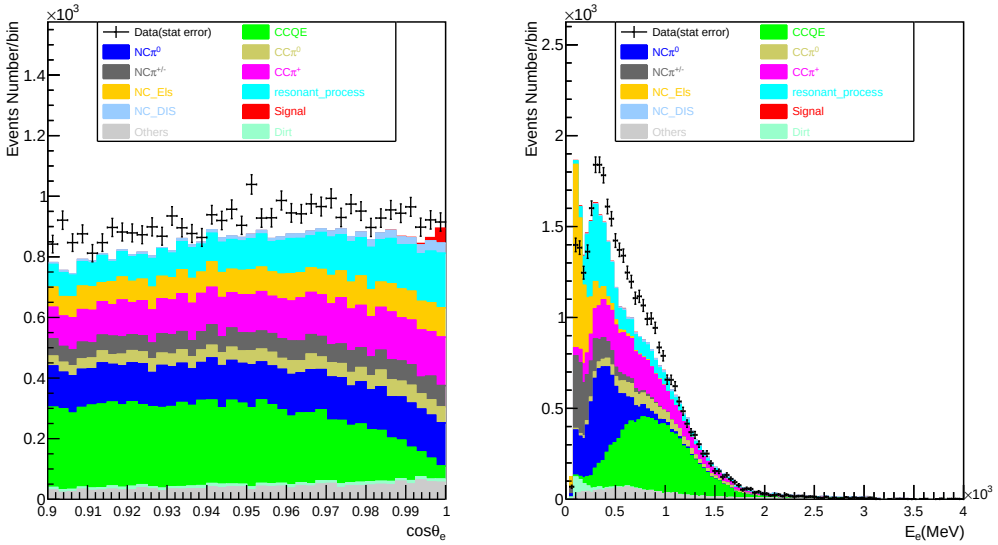

Figure 6.6: The stack electron angle (energy) distribution on the left (right) for various channels in MiniBooNE along with data with its statistical error after applying preselection cuts.

6.3.2 Further Event Selection

The selection of neutrino electron elastic scattering events from the beam data continues with a set of specific cuts to extract potential electrons in the sample. Table 6.2 shows the expected number of events from beam related background, dirt background and signal channels in comparison with observed data after applying the further selection cuts. The last column shows the number of the expected events and observed data in the region of the signal, note that this selection is not included in this analysis. The last row presents the efficiency of each cut where computed by the fraction of the number of the signal events after applying the cut to the number of the signal events form the previous cut. The total efficiency of the cuts is then 28%.

The cuts are listed below:

1. μ ***endpoint < 488 cm***
   The location of the track endpoint is another cut in addition to $R_{electron}$ to keep the events away from the tank edge where they can be reconstructed better.
2. ***Particle identification (PID) cuts***
   We used the same cuts as for the MiniBooNE oscillation analysis (equations 4.5 to 4.7) to select electron neutrino elastic scattering events and remove background events with μ and π^0 in the final state. The efficiency of the PID sets of cuts for the signal channel in this analysis shows in Figure 6.7. The left (right) panel shows the efficiency as a function of electron angle (energy). It should be noted that plots show only the bins in which signal events are available. The large error bars are due to limited MC statistics.

	precuts	μ endpoint	log(L_e/L_μ)	log(L_e/L_π)	π^0 Mass	RtoWall	cosθ_e > 0.99
Signal	76.7	59.86	55.65	46.92	42.11	35.19	30.68
Beam-Background	3.34×10^4	2.44×10^4	1.04×10^4	752.98	454.46	400.64	47.09
Dirt	390.55	361.41	252.48	139.74	123.26	26.28	3.82
Data	3.7×10^4	2.7×10^4	1.1×10^4	1.1×10^3	725	560	107
Cut Efficiency	60%	78%	93%	84%	90%	84%	87%

Table 6.2: Number of events by applying the cuts one-by-one independently.

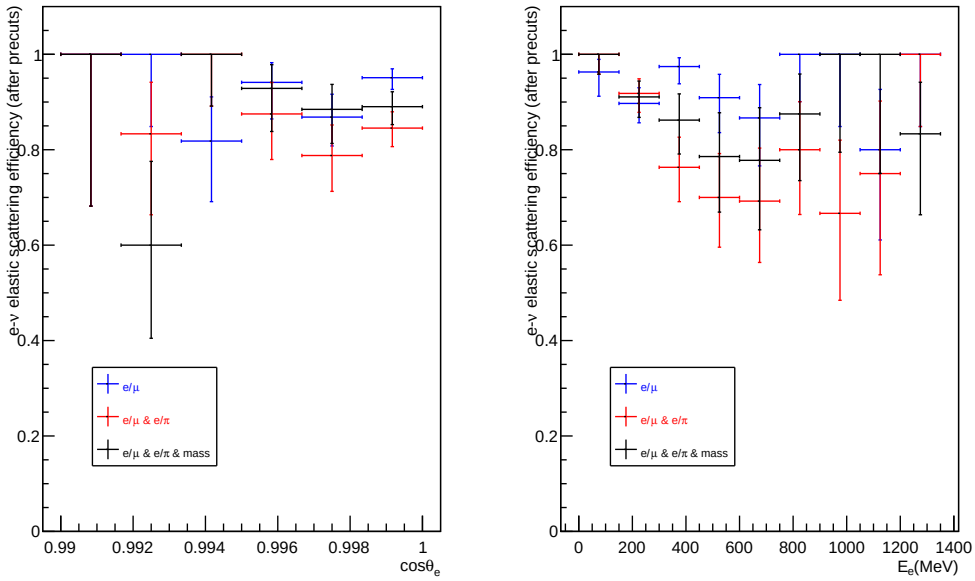

Figure 6.7: The efficiency of particle identification selection as a function of electron angle (left) and energy (right).

3. ***Distance to the wall, backward*** (RtoWall$_{backward}$)

   RtoWall$_{backward}$ > 347.3 - 0.595 E_e and RtoWall$_{backward}$ < 9999.0.

   The RtoWall cut applied to excluded the events generated in dirt outside the detector and detected inside it. Photons produced in the dirt events can penetrate the veto region and find their way into the main tank. They constitute an important source of background because they could easily be misidentified as low energy electrons. Figure 6.8 shows a cartoon representation of an interaction in which a single γ arising from π^0 decay enters the detector. In order to measure the rate of dirt events in the data, MiniBooNE used a Monte Carlo sample of events generated outside the tank and applied a cut on a reconstructed quantity that measures the distance of the event vertex to the wall of the tank in the backward direction. This quantity often called Rtowall is defined as:

   $$\text{RtoWall} = \overrightarrow{R}_{\text{events}}.\overrightarrow{U}_{\text{events}} + \left((\overrightarrow{R}_{\text{events}}.\overrightarrow{U}_{\text{events}})^2 - |\overrightarrow{R}_{\text{events}}|^2 + |R_0|^2\right)^{1/2}.$$

   where $\overrightarrow{R}_{events}$ represents the reconstructed event-vertex, while $\overrightarrow{U}_{events}$ is the reconstructed direction. Here R_0 is the radius of the fiducial sphere which set to $550cm$.

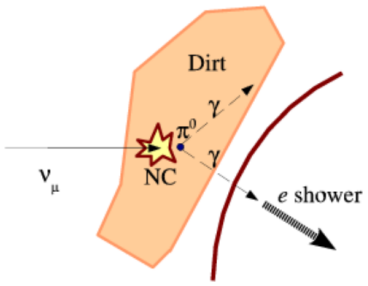

Figure 6.8: A cartoon representation of a photon from the decay of a π^0 event produced from the interaction of neutrinos with the dirt outside the detector.

Figure 6.9 shows the scatter plot of RtoWall as a function of the reconstructed energy of electron after applying the preselection cuts. The black curve indi-

cates the maximized cut value that separates a simulation of NUANCE channels (blue) from a simulation of dirt events (red). The left (right) panel of Figure 6.10 represents 2-dimensional plot of RtoWall as a function of reconstructed energy of electron after applying the preselection cuts on signal (dirt), the black curve indicates the RtoWall selection. The plots illustrate that the selection reduces the dirt events dramatically.

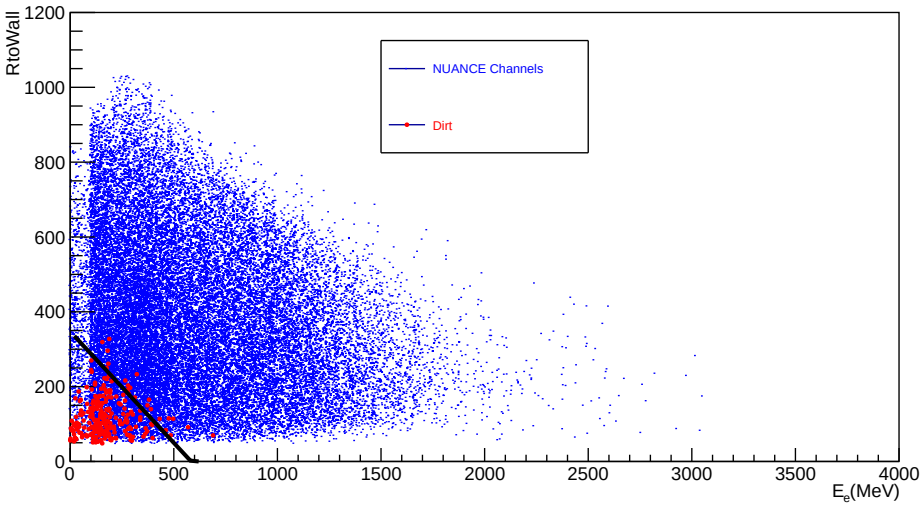

Figure 6.9: The scatter plot of RtoWall as a function of the reconstructed energy of electron after applying the preselection cuts, the black curve indicates the maximized cut value that separates a simulation of NUANCE channels (blue) from a simulation of dirt events (red).

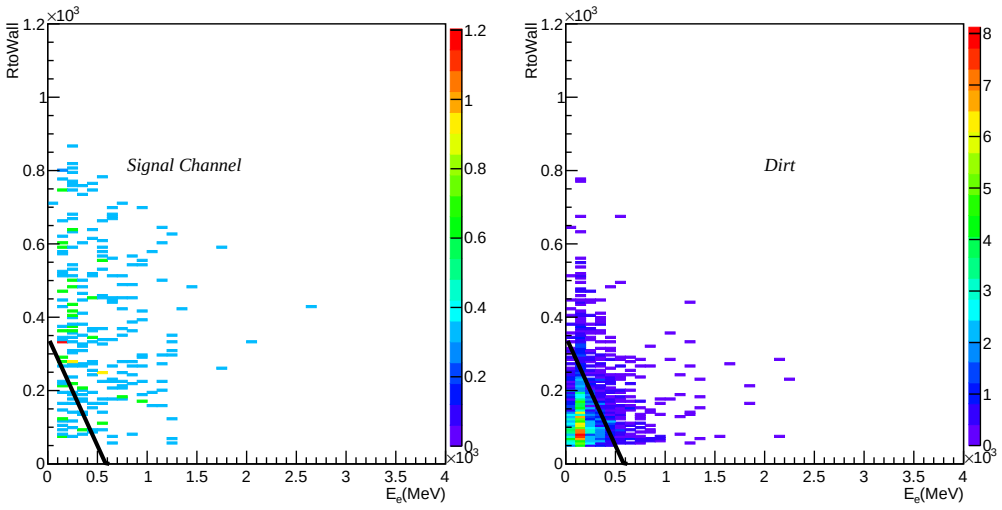

Figure 6.10: The left (right) panel is the scatter plot of RtoWall as a function of the reconstructed energy of electron after applying the preselection cuts for signal (dirt), the black curve indicates the RtoWall cut value.

6.4 Final distribution

Adding all the cuts, listed in previous section, produces the distribution which used to compute the cross section of the electron neutrino elastic scattering. Left (Right) panel of Figure 6.11 shows the electron angle (energy) after applying all selection cuts, the plots indicates almost all simulated signal events appears to be in the direction of $\cos\theta_e > 0.99$, although there are still background contamination in the signal bins (details in section 6.5.2). By considering the cut of $\cos\theta_e > 0.9$ we also keep the bins of only background in the analysis in order to get the extrapolation of background in the signal bins.

The last column of Table 6.2 shows the expected number of signal and background events compare to observed data in the signal bins where $\cos\theta_e > 0.99$. The significance of the excess in signal bins is estimated by the fraction of difference between observed data (n_{data}) and expected number of events from Monte Carlo ($n_{sig} + n_{bkg}$) to the square root of total observed data:

$$\frac{n_{data} - (n_{sig} + n_{bkg})}{\sqrt{n_{data}}} = \frac{107.0 - (30.68 + 47.09 + 3.82)}{\sqrt{107.0}} \approx 2.45\sigma. \qquad (6.1)$$

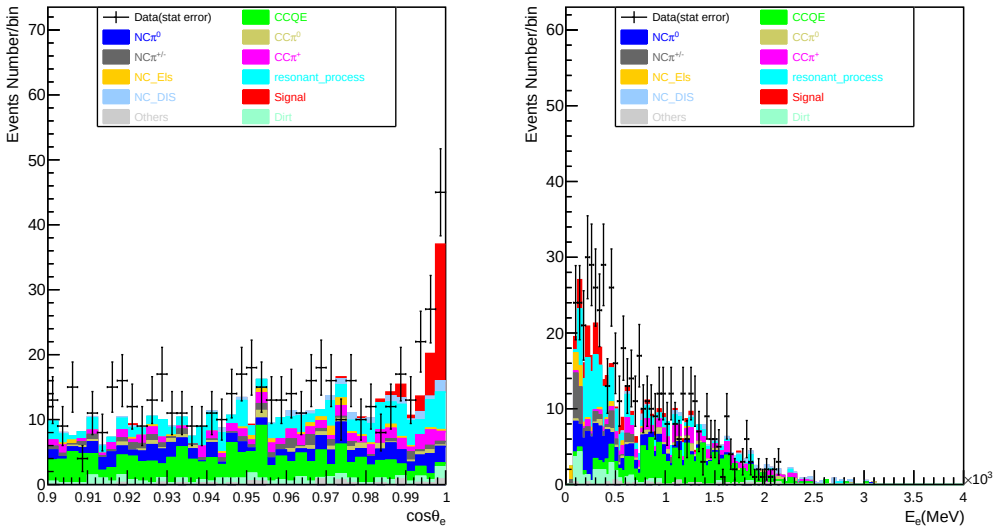

Figure 6.11: The stack electron angle (energy) distribution on the left (right) for various channels in MiniBooNE along with data with its statistical error after applying all cuts.

6.5 Sample Contamination

After defining all the selection cuts, this section presents the sample contamination after consecutive selection requirements. The composition of different interaction types after applying the cuts one-by-one sequentially demonstrates in Table 6.3 (Table 6.4) where $\cos\theta_e > 0.9$ ($\cos\theta_e > 0.99$).

The percentage of the composition sample for individual cut ($C^{cut}_{interaction-type}$) in the tables is defined as the number of events of specific interaction type ($n^{cut}_{interaction-type}$) which passing the cut divided by the number of events for all interaction type (n^{cut}_{total}) passing the cut,

$$C^{cut}_{interaction-type} = \frac{n^{cut}_{interaction-type}}{n^{cut}_{total}} \tag{6.2}$$

consequently each column of the tables presents the total 100%.

6.5.1 Composition of Samples after applying the cuts one-by-one ($\cos\theta_e > 0.9$)

Figure 6.12 shows the number of events of the various interaction types after applying the cuts one-by-one subsequently which corresponding to the percentages present in Table 6.3.

Figure 6.12 shows how adding the individual cut affects the number of events of the specific interaction type. The last column of the table shows the contaminations after applying all selection requirements in the analysis. The purity of electron neutrino elastic scattering (signal) is low, with only 8%, and the most dominated background events in the analysis are CCQE, resonant process with more than 2π and $NC\pi^0$ respectively.

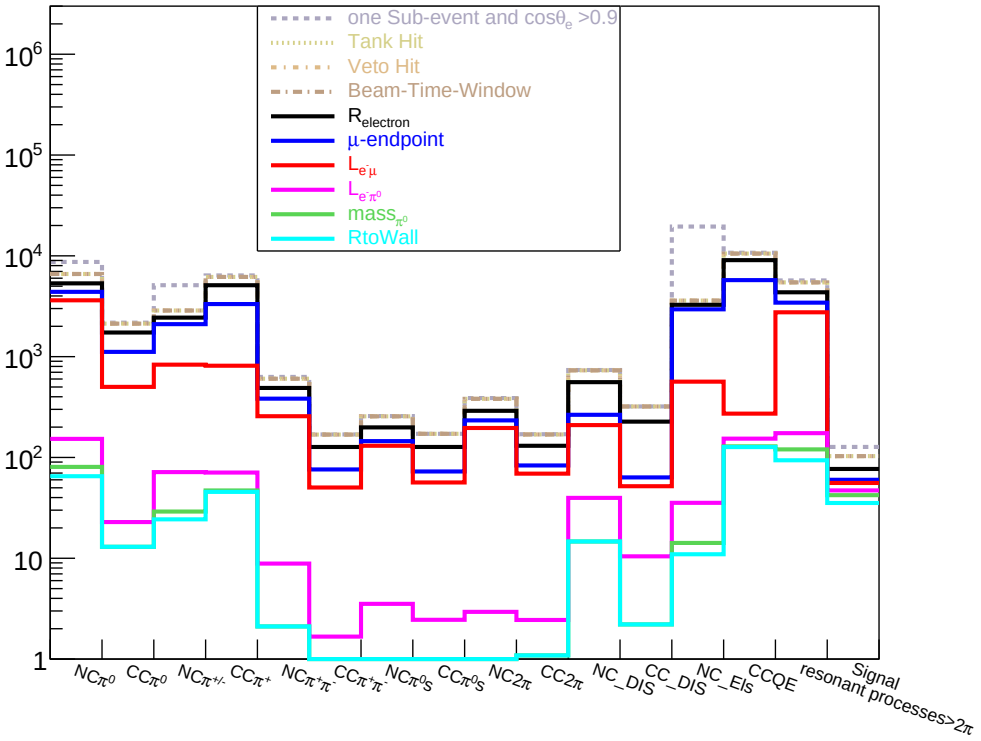

Figure 6.12: Number of events of various interaction types after applying the cuts one-by-one sequentially where $\cos\theta_e > 0.9$.

channel	ones+Direction	Thit	Vhit	beam-window	$R_{electron}$	μ endpoint	$\log(L_e/L_\mu)$	$\log(L_e/L_\pi)$	π^0 Mass	RtoWall
NCπ_0	14.19%	16.41%	16.41%	16.41%	15.91%	17.98%	34.7%	19.09%	16.22%	14.93%
CCπ_0	3.54%	5.28%	5.28%	5.28%	5.18%	4.56%	4.8%	2.86%	2.61%	2.98%
NC$\pi^{\pm}$	8.34%	7.13%	7.13%	7.13%	7.27%	8.6%	7.98%	8.94%	5.85%	5.58%
CCπ^+	10.43%	15.34%	15.34%	15.34%	15.25%	13.6%	7.79%	8.85%	9.47%	10.44%
NCπ^+ π^-	1.03%	1.5%	1.5%	1.5%	1.46%	1.57%	2.46%	1.11%	0.42%	0.48%
CCπ^+ π^-	0.28%	0.42%	0.42%	0.42%	0.38%	0.31%	0.48%	0.21%	0.0%	0.0%
NCπ_0's	0.42%	0.64%	0.64%	0.64%	0.59%	0.59%	1.25%	0.44%	0.12%	0.07%
CCπ_0's	0.28%	0.43%	0.43%	0.43%	0.38%	0.3%	0.54%	0.31%	0.11%	0.13%
NC>2π	0.63%	0.95%	0.95%	0.95%	0.87%	0.95%	1.88%	0.37%	0.11%	0.12%
CC >2π	0.28%	0.42%	0.42%	0.42%	0.39%	0.34%	0.66%	0.31%	0.22%	0.25%
NC-DIS	1.2%	1.82%	1.82%	1.82%	1.67%	1.08%	2.01%	4.96%	2.95%	3.36%
CC-DIS	0.52%	0.8%	0.8%	0.8%	0.68%	0.26%	0.5%	1.31%	0.44%	0.51%
NC-Els	31.84%	8.94%	8.94%	8.94%	9.75%	12.06%	5.41%	4.43%	2.85%	2.51%
CCQE	17.51%	26.15%	26.15%	26.15%	27.04%	23.5%	2.61%	19.19%	25.92%	29.05%
resonant processes >2π	9.3%	13.54%	13.54%	13.54%	12.97%	14.05%	26.39%	21.75%	24.19%	21.49%
Signal	0.21%	0.26%	0.26%	0.26%	0.23%	0.25%	0.54%	5.88%	8.5%	8.1%

Table 6.3: Sample Contamination of all NUANCE channels after applying the cuts one-by-one subsequently

6.5.2 Composition of Samples in Signal Bins after Applying The Cuts One-by-one ($\cos\theta_e > 0.99$)

Figure 6.13 shows the number of events of the various interaction types after applying the cuts one-by-one subsequently which corresponding to the percentages present in Table 6.4. It should be noted that this section presents the contamination of the various interaction types in only signal bins where $\cos\theta_e > 0.99$ in order to study the effects of the cuts in very forward angle where almost all signal events are.

Figure 6.13 shows how adding the individual cut affects the number of events of the specific interaction type in very forward angle. The last column of the table shows the contaminations after applying all selection requirements in the analysis. The purity of electron neutrino elastic scattering (signal) is $\approx 40\%$, and the most dominated background events in the analysis are resonant process with more than 2π, $NC\pi^0$ and CCQE respectively.

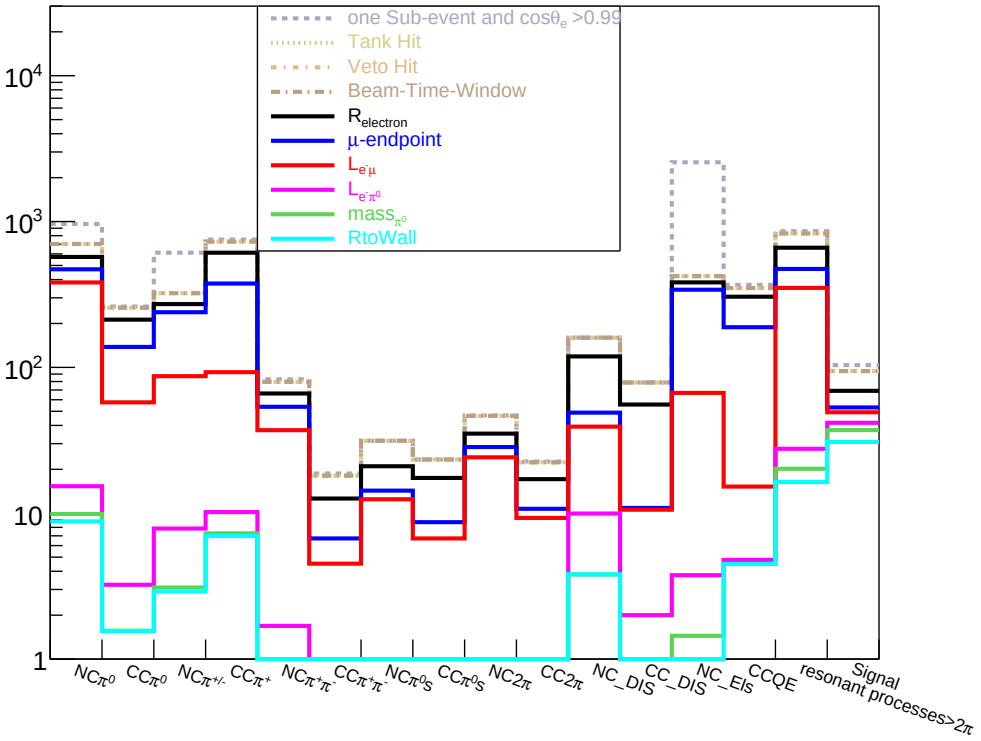

Figure 6.13: Number of events of various interaction types after applying the cuts one-by-one sequentially in signal bins where $\cos\theta_e > 0.99$.

channel	ones	Thit	Vhit	beam-window	$R_{electron}$	μ endpoint	$\log(L_e/L_\mu)$	$\log(L_e/L_\pi)$	π^0 Mass	RtoWall
NCπ_0	13.88%	16.85%	16.85%	16.85%	16.67%	19.12%	30.69%	11.84%	10.95%	11.28%
% CCπ_0	3.77%	6.16%	6.16%	6.16%	6.2%	5.61%	4.62%	2.5%	1.73%	2.0%
NC$\pi^{\pm}$	8.82%	7.75%	7.75%	7.75%	7.92%	9.7%	6.98%	6.07%	3.43%	3.73%
CCπ^+	10.86%	17.49%	17.49%	17.49%	17.83%	15.27%	7.44%	7.87%	8.07%	8.96%
NCπ^+ π^-	1.2%	1.91%	1.91%	1.91%	1.93%	2.18%	2.98%	1.3%	0.67%	0.77%
CCπ^+ π^-	0.27%	0.43%	0.43%	0.43%	0.37%	0.27%	0.36%	0.0%	0.0%	0.0%
NCπ_0's	0.45%	0.75%	0.75%	0.75%	0.61%	0.58%	1.0%	0.62%	0.33%	0.39%
CCπ_0's	0.34%	0.56%	0.56%	0.56%	0.51%	0.35%	0.54%	0.19%	0.0%	0.0%
NC>2π	0.68%	1.12%	1.12%	1.12%	1.02%	1.16%	1.94%	0.19%	0.0%	0.0%
CC >2π	0.33%	0.54%	0.54%	0.54%	0.5%	0.44%	0.75%	0.0%	0.0%	0.0%
NC-DIS	2.31%	3.84%	3.84%	3.84%	3.47%	1.99%	3.15%	7.69%	4.22%	4.89%
CC-DIS	1.14%	1.89%	1.89%	1.89%	1.62%	0.44%	0.85%	1.55%	0.51%	0.59%
NC-Els	36.78%	10.14%	10.14%	10.14%	11.16%	13.85%	5.37%	2.9%	1.6%	1.08%
CCQE	5.31%	8.41%	8.41%	8.41%	8.9%	7.66%	1.22%	3.7%	4.97%	5.76%
resonant >2π	12.39%	19.9%	19.9%	19.9%	19.29%	19.23%	28.16%	21.38%	22.36%	21.0%
Signal	1.5%	2.27%	2.27%	2.27%	2.01%	2.16%	3.95%	32.22%	41.17%	39.57%

Table 6.4: Sample Contamination of all NUANCE channels after applying the cuts one-by-one subsequently in signal bins where $\cos\theta_e > 0.99$

6.6 Summary

After applying the selection cuts on the data with twice more POT than the previous ν-mode data still the purity of the signal sample is low. In order to study the distribution of reconstructed signal events, it is necessary to obtain more pure sample. This goal achieved by fitting data distributions to Monte Carlo predicted signal and background to extract the fraction of the signal events in data. Moreover we need to have the exact measurement on statistical and systematic uncertainties associated with the selected data. In the following chapter we measure the errors, and present the fit on selected data to compute the signal cross section.

7 Cross section Measurement

After defining our signal by applying the selection cuts, described in previous chapter, this chapter presents the electron neutrino elastic scattering cross section measurement in MiniBooNE.

The analysis of this channel is performed using statistical fits to extract the number of signal events in the data sample. Fitting is necessary because of the relatively low purity of the final sample after applying all selection cuts. The detail of fitting procedure is described in the following section, followed by a list all the possible systematic uncertainties and the procedure employed to add them to the analysis, at the end the cross section measurement method and its validation discuss.

7.1 Fit Procedure

Table 6.3 showed that only $\approx 8\%$ of the events in the final sample selection are due to electron neutrino elastic scattering. It was also mentioned earlier that in order to overcome the limitation on the purity of the signal events we employ statistical fit of the data to MC predicted signal and background distribution. As illustrated in Figure 6.1, the signal events scattered in very forward direction with low energy, and the final distribution (Figure 6.11) showed the background events are nicely constrained by $\cos\theta_e$ distribution, but the energy distribution of the background do not follow any specific pattern. As a consequent the electron neutrino elastic scattering events can be distinguished from the background events in the angular distribution, although the signal bins ($\cos\theta_e > 0.99$) in the angular plot have contamination of the background events which come from wide range of energy from $50\ MeV$ to $4\ GeV$. The combined fit of the two distributions allows to increase signal purity by spreading the background events with their wide range of energy.

Note that the 2-dimensional fit requires high statistics for the fitting algorithm to converge. Since the selected sample has low statistics, the reconstructed energy is divided into only two bins of low ($< 800MeV$) and high ($> 800MeV$) elec-

tron energy. Moreover since the sample has lower statistics in high energy region the angular distribution in that region is divided into ten bins, while the low energy region with high enough statistics grouped into twenty bins. Figure 7.1 shows the so-called 2D distribution of $\cos\theta_e$ with two bins of reconstructed electron energy for the signal and all possible background events. Table 7.1 (7.2) shows the sample contamination after applying the cuts subsequently in low (high) electron energy. Since the signal events appear mostly in low energy the purity of the signal increased to $\approx 13\%$ in that region.

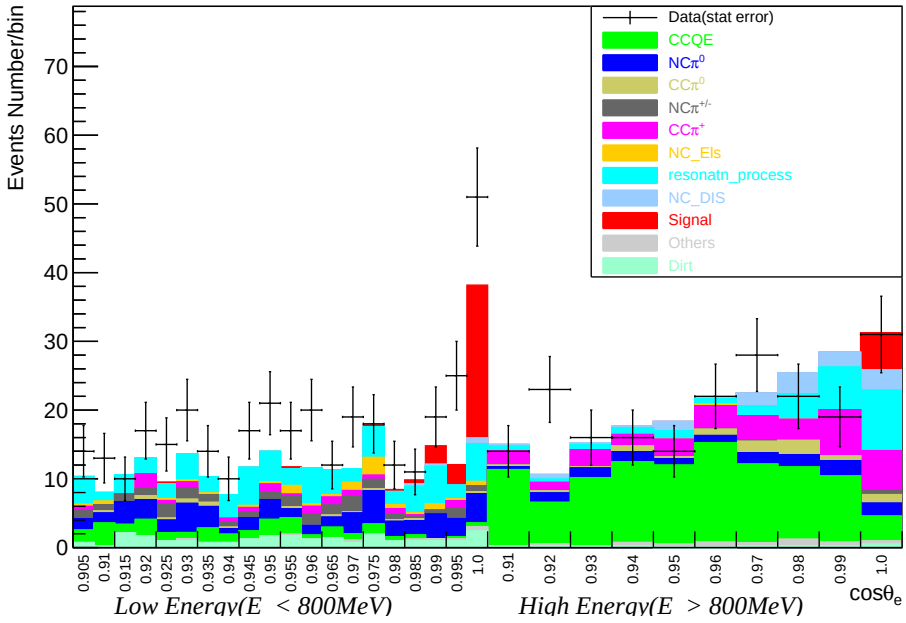

Figure 7.1: The 2-dimensional distribution of $\cos\theta_e$ and E_e in final selection sample.

channel	ones	Thit	Vhit	beam-window	$R_{electron}$	μ endpoint	$\log(L_e/L_\mu)$	$\log(L_e/L_\pi)$	π^0 Mass	RtoWall
NCπ_0	17.01 %	22.37%	22.37%	22.37%	21.95%	23.00%	38.82 %	24.83%	22.68%	21.96%
CCπ_0	2.34 %	3.94%	3.94 %	3.94%	3.81 %	3.51%	3.30%	1.54 %	1.53 %	1.93 %
NC$\pi^{\pm}$	10.33%	10.08%	10.08%	10.08%	10.38%	11.30%	9.11%	14.52%	9.66 %	10.15%
CCπ^+	8.53 %	14.21%	14.21%	14.21%	13.85 %	12.32	6.37 %	5.63%	4.99%	5.65%
NCπ^+ π^-	1.11%	1.86%	1.86%	1.86%	1.84%	1.87%	2.49%	1.34%	0.39 %	0.49%
CCπ^+ π^-	0.15%	0.26 %	0.26%	0.26%	0.22%	0.22%	0.32 %	0.06%	0.0%	0.0 %
NCπ_0's	0.3 %	0.52 %	0.52 %	0.52%	0.49%	0.50%	0.94 %	0.29%	0.20 %	0.13%
CCπ_0's	0.1%	0.18%	0.18 %	0.18%	0.16 %	0.15 %	0.24%	0.06%	0.0 %	0.0%
NC>2π	0.55 %	0.94%	0.94%	0.94 %	0.88 %	0.97	1.66%	0.32%	0.11%	0.13%
CC >2π	0.13 %	0.23%	0.23 %	0.23 %	0.22%	0.21 %	0.36%	0.05 %	0.09 %	0.11%
NC-DIS	0.33 %	0.55 %	0.55%	0.55%	0.53 %	0.54%	0.79 %	0.95 %	0.51%	0.64%
CC-DIS	0.04 %	0.07%	0.07%	0.07 %	0.07%	0.07%	0.10 %	0.08 %	0.12%	0.16%
NC-Els	39.91 %	12.85%	12.85%	12.85%	14.14%	16.00%	6.24 %	7.28%	4.76 %	4.61%
CCQE	9.49%	15.92 %	15.92%	15.92%	15.93%	13.02%	1.41 %	8.0%	9.87%	11.54%
resonant >2π	9.46 %	15.72%	15.72%	15.72%	15.72%	16.04 %	27.31%	26.43 %	32.51%	29.61%
Signal	0.22 %	0.3%	0.3%	0.3 %	0.27%	029%	0.55%	8.62 %	12.58 %	12.89%

Table 7.1: The sample purity after applying the cuts subsequently in low electron energy (<800MeV).

channel	ones	Thit	Vhit	beam-window	$R_{electron}$	μ endpoint	$\log(L_e/L_\mu)$	$\log(L_e/L_\pi)$	π^0 Mass	RtoWall
NCπ_0	3.07 %	3.07 %	3.07 %	3.07 %	2.75 %	2.88 %	10.72 %	10.49 %	6.95 %	6.95 %
CCπ_0	8.27 %	8.27 %	8.27 %	8.27 %	8.15 %	7.73 %	13.56 %	4.83 %	4.16 %	4.16 %
NC$\pi^{\pm}$	0.51 %	0.51 %	0.51 %	0.51 %	0.51 %	0.47 %	1.38 %	0.57 %	0.38 %	0.38 %
CCπ^+	17.87 %	17.87 %	17.87 %	17.87 %	18.28 %	17.46 %	16.08 %	13.67 %	15.87 %	15.87 %
NCπ^+ π^-	0.7 %	0.7 %	0.7 %	0.7 %	0.64 %	0.66 %	2.27 %	0.76 %	0.47 %	0.47 %
CCπ^+ π^-	0.77 %	0.77 %	0.77 %	0.77 %	0.73 %	0.58 %	1.45 %	0.43 %	0.0 %	0.0 %
NCπ_0's	0.89 %	0.89 %	0.89 %	0.89 %	0.81 %	0.88 %	3.05 %	0.66 %	0.0 %	0.0 %
CCπ_0's	0.98 %	0.98 %	0.98 %	0.98 %	0.86 %	0.75 %	2.29 %	0.68 %	0.28 %	0.28 %
NC>2π	0.96 %	0.96 %	0.96 %	0.96 %	0.82 %	0.9 %	3.18 %	0.44 %	0.11 %	0.11 %
CC >2π	0.85 %	0.85 %	0.85 %	0.85 %	0.77 %	0.74 %	2.42 %	0.68 %	0.41 %	0.41 %
NC-DIS	4.64 %	4.64 %	4.64 %	4.64 %	4.15 %	2.74 %	9.07 %	10.97 %	6.45 %	6.45 %
CC-DIS	2.41 %	2.41 %	2.41 %	2.41 %	2.0 %	0.84 %	2.83 %	3.15 %	0.9 %	0.9 %
NC-Els	0.19 %	0.19 %	0.19 %	0.19 %	0.19 %	0.2 %	0.62 %	0.17 %	0.13 %	0.13 %
CCQE	49.03 %	49.03 %	49.03 %	49.03 %	51.22 %	55.04 %	9.6 %	35.96 %	48.94 %	48.94 %
resonant >2π	8.68 %	8.68 %	8.68 %	8.68 %	7.98 %	8.03 %	21.03 %	14.76 %	12.26 %	12.26 %
Signal	0.16 %	0.16 %	0.16 %	0.16 %	0.14 %	0.12 %	0.45 %	1.79 %	2.67 %	2.67 %

Table 7.2: The sample purity after applying the cuts subsequently in high electron energy (> 800MeV).

7.2 Measurement Uncertainties

Before measuring the final cross section we need to assess the systematic and statistical uncertainties associated with the measurement. The individual normalized error contributions to the total electron neutrino elastic scattering cross section is listed in Table 7.3. We begin by presenting the definition of each individual uncertainty in MiniBooNE, and show the procedure of computing them, later (section 7.4).

The systematic uncertainties can be classified into one of the following three types:

1. **Flux uncertainty:** the uncertainty in the flux is due to the combination of the following uncertainties :
   - *POT error:* this error is due to the uncertainty in number of POT delivered to the MiniBooNE target by the Fermilab Booster.
   - *Beam error:* this error associated with horn uncertainties and uncertainties in the target that affect the neutrino flux. The uncertainty involves parameters like: skin depth, horn current, nuclear inelastic cross section, nuclear quasi-elastic cross section, pion inelastic cross section, pion quasi-elastic cross section, and pion total cross section.
   - π^+, π^-, K^0, K^-, *and* K^+ *production in the target:* These five uncertainties are due to the uncertainties in the meson production from the simulation of inelastic interactions of proton in the Beryllium target with the potential to produce these mesons. The number of particles produced in an inelastic scattering follows the Poisson distribution with dependency on double differential cross section for different meson productions, Sanford-Wang parametrization describes the production of $\pi^{\pm}$ and K^0, on the other hand production of K^+ (K^-) describes by Feynman scaling (MARS15 hadron MC package) for more details see Ref. [69]. The uncertainties associated with the parameterization of the double differential cross section involve in these last five uncertainties.
2. **Cross section uncertainty:** the uncertainty in the cross section is due to the modeling:

- *Hadronic model error:* the uncertainties in the hadron production model in the MiniBooNE detector appears to this error.
- π^0 *yield error:* the uncertainty in the π^0 production in the detector.
- *Cross section error:* the uncertainties in the cross section parameters shown on Table 5.2. For the electron neutrino elastic scattering cross section measurement, these parameters are allowed to vary only for the background events.
- *Dirt error:* the uncertainty in the dirt background measurement.

3. **Detector uncertainty:** the uncertainties in the detector response is due to following sources:
   - *Discriminator threshold:* is PMT response variation, the discriminator threshold is varied from its central value of $0.1\ PE$ (photoelectric effect) to $0.2\ PE$. The altered threshold affects hit timing and results in the loss of of some low-charge hits.
   - *Charge-time correlation:* is also PMT response variation, the charge- time (QT) correlation variation concerns the shape of the PMT hit charge distribution as a function of hit time. The error due to the uncertainty in the model of charge-time simulation of the PMTs.
   - *Optical Model (OM):* this error is due to the uncertainty in the modeling of the optical properties of the detector target medium. OM excursions consist of the variation of 35 correlated parameters:
     - extinction length (5)
     - Raleigh/Raman scattering (3)
     - refractive index (3)
     - PMT angular efficiency (2)
     - scintillation yield from each fluor (4)
     - fluorescence yield from each fluor (4)
     - UV fluorescence yield from each fluor (4)
     - time constant of from each fluor (4)
     - Cherenkov scale factor (1)
     - reflection (2)

- Birk's law coefficients (2)
- old/new PMT relative efficiency (1)

Because of computing constraints, the MC sample generated for each excursion was limited to having only data-sized statistics. 66 (130) throws were generated for neutrino (antineutrino) mode. Each throws was ran with data statistics collected. By adding the new neutrino mode data (MicroBooNE-era) we have more data (twice more POT), as a consequence the statistical error predicted by OM is now higher than what it is in reality with new data.

By the time of finishing this analysis the MC throws on OM with new data size are not available. Therefore we introduce a method in which the old statistical error subtracted from OM and new statistical error from data added to it. The study on the effects of this method discusses by comparing the results of the fit where the new statistical error from data added instead of the old errors (details in section 7.5).

Consequentially we have a total of 15 systematic uncertainties, plus statistical error to consider in computing the cross section.

7.3 multisim and unisim

Systematic uncertainties for MiniBooNE are calculated with two different methods: 1) unisim, and 2) multisim [70]. unisim are generally used when the effect on the final physics parameters are changed and the response functions are known, while multisim are generally used when the covariance matrix of the input parameters is known.

1. *unisim:* For this method, a new set of MC events "MC^{unisim}" for individual systematic is created by changing a particular parameter to a $1-\sigma$ excursion value, and an error matrix may be constructed by combining with the MC of the best estimation of the parameter which called central value MC, "MC^{cv}",

$$M_{ij}^{unisim} = (N_i^{unisim} - N_i^{cv})(N_j^{unisim} - N_j^{cv}) \tag{7.1}$$

Here, N_i^{unisim} and N_i^{cv} are the number of events in the i^{th} bin of a given his-

Sources of Error	Total Normalized Error %	
POT	2.8	Flux Uncertainty = 8.1%
Beam-Unisim	2.8	
K^-Production	2.5	
K^+Production	3.9	
K^0Production	3.7	
π^+Production	2.6	
π^-Production	2.8	
Hadronic production	2.7	Cross Section Uncertainty = 11.13%
π^0 Yield	3.5	
cross section (backgrounds)	10.3	
Dirt	2.7	
CCQE -CCπ	2.6	
Optical Model	7.2	Detector Uncertainty = 8.3%
Discriminator threshold	1.4	
Charge-time correlation	3.9	
statistical error from data	5.1	

Table 7.3: Individual normalized error contributions to the total $e^-\nu$ elastic scattering cross section

togram from the unisim MC (MC^{unisim}) and central value MC (MC^{cv}), respectively. All unisim parameters are assumed independent, so the total error matrix considering all unisim parameters is the simple sum of all unisim error matrices.

The uncertainties due to the discriminator threshold, and charge-time correlation are calculated by using unisim method. Figure 7.2(a)(7.3(a)) shows how $1-\sigma$ excursion value of discriminator threshold (charge-time correlation) in gray compares to MC^{cv} in black. Figure 7.2(b), and 7.3(b) illustrate the covariance matrix (equation 7.1) for the corresponding detector unisim errors.

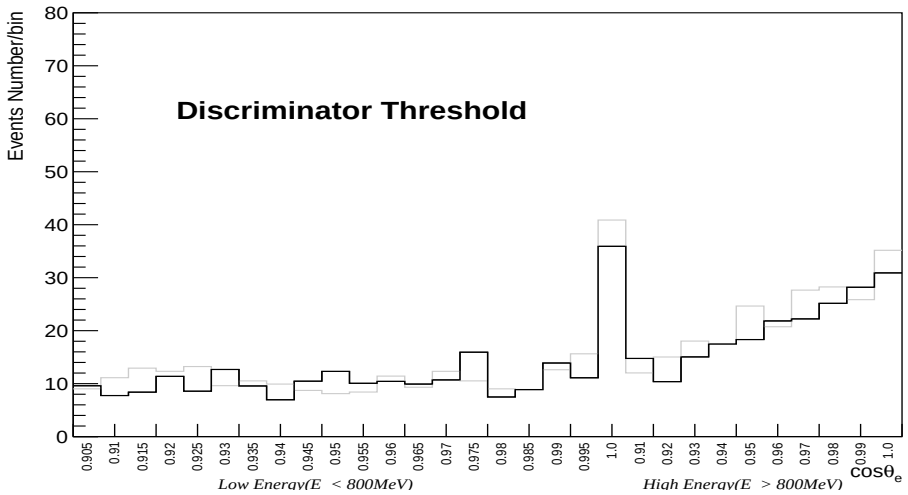

(a)

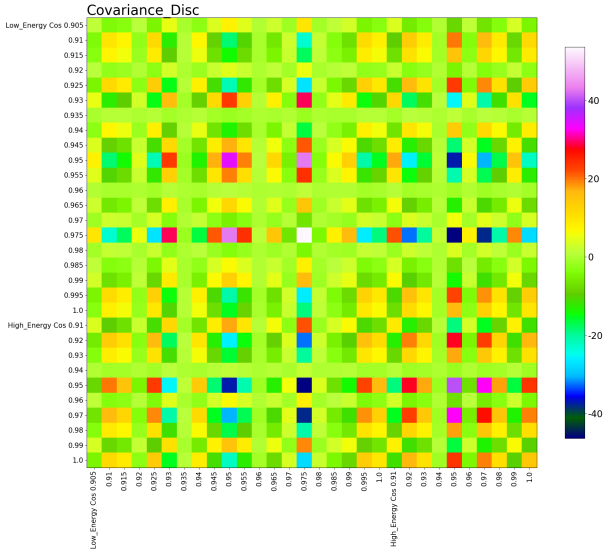

(b)

Figure 7.2: (a) $1-\sigma$ excursion value of discriminator threshold (gray) in the angular distribution low and high energy compare to cv MC (black). (b) The covariance matrix of discriminator threshold.

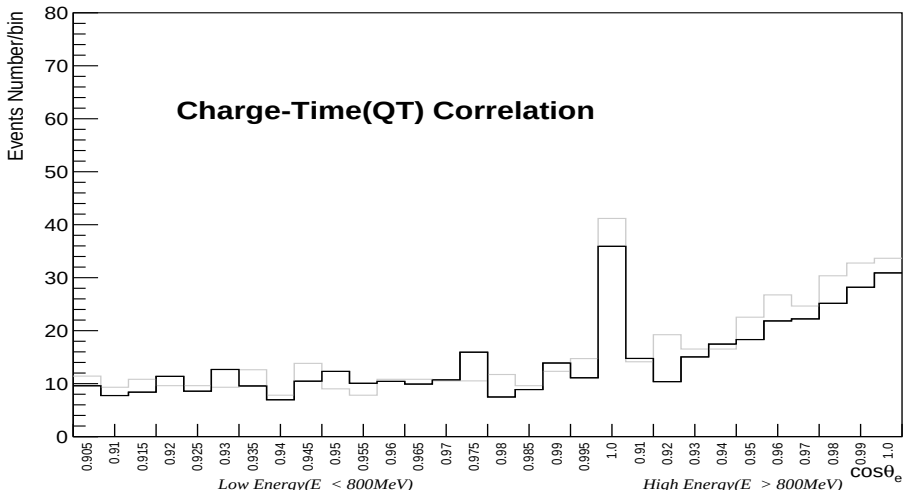

(a)

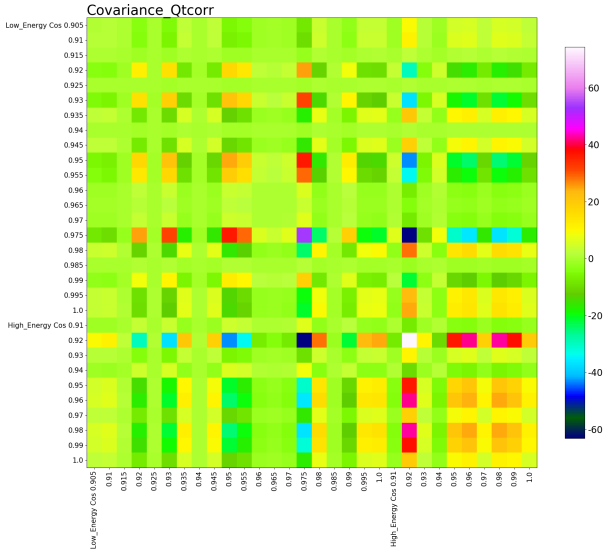

(b)

Figure 7.3: (a) $1-\sigma$ excursion value of charge-time correlation (gray) in the angular distribution low and high energy compare to cv MC (black). (b) The covariance matrix of charge-time correlation.

2. *Multisims:* Some systematic Uncertainties are highly correlated, the unisim method cannot estimate the systematic error correctly if there are correlations between different parameters. The multisim method correctly handles this effect. First, we classify parameters into G groups. The g^{th} group consists of u parameters. These parameters are dependent upon each other, but independent from the parameters in other groups. So, in the end, we can form G independent multisim error matrices and the final total error matrix will be the simple sum (it should be noted that the matrix is already quadratic) of all matrices. For our case, all different sources of error in Table 7.3 (except last 3) are based on multisim (G=13).

   Several throws are run to see how the reconstructed distribution changes by choosing different parameter values based off the input covariance matrix. This is possible because the analytic and simulated relationship between the input parameters and the true energy of the event is known. The covariance matrix from the multisim method was calculated by following equation:

$$M_{ij}^{multisim} = \frac{1}{n_{throws}} \sum_{k=1}^{n_{throws}} (N_i^k - N_i^{cv})(N_j^k - N_j^{cv}) \tag{7.2}$$

   where N_i^k is the number of events in i^{th} bin of k^{th} histogram from the k^{th} MC run in the set of multisim.

   For the uncertainties due to the neutrino flux prediction and the neutrino cross section, the multisim can be constructed by an event-by-event re-weighting. Varying the parameters do not change the nature of the events, but just likelihood of their occurring which can be controlled by weight the events. In our case, we ran 1000 MC throws for the flux and cross section uncertainties, more details on systematic uncertainties can be found in Ref. [6]. Figure 7.4 shows the multisim MC throws (gray) compare to cv MC (black) in the 2-dimensional distribution for the first twelve sources of multisim errors in Table 7.3, the first 20 (last 10) bins represent the angle of $\cos\theta_e > 0.9$ in low (high) energy region, the red square in the plots indicate the sources of the flux uncertainties. It important to note that the cross section modeling errors just applied on the

background in the analysis since we are computing the signal cross section. Moreover Figure 7.5 shows the cross section modeling uncertainty on each individual background channels.

Figure 7.6 and 7.7 illustrate the covariance matrices (using equation 7.2) as the result of the total sources of flux uncertainties (with the total normalized errors of $\%8.1$) and cross section uncertainties (with the total normalized errors of $\%11.13$) respectively.

The covariance matrices demonstrate that the last bins of high energy region with the angle $\cos\theta_e > 0.97$ have the highest ambiguity. This big uncertainty in high energy region of the Cross Section Modeling (CSM) is due to big uncertainties on the modeling of CCQE and resonant process with more than 2π channels. The covariance matrices of the cross section modeling of these two channels are shown in Figure 7.8. Table 7.4 shows the normalized cross section modeling uncertainty on each background channel in low and high energy region (first column), and as the low and high energy are separated in the second and third columns on each background channel.

Background channel	CSM Error (low and high energy) %	(Low energy) %	(High energy) %
Resonant process ($> 2\pi$)	3.1	5.2	5.5
CCQE	8.1	3.9	12.4
NC-DIS	1.0	0.6	2.8
NC-Els	1.0	1.9	0.1
CCπ^+	2.2	1.0	4.1
CCπ^0	0.6	0.4	1.1
NCπ^0	3.2	3.6	3.3
NC$\pi^{+/-}$	2.8	5.1	0.3
Total CSM Uncertainty	10.3	9.2	14.9

Table 7.4: Normalized error (on individual background channels) contributions to the total Cross Section Modeling (CSM) uncertainty in $e^{-}\nu$ elastic scattering cross section measurement.

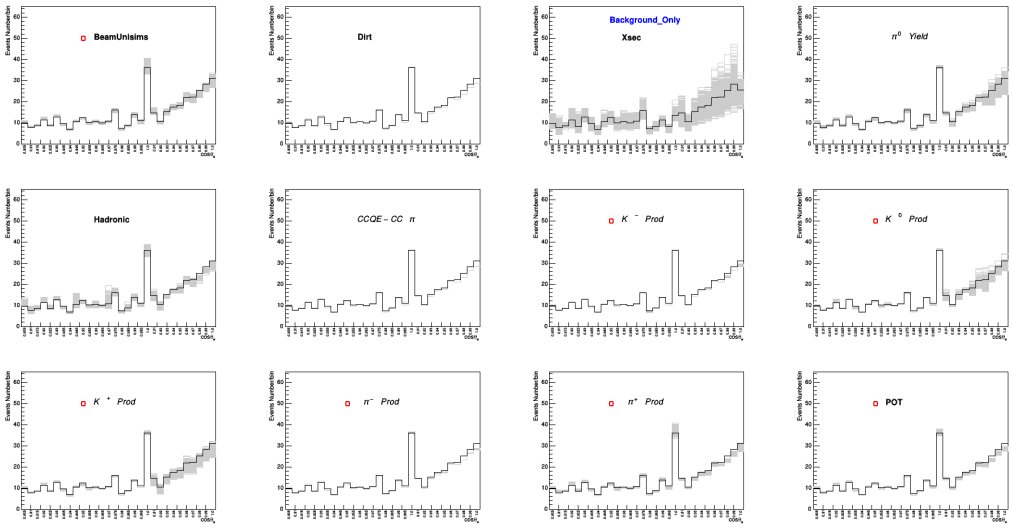

Figure 7.4: MC throws (gray) compare to cv MC (black) in 2-dimensional distribution for various sources of multisim errors. The first 20 (last 10) bins represent the angle of $\cos\theta_e > 0.9$ in low (high) energy, the red square in the plots points out the sources of the flux uncertainties. It important to note that the cross section modeling errors just applied on the background channels in the analysis as we are computing the signal cross section.

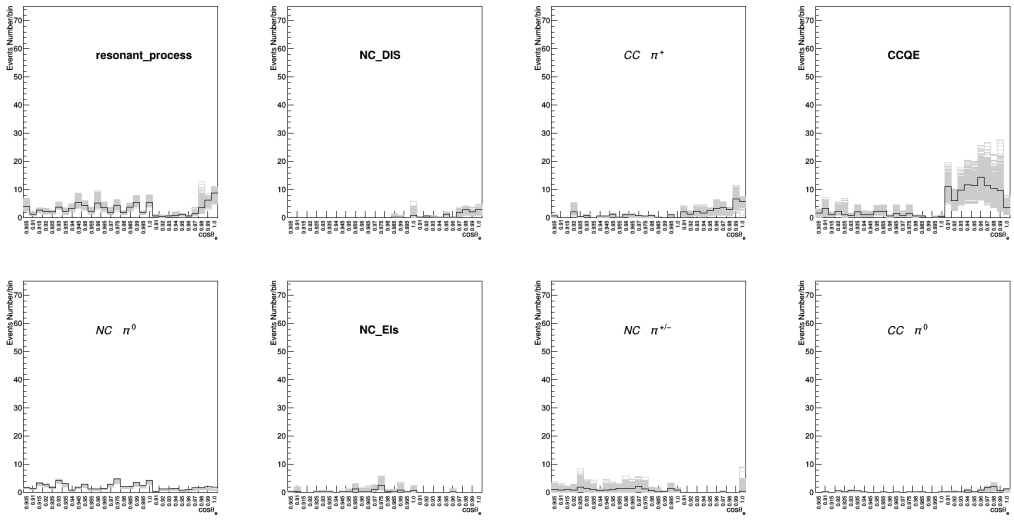

Figure 7.5: MC throws (gray) compare to cv MC (black) of cross section modeling in 2-dimensional distribution for individual background channels (the notations are same with Figure 7.4)

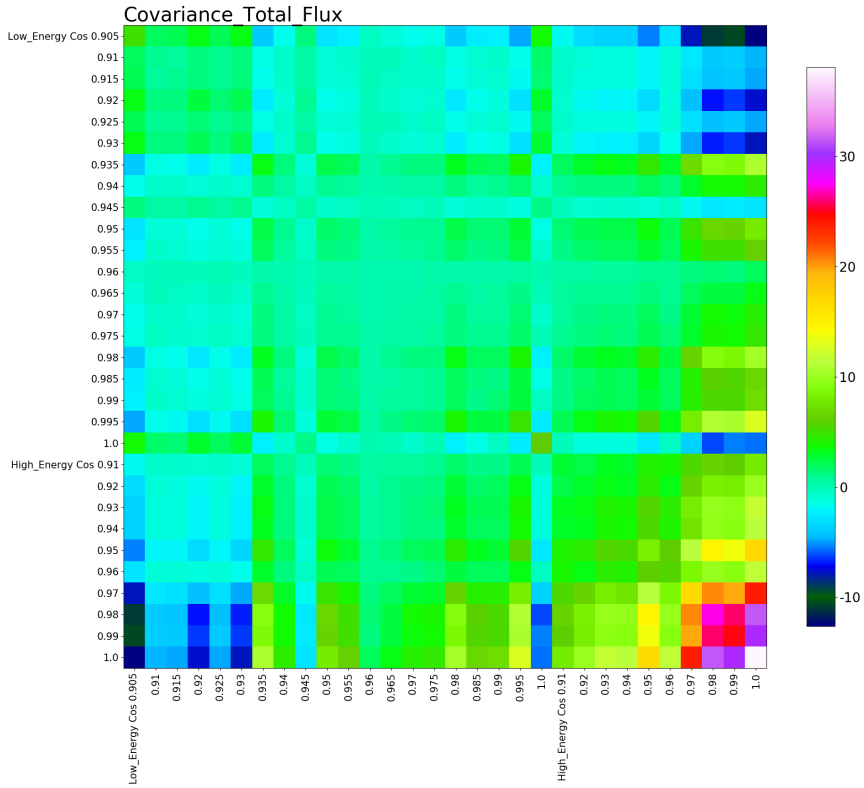

Figure 7.6: Total flux covariance matrix

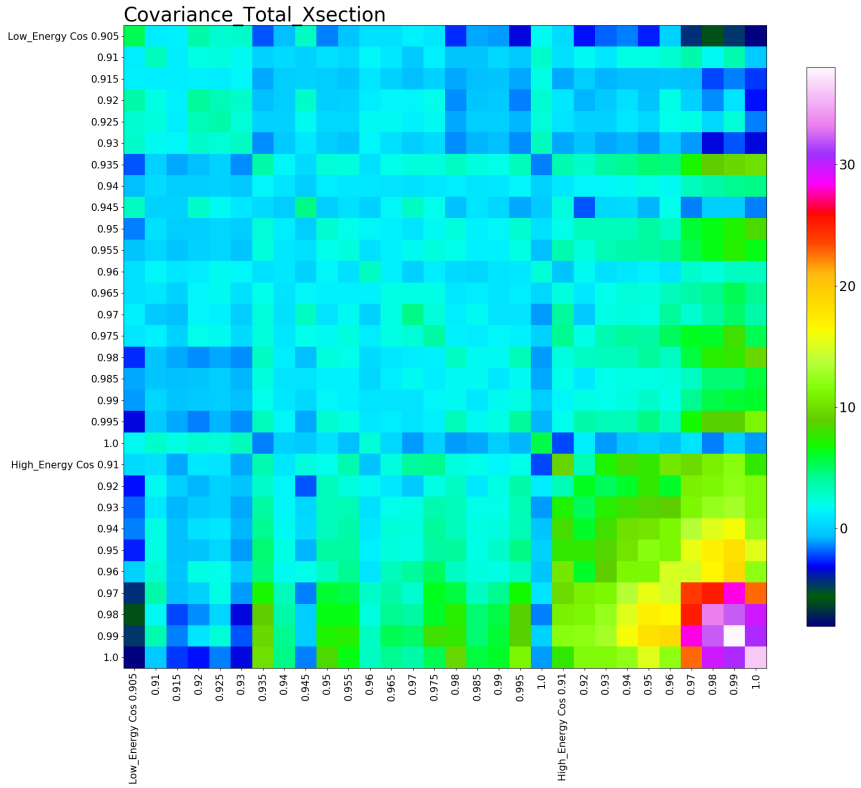

Figure 7.7: Total cross section covariance matrix

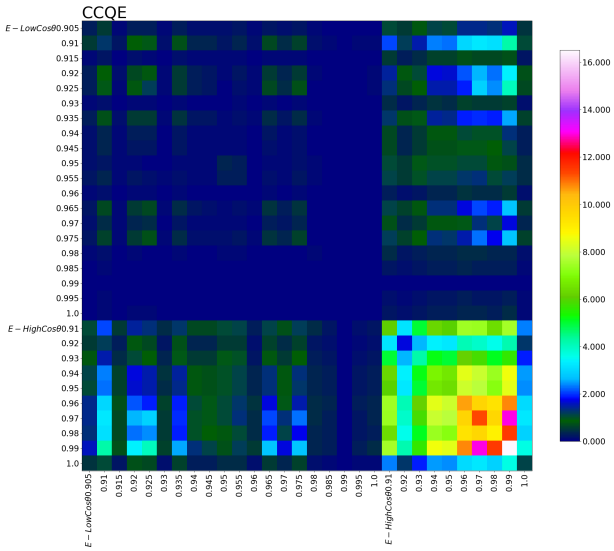

(a)

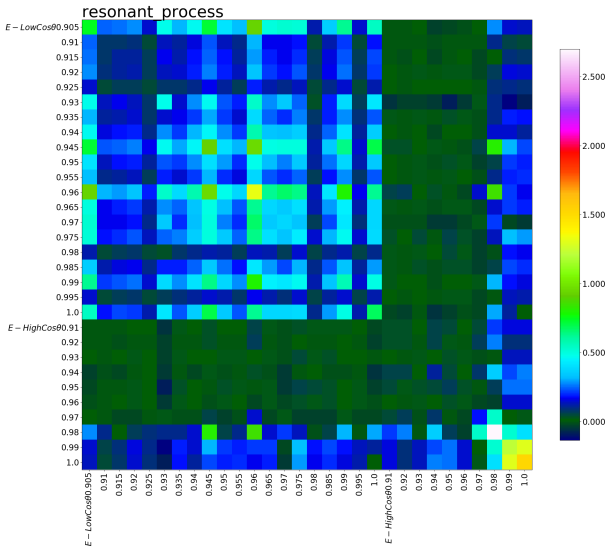

(b)

Figure 7.8: (a) The cross section modeling covariance matrix on CCQE (b) The cross section modeling covariance matrix on resonant process with more than 2π.

On the other hand, for the OM uncertainty, this re-weighting method could not be used due to the effect on the nature of the events (e.g. energy, angle, and time distributions) when the OM parameters are varied. Thus the OM multisim were produced by generating 66 fully reconstructed simulations based on the covariance matrix of the 35 OM parameters, which then passed through the selection cuts.

Figure 7.9(a) shows how 66 OM throws (gray) varies from the central value (black) in 2-dimensional distribution. Figure 7.9(b) illustrate the covariance matrix (using equation 7.2) for the OM uncertainty. Therefore the total uncertainty due to the detector is a simple summation of the OM, Discriminator threshold and Charge-time correlation which result in 8.3% uncertainty.

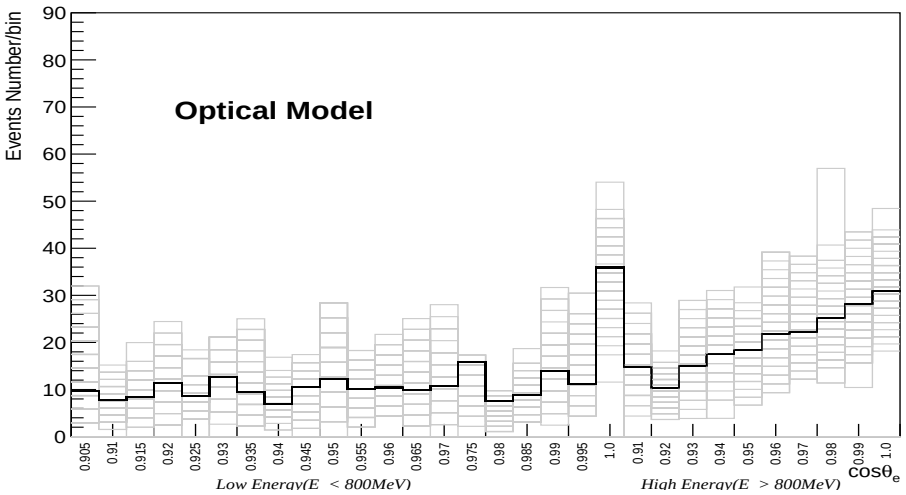

(a)

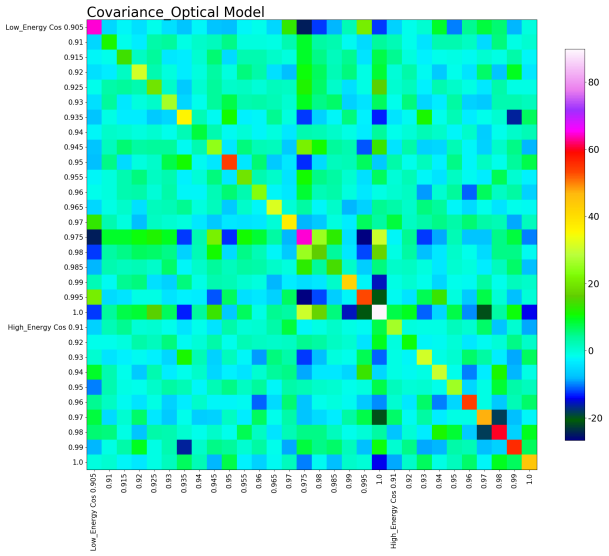

(b)

Figure 7.9: (a) 66 optical model throws (gray) compare to cv MC (black) in 2-dimensional distribution. (b) The covariance matrix of optical model.

7.4 Uncertainty Calculation

Equation 7.1 (7.2) forms an $n \times n$ (n is the number of the bins in the histogram) error matrix for each uncertainty, which computed and illustrated for each individual error in previous section.

The diagonal element of this error matrix, M_{ii}, is called the variance of N_i, $var(N_i)$, and an off-diagonal element, $M_{ij}(i \neq j)$, is called the covariance of N_i and N_j, $cov(N_i, N_j)$. Then the total error for the i^{th} bin, δN_i, is:

$$\delta N_i = \sqrt{M_{ii}} \tag{7.3}$$

if the histogram is combined into only one bin, $N_T = N_1 + \cdots + N_n$, total error for the total number of events, N_T , becomes:

$$\delta N_T = \sqrt{var(N_i + \cdots + N_n)} = \sqrt{\sum_{ij} M_{ij}} \tag{7.4}$$

where we used the sum rule of variance and covariance,

for 2×2 matrix: $var(N_1{+}N_2) = var(N_1){+}var(N_2){+}2cov(N_1, N_2) = \sum_{\substack{0<i<3 \\ 0<j<3}} M_{ij}$ (7.5)

In order to show the size of the error matrix in a single number, the "total normalized error" introduced as

$$\frac{\delta N_T}{N_T} = \frac{\sqrt{\sum_{ij} M_{ij}}}{N_1 + \cdots + N_n} \tag{7.6}$$

The total uncertainties in Table 7.3 computed by using equation (7.6).

7.5 Fit Monte Carlo To Data

The fit to data distributions allows us to estimate the correction in flux averaged cross section of electron neutrino elastic scattering coming from MiniBooNE MC. In this section the results of the fit presents where the complete study discusses on the uncertainties.

The fitting routine uses MINUIT to perform a χ^2 minmization, returning the best estimate of the correction factor on the MC prediction in the observed data.

Here, all background MC are added together. The background prediction, with different shape in low and high energy region, floats with two separated fractions (the background fraction in low (n_{bkg}^{low-E}) and high (n_{bkg}^{high-E}) energy region).

On the other hand the signal prediction, with the same shape in low and high energy region, floats with only one overall fraction in both low and high energy region (n_{sig}). In order to consider the different efficiency of the signal in low and high energy region we have to correct the fraction in high energy region with the fraction of the number of signal events in high energy ($a = 5.41$) to the number of signal events in low energy ($b = 29.78$), $\frac{a}{b} = \frac{5.41}{29.78}$. Note that this fraction adds an additional systematic uncertainties which has to be taken into account. The error propagation of the fraction is considered to be the Poisson error of the fraction where there is no correlation between them in the bins of the signal in high energy region.

As mentioned earlier in order to use the best constraining information from all background prediction in the analysis, the distribution considered to have wider angel range than the only signal bins. We do the fit on 30 bins, 20 bins in low energy plus 10 bins in high energy in the angle of $\cos\theta_e > 0.9$.

The χ^2 function to minimize is

$$\chi^2 = \sum_{i=1}^{\text{all bins(30)}} \sum_{j=1}^{\text{all bins(30)}} (N_i^{data} - N_i^{MC}) \, (M_{total}^{-1})_{ij} \, (N_j^{data} - N_j^{MC}) \qquad (7.7)$$

where N_i^{MC} (N_i^{data}) is the number of events predicted (observed) in the i^{th} bin and M_{total}^{-1} is the inverse of total error matrix resulting from various sources of

uncertainty,

$$M_{total} = M_{flux} + M_{cross-section} + M_{detector} + M_{data-stat} + M_{\frac{a}{b}} \tag{7.8}$$

N_i^{MC} is the sum of the number of signal (N_i^{sig}) and background (N_i^{bkg}) events predicted in the i^{th} bin with their correction factors,

$$N_i^{MC} = n_{sig} \times N_i^{sig} + n_{bkg}^{low-E} \times N_i^{bkg} \quad \text{where} \quad i \leq 20 \text{ (low energy)} \tag{7.9}$$

$$N_i^{MC} = \frac{a}{b}\, n_{sig} \times N_i^{sig} + n_{bkg}^{high-E} \times N_i^{bkg} \quad \text{where} \quad i > 20 \text{ (high energy)} \tag{7.10}$$

This section presents the results of minimizing the χ^2 function (doing the fit). First, the fit with varying only the signal (background) prediction correction factor(s) in the grid presents in order to study the behavior of data with no enhanced in background (signal) model. Then, the results of the signal-background fit with varying the signal and background predictions simultaneously present. Floating the background prediction along with the signal provide an important constraint on the background number of the events in the signal region where $\cos\theta_e > 0.99$. Moreover varying the background in the fit can carry out the excess concluded from the oscillation analysis.

Furthermore a complete study on the response of excluding/including the most effective systematics uncertainties in the fit results presents for both signal (background) only and signal-background fit.

7.5.1 Signal Only and Background Only Fit

In order to study signal model itself and obtain the estimate of the signal fraction with the assumption of the perfect background model, we vary only the signal fraction in the grid of 30 bins, the number of degrees of freedom (d.o.f.) is obtained by (#bins−#free parameters), here 30 (bins) -1 (free parameter)$= 29$ (d.o.f.). Minimizing χ^2 function with one free parameter (n_{sig}), where all system-

atics uncertainties included in the analysis, results in $n_{sig} = 1.62 \pm 0.37$. The study on the response of excluding/including systematics uncertainties in the fit results present in the second box of Table 7.5.

On the other hand in order to study the background model itself and obtain the estimate of the background fractions with the assumption of the perfect signal model, we vary only the background fractions in low and high energy in the grid (28 d.o.f.). Minimizing χ^2 function with two free parameters (n_{bkg}^{low-E} and n_{bkg}^{high-E}), where all systematics uncertainties included in the analysis, results in $n_{bkg}^{low-E} = 1.42 \pm 0.15$ and $n_{bkg}^{high-E} = 0.90 \pm 0.21$. The study on the response of excluding/including systematics uncertainties in the fit results present in last box of Table 7.5.

7.5.2 Signal-Background fit

Signal-background fit performs with varying three fit parameters, n_{sig}, n_{bkg}^{low-E} and n_{bkg}^{high-E} in the grid (27 d.o.f.) in order to find the values that minimize χ^2 function. The results are the correction to the model prediction from MiniBooNE MC. Table 7.5 shows the fit results. The first row shows the fit results of standard fit where all errors included. The rest show the results where cross section model, flux and OM uncertainties excluded and included. Finally the last row shows the fit results of statistical error only.

Since the fractions computed for overall direction and energy the results are the flux average cross section. The fit results, where all errors included in minimizing χ^2 function, are

$$
\begin{aligned}
n_{sig} &= 1.42 \pm 0.37 \\
n_{bkg}^{low-E} &= 1.39 \pm 0.15 \\
n_{bkg}^{high-E} &= 0.89 \pm 0.21 \\
\frac{\chi^2}{d.o.f.} &= \frac{12.48}{27.0}
\end{aligned}
\tag{7.11}
$$

Figure 7.10 illustrate these results into the grid of the fit, the top plot shows the comparison of pre-fit and post-fit (by applying the correction factor), the bottom left shows correlation matrix within the fitting region of direction and energy (first 20 (last 10) rows/columns corresponding to 20 bins (10 bins) of angle in low (high) energy), and the bottom right shows correlation matrix of the fit parameters.

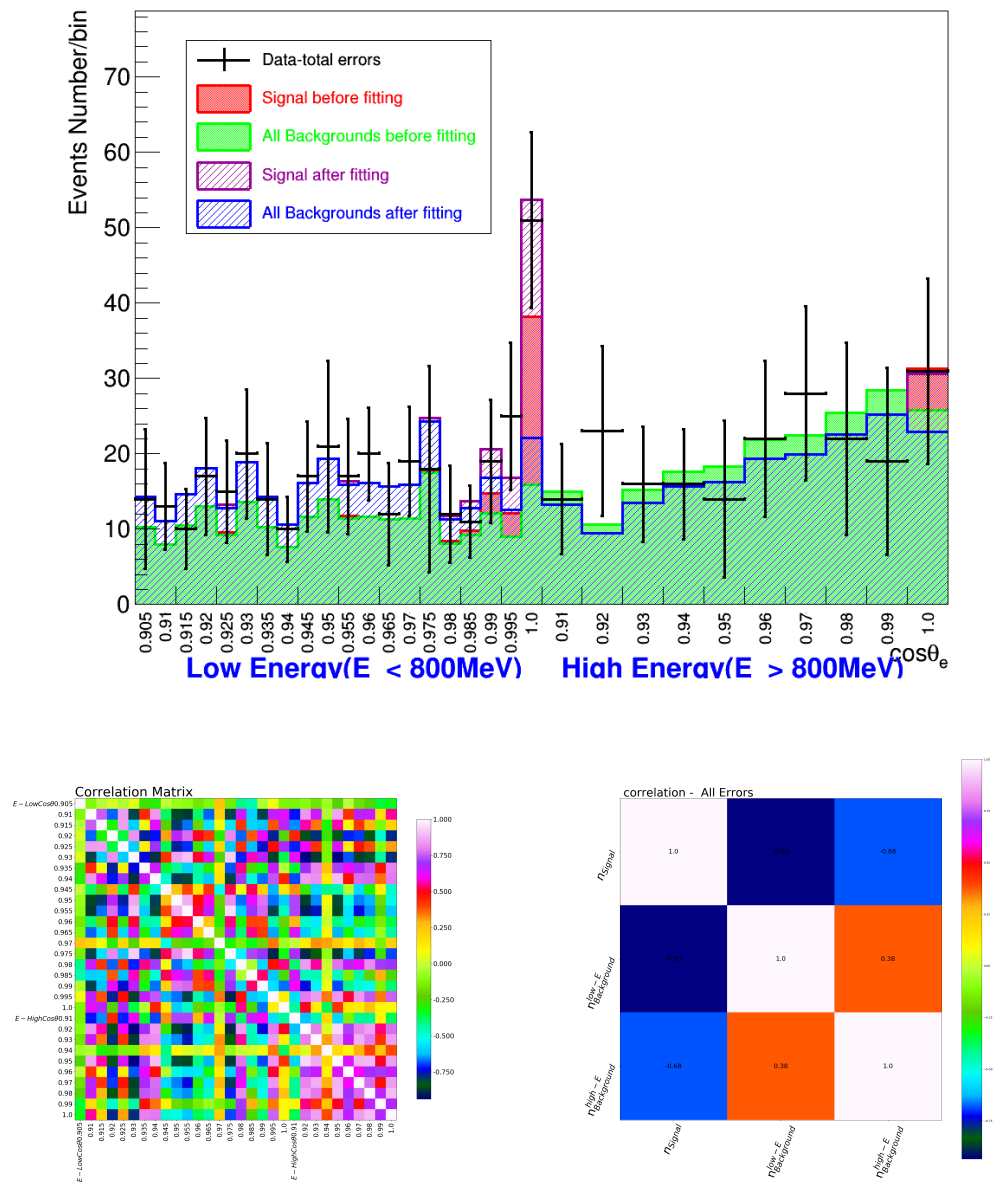

Figure 7.10: The plots for standard fit. The top plot shows data-MC comparison before and after the fit, green (red) stack plot shows background (signal) channels before fit and blue (purple) stack plot shows background (signal) channels after fit, the black line shows the number of data events in each bin with its total error. The bottom left shows the correlation matrix within fitting region of energy-direction. The bottom right shows the correlation between fit parameters.

The confidence ellipse of three fit parameters shows in Figure 7.11, it allows to visualize a 3D confidence interval for one, two and three standard deviation (std). The star shows best fit results is in the center of the ellipse, the circle shows the values expected form standard model, and the cross shows the point where we consider 20% excess coming from oscillation analysis in the background channels. It shows that the results of the fit are $\approx 2\sigma$ from standard model and oscillation excess.

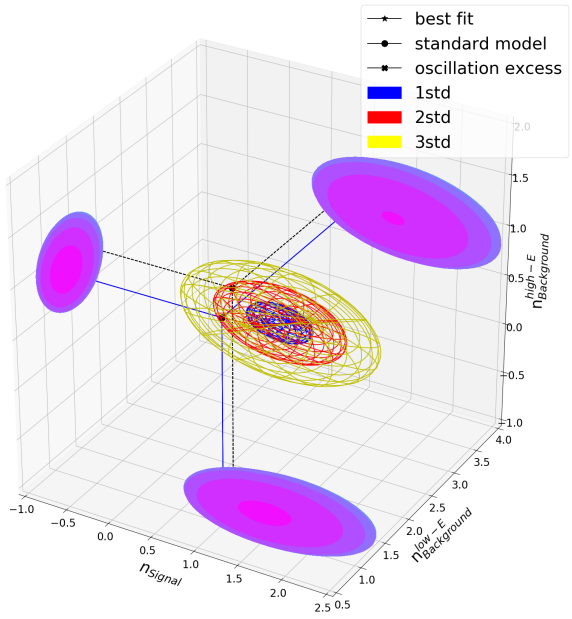

Figure 7.11: The confidence ellipse for three fit parameters (standard fit) with its projection on each plane.

Figure 7.12 to 7.27 (the notations are same as Figure 7.10 and 7.11) illustrate the results of the signal-background fit from first box of Table 7.5 into the grid of the fit with excluding/including each of the most effective error in the fit to estimate the response of the fit with each of the systematic uncertainty in the results.

Looking closely into the Table 7.5 and comparing the results of OM with old and new statistical uncertainty shows there is an unexpected cancelation happening in off diagonal terms of OM matrix when we subtract the old statistical uncertainty and add the new statistical uncertainty based on new POT of data, the errors expected to decrease as a result of more available data while it increases. The strange change in the error proves that we do not consider a perfect correlation in OM covariance matrix, and we need to re-throw OM for the appropriate POT. Also, an other reason of not having the prefect correlation in OM appears in the χ^2 results of the fit, including OM uncertainty in the analysis pulls the χ^2 in a bad way while excluding the OM results in $\frac{\chi^2}{\text{d.o.}f} \approx 1$. Comparing the χ^2 of including the OM uncertainty to excluding it shows that we are overestimating the OM uncertainty in this analysis, it can be fixed by new MC sets with appropriate POT. As we mentioned earlier the OM is not the largest error in this analysis, we believe this approach would be reasonable enough to take the new statistical error into account.

	Signal-Background Fit				Signal-Only Fit		Background-Only Fit		
Uncertainties in analysis	n_{sig}	n_{bkg}^{low-E}	n_{bkg}^{high-E}	χ^2/d.o.f.	n_{sig}	χ^2/d.o.f.	n_{bkg}^{low-E}	n_{bkg}^{high-E}	χ^2/d.o.f.
All errors included	1.42 $\pm$ 0.37	1.39 $\pm$ 0.15	0.89$\pm$ 0.21	12.48/27.0	1.62 $\pm$ 0.37	20.81/29.0	1.42$\pm$0.15	0.90 $\pm$ 0.21	13.75/28.0
Excluding cross section	1.43 $\pm$ 0.37	1.40$\pm$ 0.13	0.89 $\pm$ 0.15	12.79/27.0	1.65 $\pm$ 0.36	23.16/29.0	1.42$\pm$ 0.13	0.88$\pm$ 0.15	14.14/28.0
Excluding flux	1.44$\pm$ 0.36	1.39$\pm$ 0.15	0.90$\pm$ 0.19	12.64/27.0	1.65 $\pm$ 0.35	21.17/29.0	1.44$\pm$ 0.15	0.92$\pm$ 0.19	14.09/28.0
Excluding OM	1.29 $\pm$0.34	1.37 $\pm$0.12	0.85 $\pm$0.20	20.63/27.0	1.60 $\pm$ 0.33	33.66/29.0	1.39 $\pm$ 0.12	0.86$\pm$ 0.20	21.35/28.0
Cross section and stat	1.44 $\pm$0.32	1.32$\pm$0.11	0.94$\pm$ 0.15	24.81/27.0	1.70 $\pm$ 0.31	35.99/29.0	1.36 $\pm$0.11	0.95 $\pm$ 0.15	26.62/28.0
Flux and stat	1.42$\pm$ 0.33	1.32$\pm$ 0.09	0.90$\pm$ 0.13	25.31/27.0	1.69 $\pm$ 0.32	41.18/29.0	1.34 $\pm$ 0.08	0.90 $\pm$ 0.13	26.92/28.0
OM and new-stat	1.53 $\pm$0.35	1.37 $\pm$0.12	0.98 $\pm$0.09	17.33/27.0	1.78 $\pm$ 0.34	26.591/29.0	1.41$\pm$0.12	1.00$\pm$0.09	19.58/28.0
OM and old-stat	1.46 $\pm$0.25	1.35 $\pm$0.09	1.00$\pm$0.07	39.76/27.0	1.71 $\pm$ 0.24	53.72/29.0	1.40 $\pm$0.09	1.03 $\pm$ 0.07	42.98/28.0
Stat ONLY	1.43 $\pm$ 0.32	1.33 $\pm$ 0.08	0.95$\pm$ 0.07	25.75/27.0	1.78 $\pm$ 0.31	42.44/29.0	1.36 $\pm$ 0.08	0.95$\pm$0.07	27.59/28.0

Table 7.5: First box shows the results of signal-background fit with three fit parameters along with showing the results of the fit by excluding/including each systematic uncertainties. The second box shows the results of signal only fit with one fit parameter. The last box shows the results of background only fit with two fit parameters. In each box the last column shows the χ^2 results of the fit compare to the d.o.f.

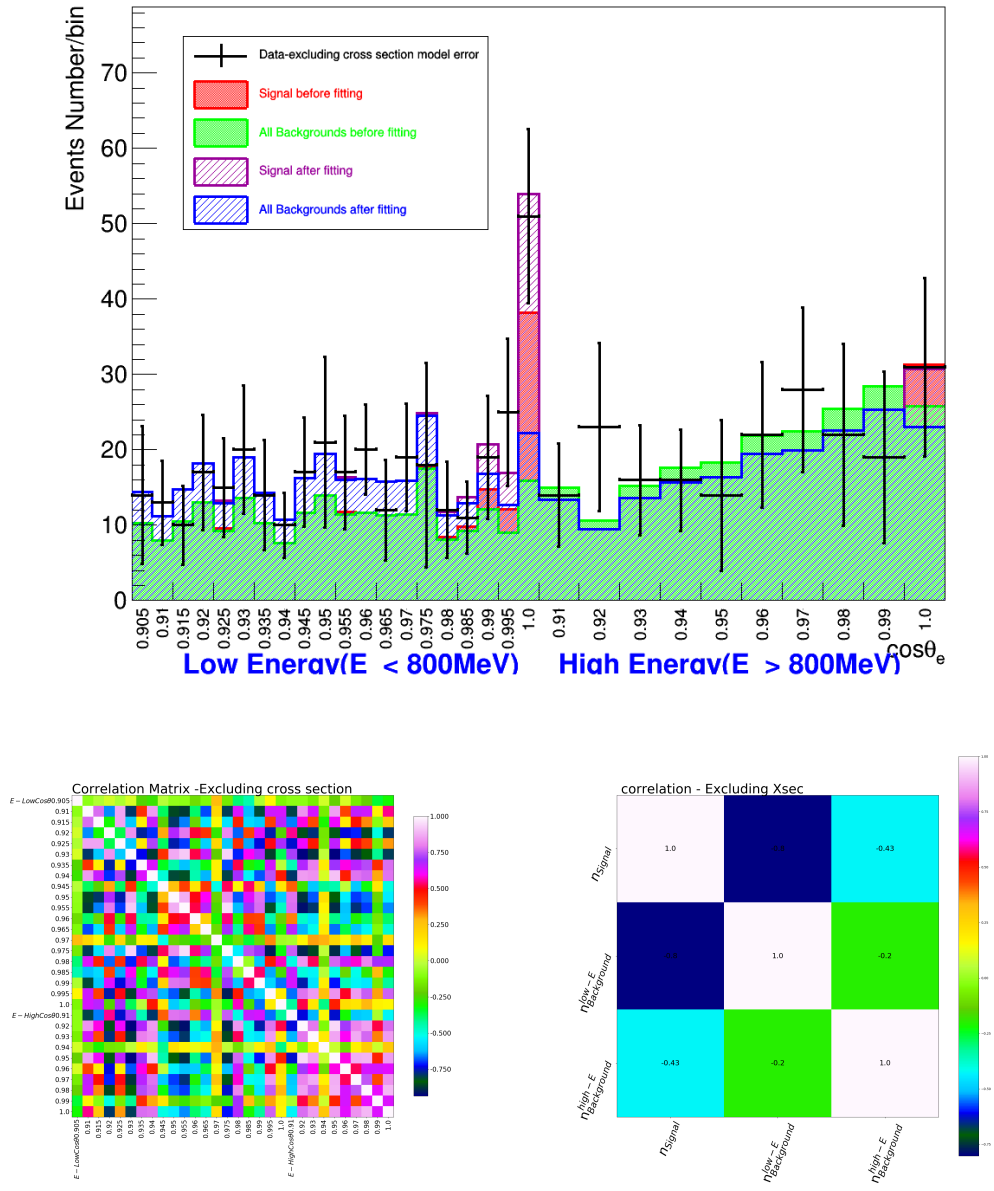

Figure 7.12: The plots with excluding cross section model uncertainties (the notations are same with Figure 7.10).

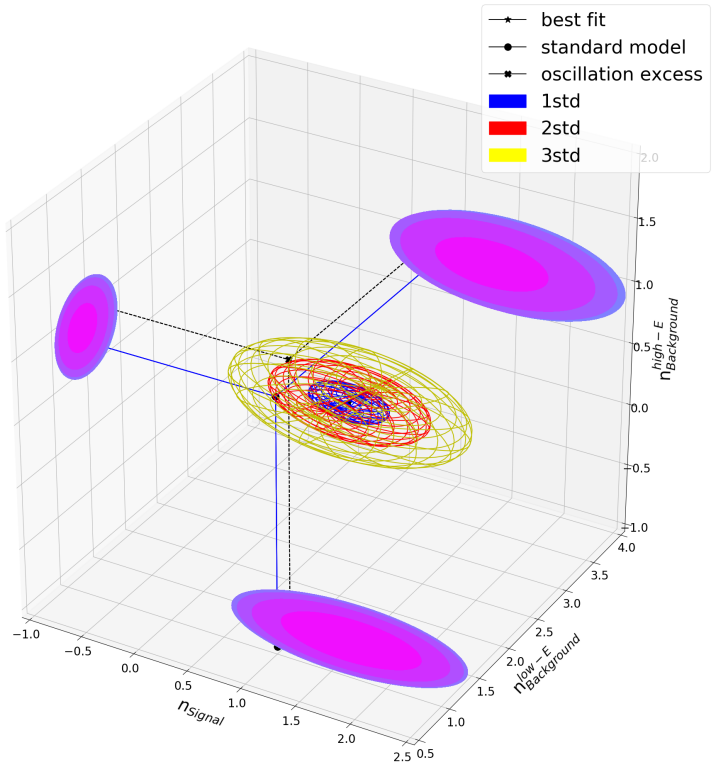

Figure 7.13: The confidence ellipse for three fit parameters (cross section model uncertainty excluded) with its projection on each plane.

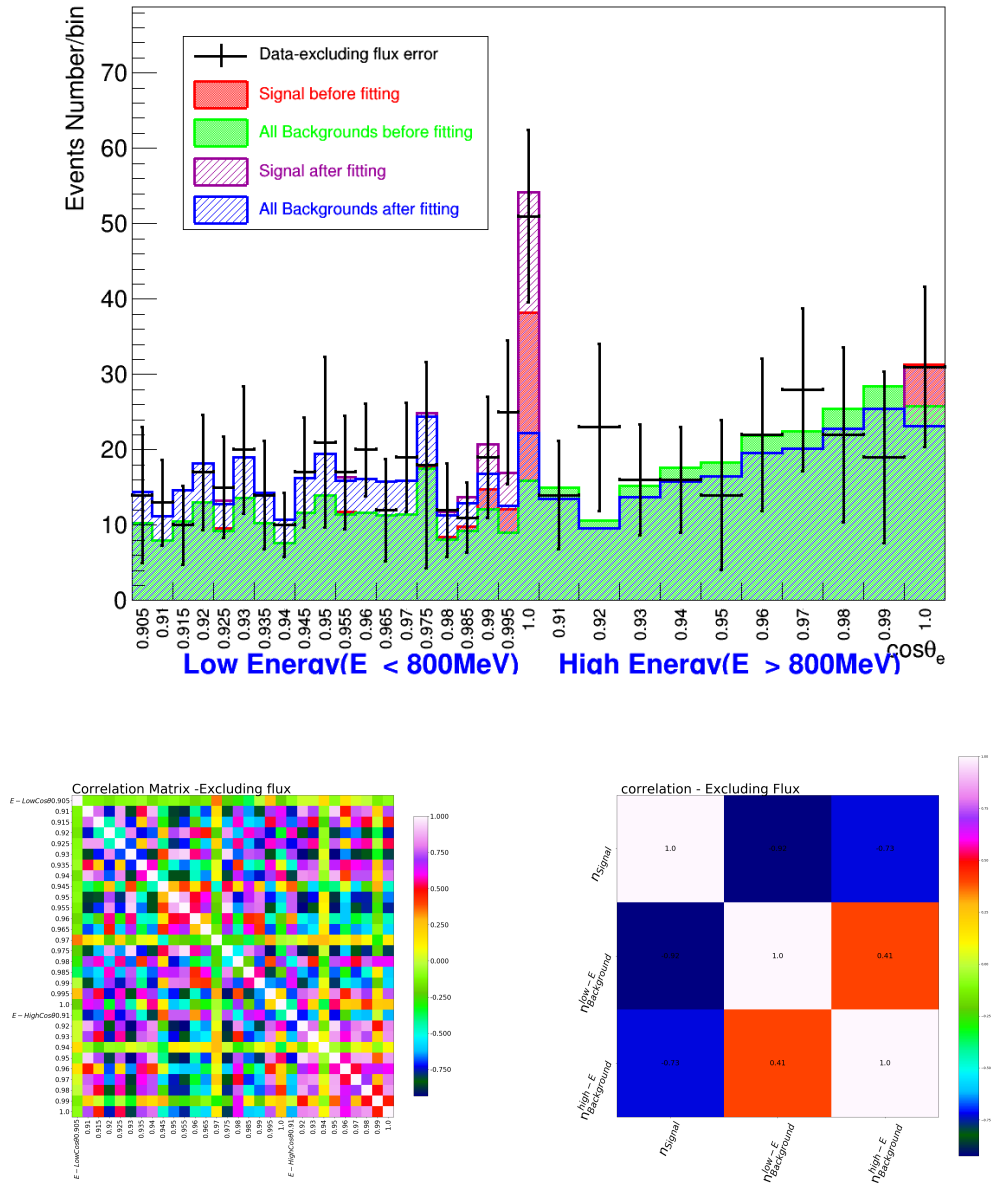

Figure 7.14: The plots with excluding flux uncertainties. (the notations are same with Figure 7.10).

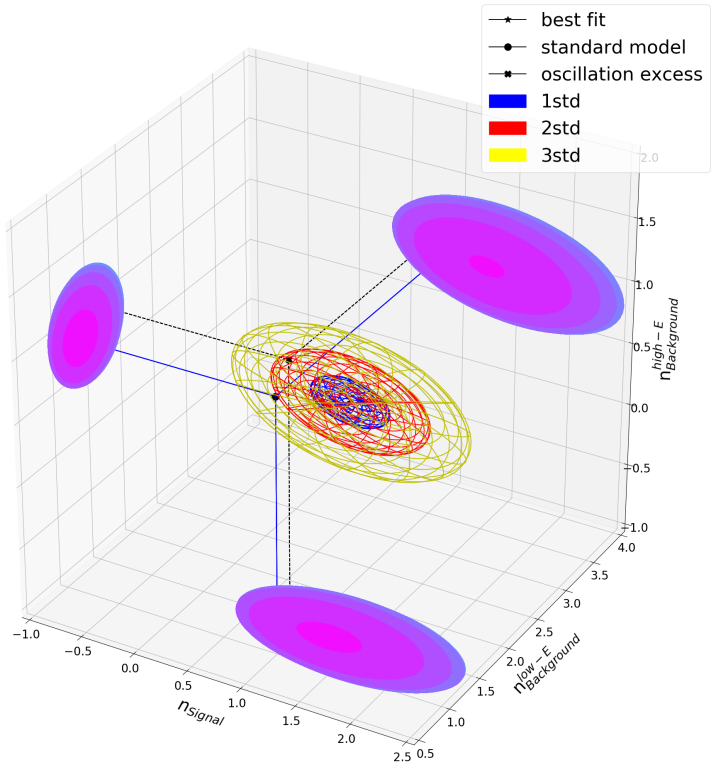

Figure 7.15: The confidence ellipse for three fit parameters (flux uncertainty excluded) with its projection on each plane.

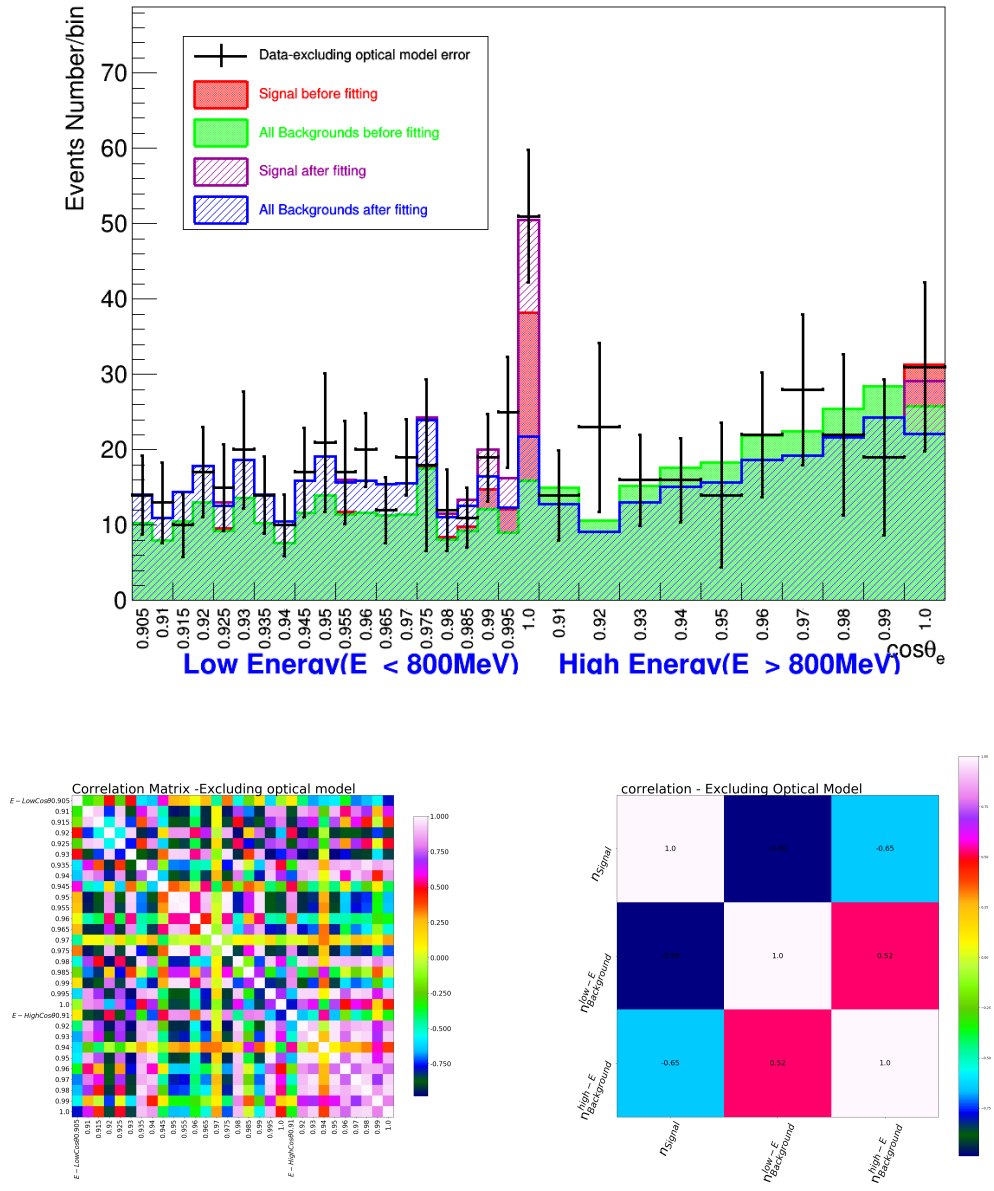

Figure 7.16: The plots with excluding optical model uncertainties (the notations are same with Figure 7.10).

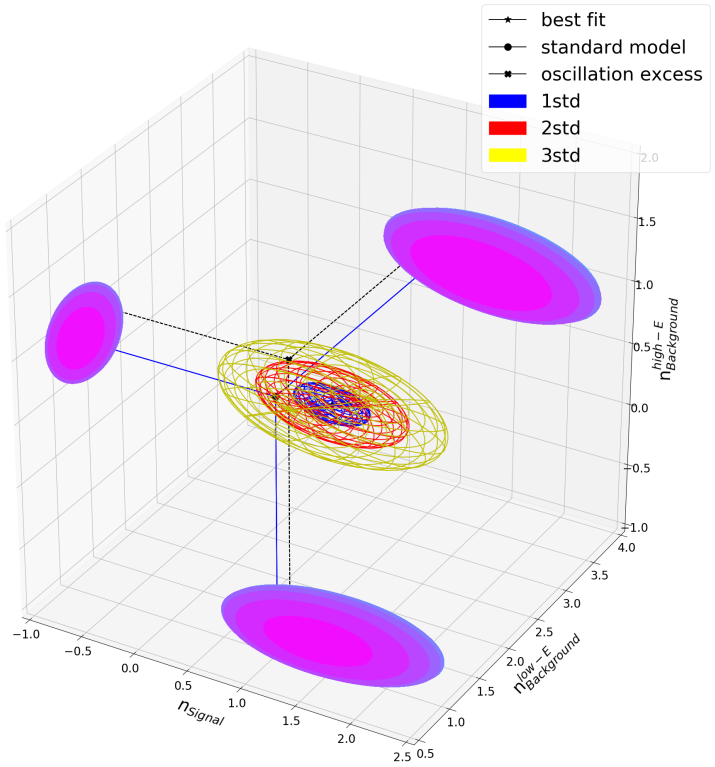

Figure 7.17: The confidence ellipse for three fit parameters (optical model uncertainty excluded) with its projection on each plane.

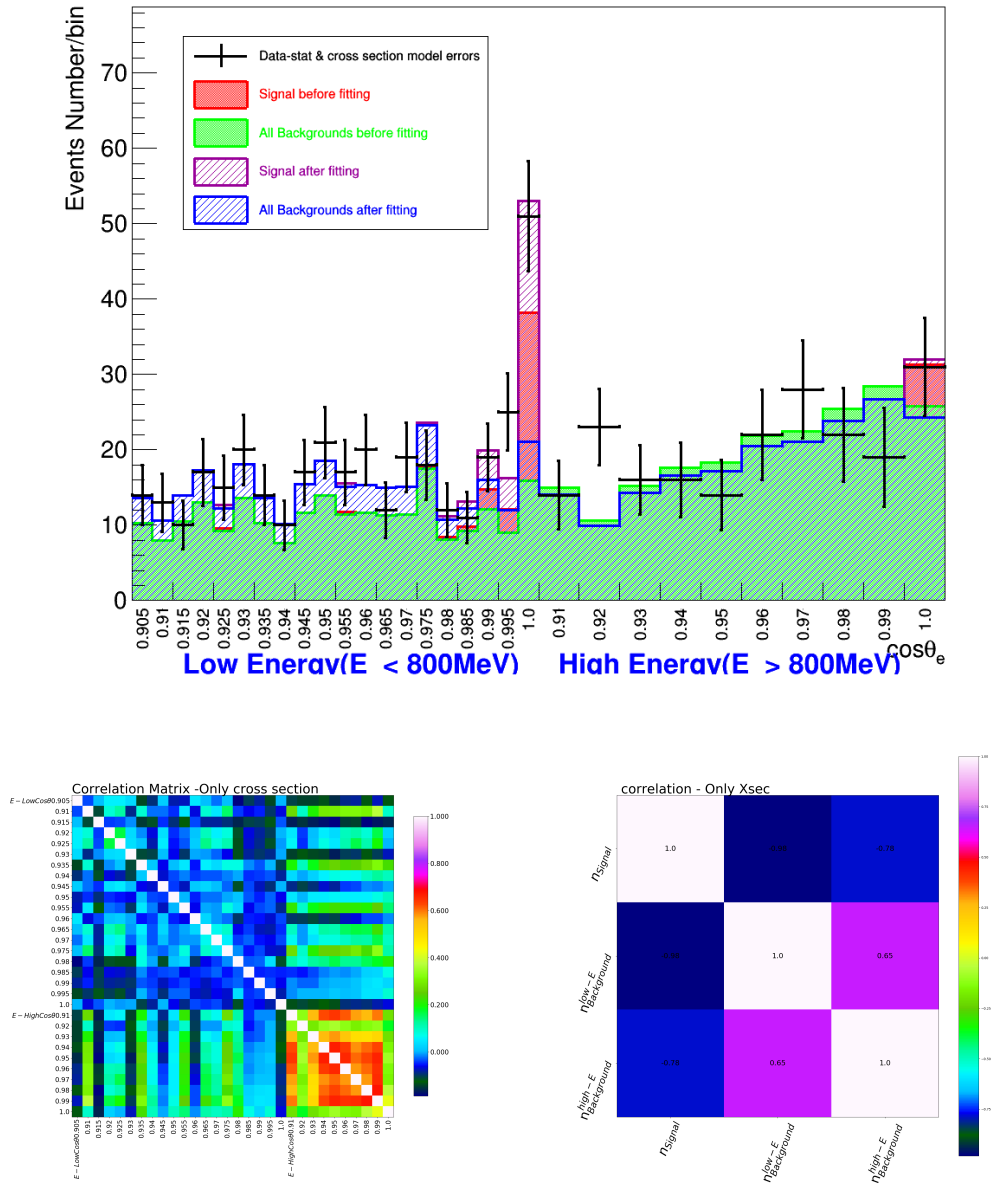

Figure 7.18: The plots with cross section model and statistical uncertainties (the notations are same with Figure 7.10).

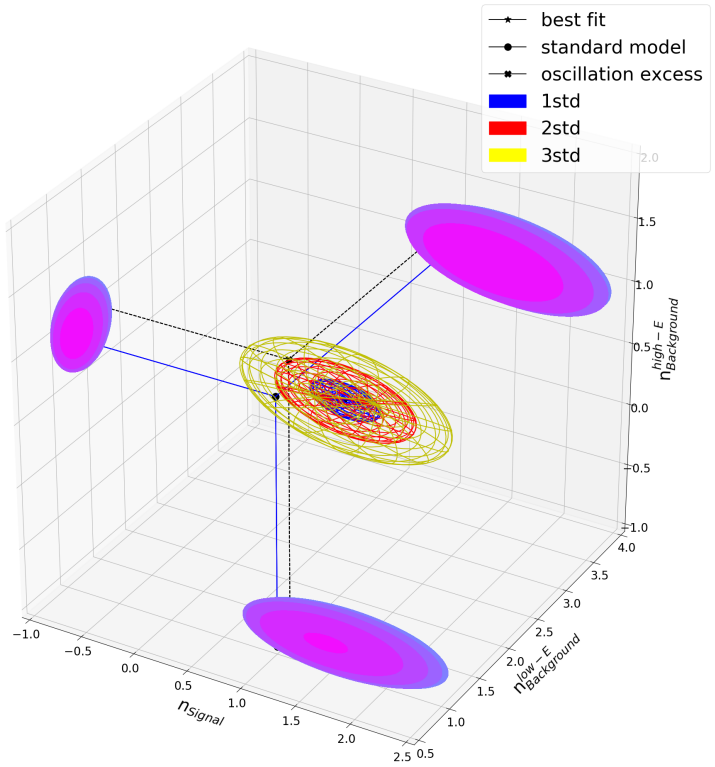

Figure 7.19: The confidence ellipse for three fit parameters (only cross section model and statistical uncertainties included) with its projection on each plane.

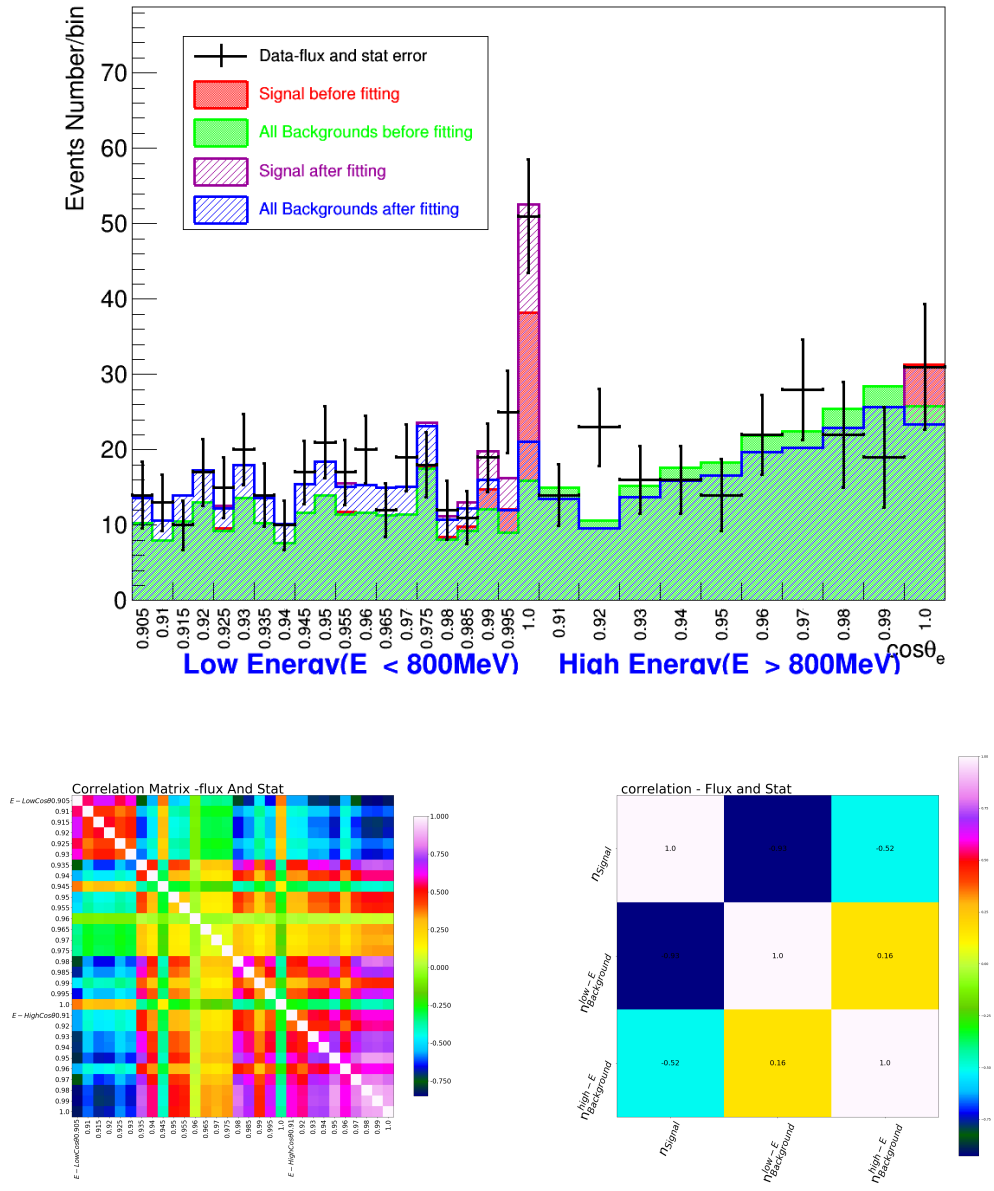

Figure 7.20: The plots with flux and statistical uncertainties (the notations are same with Figure 7.10).

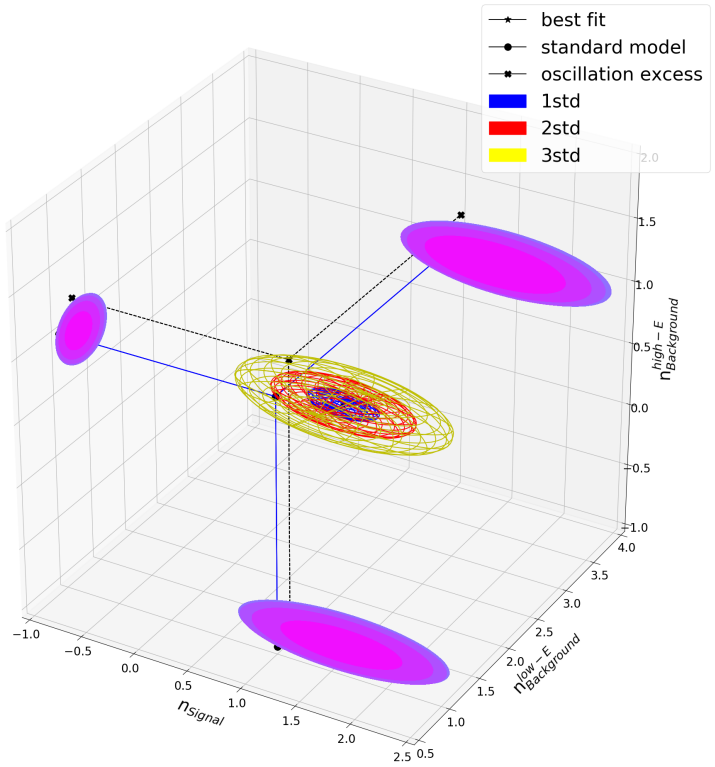

Figure 7.21: The confidence ellipse for three fit parameters (only flux and statistical uncertainties included) with its projection on each plane.

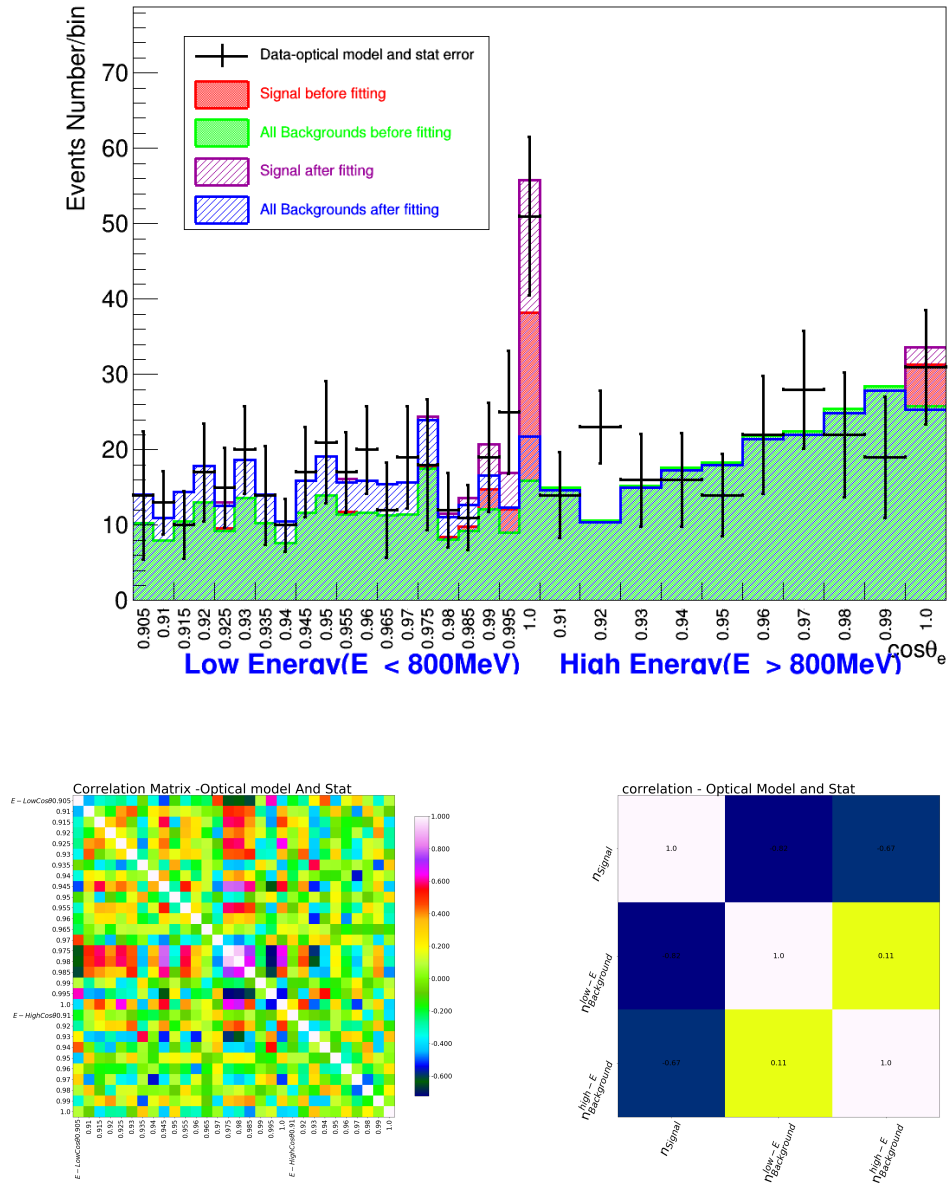

Figure 7.22: The plots with optical model and statistical uncertainties (the notations are same with Figure 7.10).

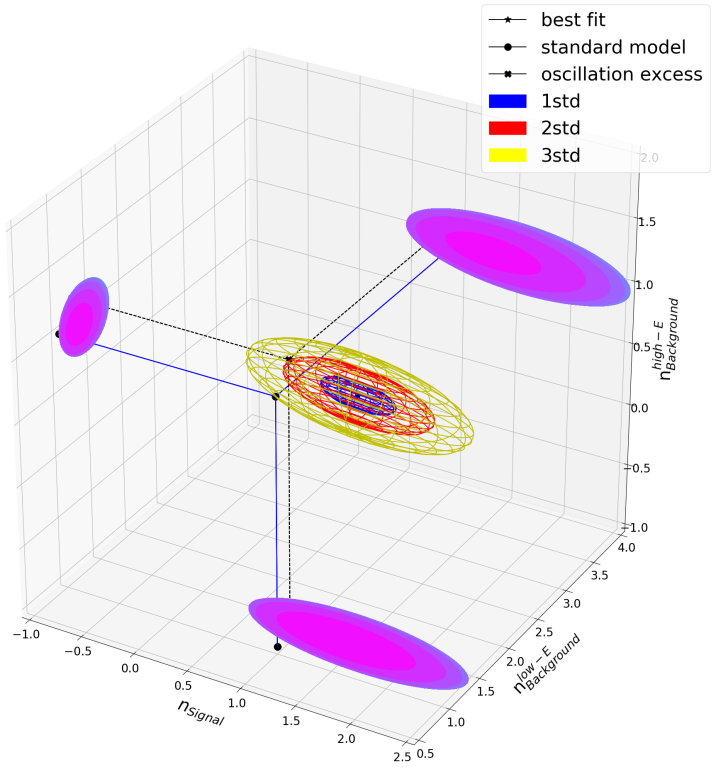

Figure 7.23: The confidence ellipse for three fit parameters (only optical model and new statistical uncertainties included) with its projection on each plane.

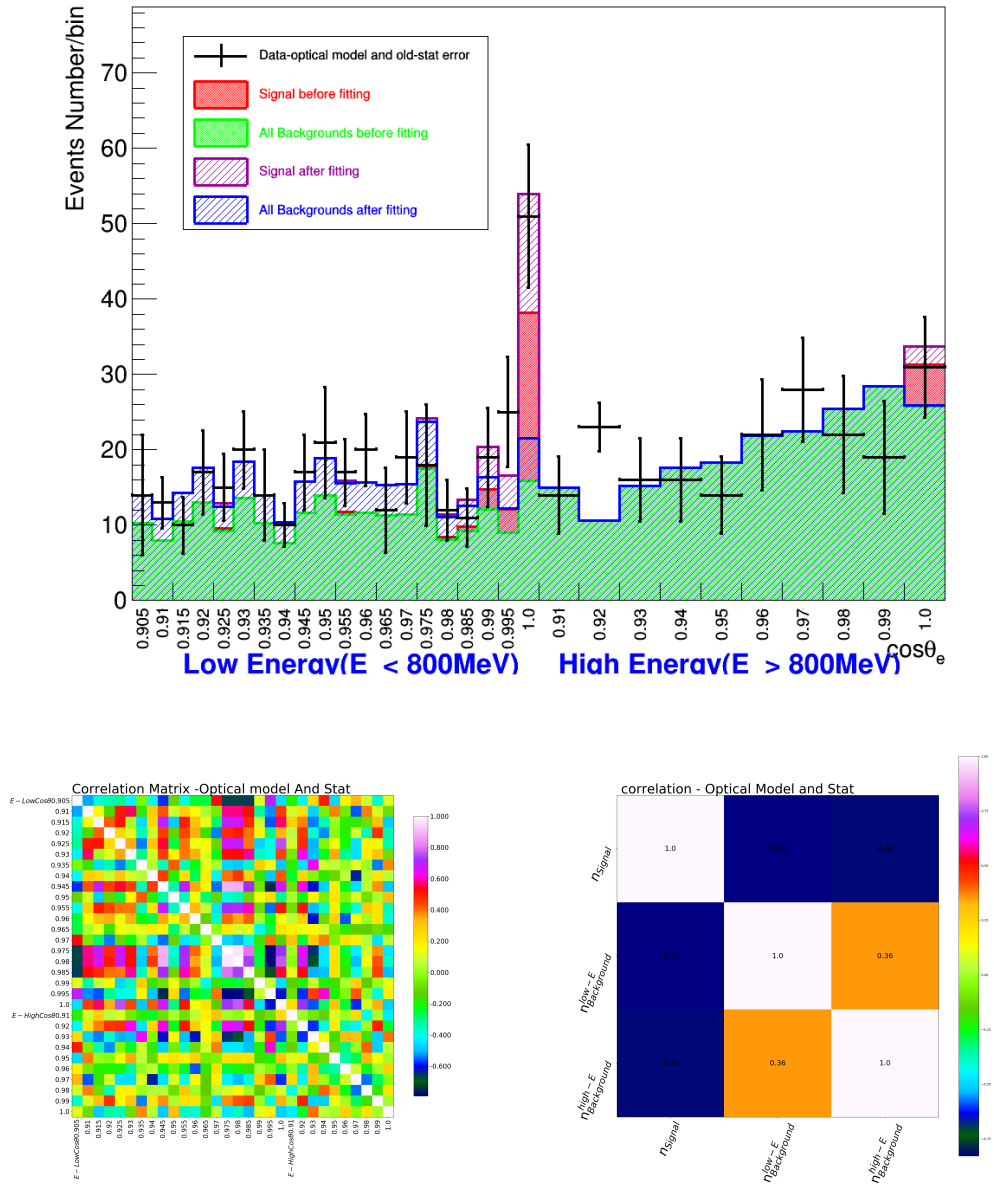

Figure 7.24: The plots with optical model and old statistical uncertainties (the notations are same with Figure 7.10).

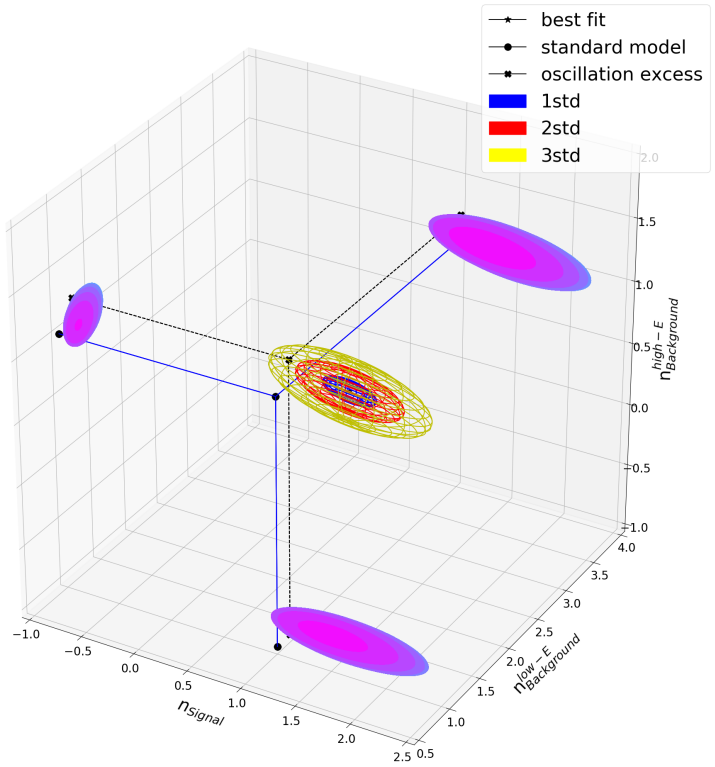

Figure 7.25: The confidence ellipse for three fit parameters (only optical model and old statistical uncertainties included) with its projection on each plane.

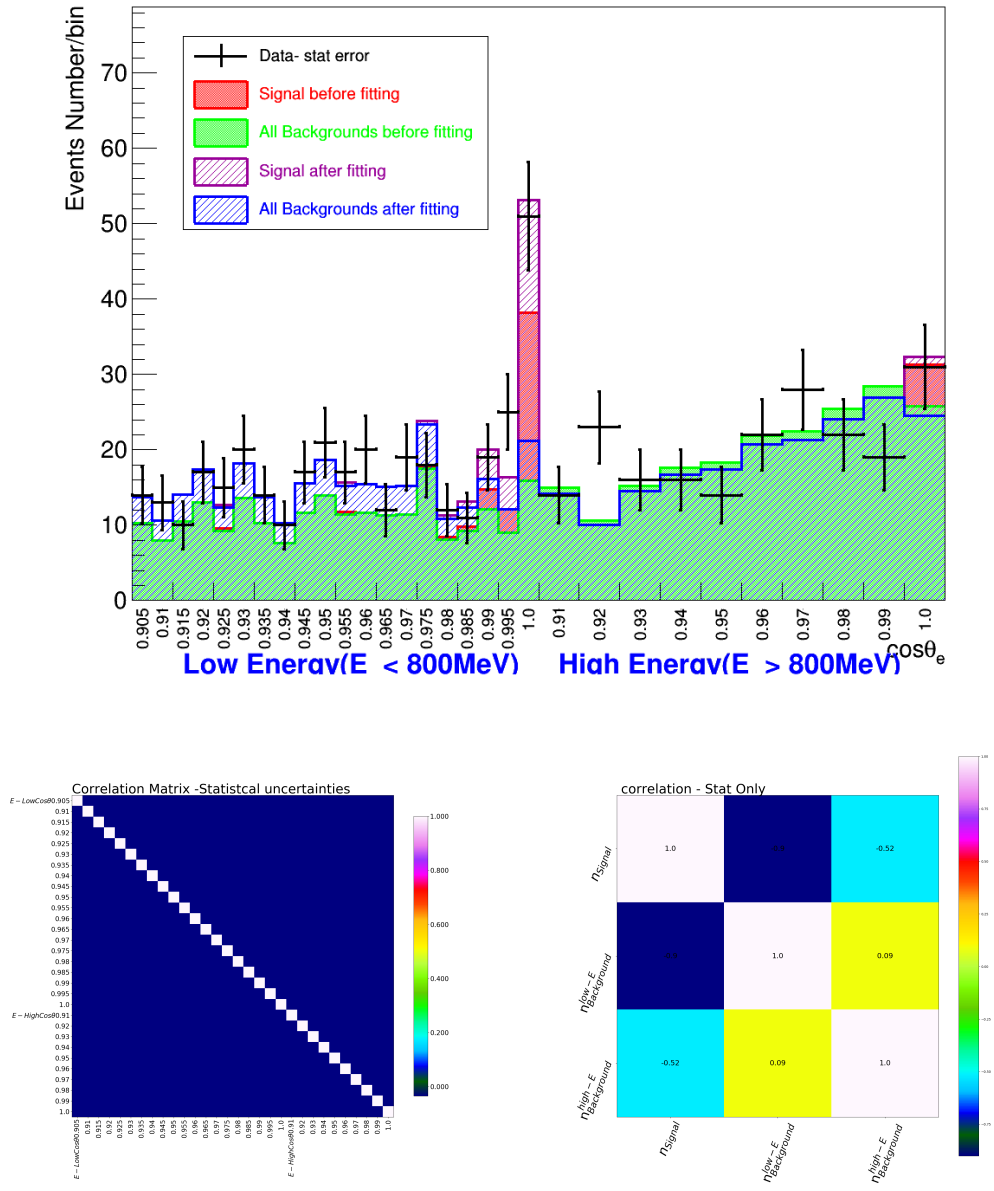

Figure 7.26: The plots with only statistical error (the notations are same with Figure 7.10)

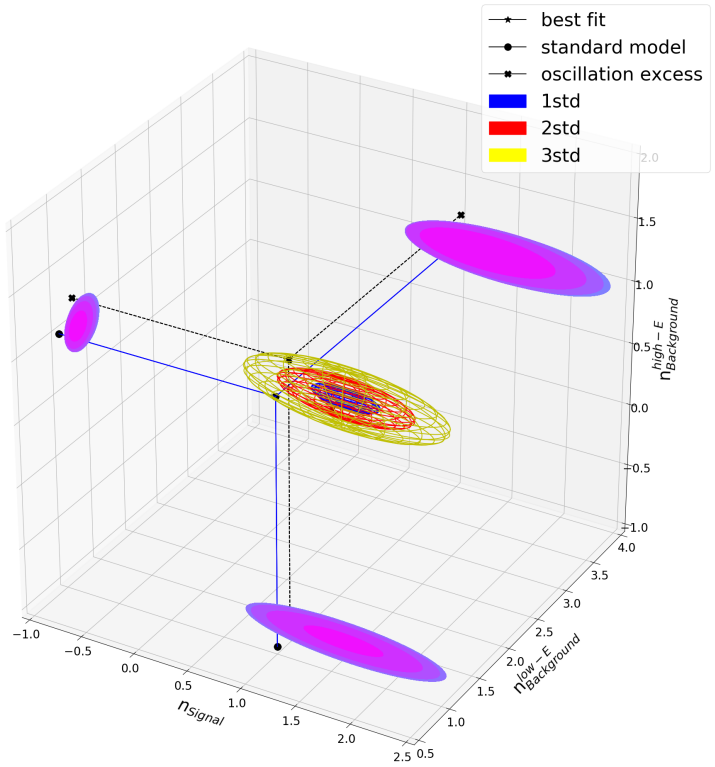

Figure 7.27: The confidence ellipse for three fit parameters (only statistical uncertainty included) with its projection on each plane.

7.5.3 Test Statistic and Probability of Fit

Generating Fake Date

In order to get the estimate of the probability of fit, we need to generate fake data and do the fit on them. The χ^2 cumulative probability distribution of the best fit to fake data results in the probability of the fit. This section presents how the fake data sets are generated.

Fake data is generated around a given central value with corresponding covariance matrix that explain the uncertainty in each bins. The schematic of how to generate fake data shows in Figure 7.28. The covariance matrix is decomposed by Cholesky decomposition [], $M = LL^T$, the result is an upper, or lower triangular matrix. An uncorrelated random number generated from a Gaussian distribution with a mean of zero and a standard deviation of one for each bin in the distribution. Multiplying the triangular matrix by the vector of uncorrelated random numbers results in a correlated random numbers as a vector. Adding the correlated random numbers to the central value distribution produce fake datas. It should be noted that the negative value is set to zero because number of events cannot measure count less than zero. N uncorrelated random numbers vector need to be produced in order to generate N fake data set.

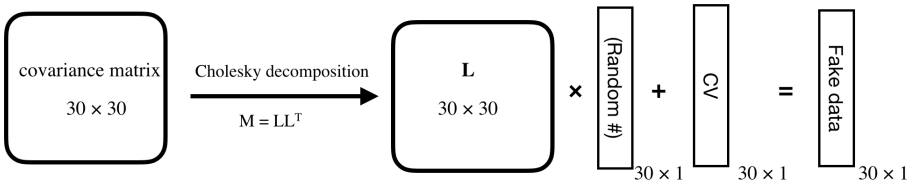

Figure 7.28: Schematic of how to generate fake data

Figure 7.29 shows the cumulative probability distribution for the best fit to fake data, this shows that the probability that the prediction compared to data yields a test statistic of $\frac{12.48}{27}$ is $\approx 20\%$ - fit is good.

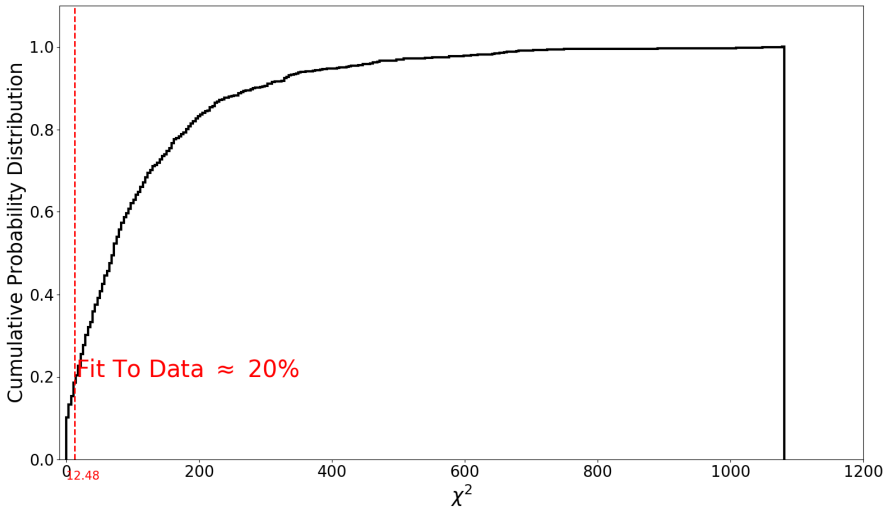

Figure 7.29: The cumulative probability distribution for best fit to fake data sets.

7.6 Conclusion

One of the primary goal of the neutrino experiments is to test the three neutrino flavor model by obtaining high-precision values of the neutrino oscillation parameters. Since both the neutrino energy and oscillation length can be relatively well controlled in accelerator-based neutrino experiments it plays a crucial role in testing the oscillation model. However, there is a inadequacy of neutrino cross section information in the energy region important for accelerator-based neutrino experiments.

This study is the first time measurement of the electron elastic scattering cross section in MiniBooNE, providing important information about the electron neutrino scattering cross section in carbon. The standard fit results in the correction factor of NUANCE electron neutrino elastic scattering cross section. Table 3.4 is given the values of total electron neutrino elastic scattering cross section, considering the correction factor coming from this study on the signal channel ($\nu_\mu e^-$ elastic scattering) the cross section in MiniBooNE detector is

$$\sigma(\nu_\mu e^- \rightarrow \nu_\mu e^-) = (2.13 \pm 0.55(stat. + syst.)) \times 10^{-45} E_\nu \; cm^2/CH_2 \; MeV. \tag{7.12}$$

in comparison to the previous cross section measurement of this channel (Table 3.5), the result is in the same range of the CHARM (SPS) experiment. It should be noted that the uncertainty due to optical properties of the detector at this point is the best estimate and it will improve by the MC throws that explain the new data sets.

Also this channel is the cleanest channels of the neutrino scattering, and can contribute to the check for the flux measurement in general.

In addition, as it mentioned earlier MiniBooNE facilitated a dedicated light dark matter search with a special off-target run. In order to measure the electron scattering from dark matter the well understanding of its background channels is needed. The electron neutrino scattering is one of the most dominated background in electron DM analysis. This complete measurement of the cross section, where all the systematics associated with the data and the detector included, furnishes

the study on the electron dark matter scattering as the next analysis. The electron DM scattering has the same characteristic with the interaction to this channel, the only difference is the time delay of massive DM compare to neutrino with tiny mass. Now then by adding the timing cut DM can be distinguished from neutrino interaction.

References

[1] E. Church *et al.*, "A letter of intent for an experiment to measure $\nu_\mu \rightarrow \nu_e$ oscillations and nu/mu disappearance at the fermilab booster," *BooNE*, 1997.

[2] L. Bartoszek, *http://www.bartoszekeng.com*, Bartoszek Engineering.

[3] A. Aguilar-Arevalo *et al.*, "Nuclear instruments and methods in physics research section a: Accelerators, spectrometers, detectors and associated equipment," *BooNE*, vol. 559, pp. 28–46, 2009.

[4] I. Stancu *et al.*, "Technical design report for the MiniBooNE neutrino beam," *BooNE*, 2001.

[5] R. Amlay, W. Metcalf, A. Bazarko, and O. Wascko, "The calibration systems for the MiniBooNE experiment," *MiniBooNE Technical Note*, 2004.

[6] R. Patterson, "A search for muon neutrino to electron neutrino oscillations at $m^2 > 1ev$," Ph.D. dissertation, Princeton University, 2007.

[7] A. A. Aguilar-Arevalo and others., "The neutrino flux prediction at MiniBooNE," *Phys. Rev. Letter*, vol. D79, 2009.

[8] J. Beringer *et al.*, "Review of particle physics," *Phys. Rev.*, vol. D86, p. 010001, 2012.

[9] S. Weinberg, "A model of Lepton," *Phys. Lett.*, vol. 19, pp. 1264–1266, 1967.

[10] C. Quigg, "Nature's greatest puzzles," *eConf*, vol. C040802, p. L001, 2004.

[11] S. Chatrchyan *et al.*, "Observation of a new boson at a mass of $125\ GeV$ with the CMS experiment at the LHC," *Phys. Lett.*, vol. B716, 2012.

[12] G. Aad *et al.*, "Observation of a new particle in the search for the SM Higgs boson with the ATLAS detector at the LHC," *Phys. Lett.*, vol. B716, 2012.

[13] F. Zwicky, "Die Rotverchiebung von extraglaktischen," *Phys. Acta*, vol. 110, 1933.

[14] S. Smith, "The mass of the Virgo Cluster," *Astrophysical Journal*, vol. 83, 1936.

[15] W. Pauli, "Letter to the physical society of Tubingen/ Dear radioactive ladies and gentlemen," *Physics Today*, vol. 31N9, p. 27, 1930 / 1978.

[16] F. Reines and L. Cowan, "A proposed experiment to detect the free neutrino," *Phys. Rev. Letter*, vol. 492, 1953.

[17] G. Danby *et al.*, "Observation of high-energy neutrino reactions and the existence of two kinds of neutrinos," *Phys. Rev. Letter*, vol. 36, 1962.

[18] D. Collaboration, "Observation of Tau neutrino interactions," *Phys. Rev. Letter*, vol. B504, 2000.

[19] G. Fogli, E. Lisi, D. Montanino, and G. Scioscia, "Neutrino oscillations. a phenomenological overview," *Nucl. Phys. Proc. Suppl*, vol. 66, pp. 315–334, 1998.

[20] J. Bahcall, "Solar neutrinos," *Phys. Rev. Letter*, vol. 12, pp. 300–302, 1964.

[21] K. Hirata *et al.*, "Experimental study of the atmospheric neutrino flux," *Phys. Lett.*, vol. B205, p. 416, 1988.

[22] Y. Fukuda *et al.*, "Measurement of a small atmospheric muon-neutrino / electron-neutrino ratio," *Phys. Lett.*, vol. B433, pp. 9–16, 1998.

[23] Q. Ahmad *et al.*, "Direct evidence for neutrino flavor transformation from neutral current interactions in the Sudbury neutrino observatory," *Phys. Rev. Letter*, vol. 89, p. 011301, 2002.

[24] M. Ahn *et al.*, "Measurement of neutrino oscillation by the K2K experiment," *Phys. Rev.*, vol. D74, p. 072003, 2006.

[25] D. Michael *et al.*, "Observation of muon neutrino disappearance with the MINOS detectors and the NuMI neutrino beam," *Phys. Rev. Letter*, vol. 97, p. 191801, 2006.

[26] E. Majoranal, "Teoria simmetrica dell-elettrone e del positrone (in italian)," *Nuovo Cimento*, vol. 14, p. 171, 1937.

[27] J. Hill, "Results from the LSND neutrino oscillation search," *Phys. Rev. Letter*, vol. 75, 1995.

[28] B. Batell, M. Pospelov, and A. Ritz, "Exploring portals to a hidden sector through fixed targets," *Phys. Rev.*, vol. D80, 2009.

[29] R. Thornton, "Search for light dark matter produced in a proton beam dump," Ph.D. dissertation, Indiana University, 2017.

[30] T. D. Lee and C. N. Yang, "Question of parity conservation in weak interactions," *Phys. Rev*, vol. 104, pp. 254–258, 1956.

[31] C. S. Wu, E. Ambler, W. Hayward, Hoppes, and R. P. Hudson, "Experimental test of parity conservation in beta decay," *Phys. Rev.*, vol. 105, pp. 1413–1414, 1957.

[32] E. C. G. Sudarshan and R. E. Marshak, "Chirality invariance and the universal fermi interaction," *Phys. Rev.*, vol. 109, pp. 1860–1861, 1958.

[33] R. P. Feynman and M. Gell-Mann, "Theory of the fermi interaction," *Phys. Rev.*, vol. 109, pp. 193–198, 1958.

[34] S. Eidelman *et al.*, "Review of particle physics. particle data group," *Phys. Lett.*, vol. B592, 2004.

[35] J. Gargamelle collab. (Blietschau and others), "Evidence for the leptonic neutral current reaction," *Nucl. Phys.*, vol. B114, p. 189, 1976.

[36] H. Faissner *et al.*, "Muon-neutrino electron scattering," *Phys. Rev*, vol. D41, p. 213, 1978.

[37] R. H. Heisterberg *et al.*, "Evidence for the leptonic neutral current reaction," *Phys. Lett.*, vol. 44, p. 635, 1980.

[38] A. M. Cnops *et al.*, "Na," *Phys. Rev. Lett.*, vol. 41, p. 367, 1978.

[39] J. CHARM collab. (Dorenbosch and others), "Na," *Zeitschrift fr Physik*, vol. C41, p. 567, 1989.

[40] L. A. Ahrens *et al.*, "Na," *Phys. Rev.*, vol. D41, p. 3297, 1990.

[41] C.-R. Collab., "Na," *Phys. Lett.*, vol. B281, p. 159, 1992.

[42] R. C. Allen, "Na," *Phys. Rev.*, vol. D47, p. 11, 1992.

[43] CERN, "Detector description and simulation tool," *CERN Program Library Long Writeup*, vol. W5013, 1993.

[44] R. A. Johnson, "MiniBooNE mineral oil: Technical specification," *BooNE*, 2001.

[45] J. Raff, R. Hawker, A. Bazarko, G. Garvey, *et al.*, "Mineral oil tests for the MiniBooNE detector," *Nucl. Sci.*, vol. 49, pp. 957–962, 2002.

[46] Hamamatsu, "http://www.hamamatsu.com," .

[47] B. T. Fleming *et al.*, "Inner structure and outer limits: Precision QCD and electroweak tests from neutrino experiments," Ph.D. dissertation, Columbia University, 2002.

[48] R. B. Patterson, "The PMT charge calculation," *BooNE Technical Note 83*, 2003.

[49] J. B. Birks, "The theory and practice of scintillation counting," *Macmillan, New York*, 1964.

[50] R. L. Craun and D. L. Smith, "Mineral oil tests for the MiniBooNE detector," *Nucl. Sci.*, 1970.

[51] A. Bazarko *et al.*, "Studies of scattering in Marcol7 mineral oil," *MiniBooNE Technical Note, Note, no. TN 144*, 1998.

[52] D. Toptygin, "Time-resolved fluorescence of MiniBooNE mineral oil,," *MiniBooNE Technical Note*, 2004.

[53] A. Bazarko *et al.*, "Studies of scattering in Marcol 7 mineral oil," *MiniBooNE Technical Note*, 2004.

[54] I. Stancu, "Maximum likelihood event reconstruction algorithms in boone," *BooNE Technical Note 5, 6, 18, 21, 36, 50*, 1998-2002.

[55] A. A. Aguilar-Arevalo *et al.*, "A search for electron neutrino appearance at the delta m**2 1 ev**2 scale," *Phys. Rev. Lett.*, 2007.

[56] ——, "Oscillation sensitivity in MiniBooNE," *Phys. Rev. Lett.*, 2007.

[57] D. Casper, "NUANCE generator," *Nucl. Phys. Proc. Suppl*, 2002, http://nuint.ps.uci.edu/nuance/.

[58] S. Agostinellietal, "GEANT4 generator," *Nucl.Inst. Meth.A506:250*, 2003, http://wwwasd.web.cern.ch/wwwasd/geant4/G4Users.

[59] M. Sorel, "Search for sterile neutrinos using the MiniBooNE beam," Ph.D. dissertation, Columbia University, 2005.

[60] C. H. Llewellyn Smith, "Neutrino reactions at accelerator energies," *Phys. Rep.*, vol. 3C, pp. 261–379, 1972.

[61] D. Rein and S. L. M., "Neutrino reactions at accelerator energies," *Ann. Phys. (NY)*, vol. 133, pp. 79–153, 1981.

[62] A. Bodek, I. Park, and U. K. Yang, "Improved low Q^2 model for neutrino and electron nucleon cross sections in few GeV region," *Nucl. Phys. Proc. Suppl*, vol. 139, p. 133, 2002.

[63] H. S. Budd, A. Bodek, and J. Arrington, "Modeling Quasi-elastic form-factors for electron and neutrino scattering," *arXiv:hep-ex/0308005l*, 2003.

[64] A. Aguilar-Arevalo *et al.*, "First measurement of the Muon Neutrino charged current Quasi-elastic double differential cross section," *Nucl. Phys. Proc. Suppl*, vol. D81, 2010.

[65] ——, "First observation of coherent π^0 production in neutrino nucleus interactions with $E_\nu < 2GeV$," *Phys. Rev.*, vol. B664, 2008.

[66] ——, "A search for electron neutrino appearance at the $\delta m^2 \approx 1ev^2$ scale," *Phys. Rev. Letter*, vol. 98, 2007.

[67] C. Athanassopoulos *et al.*, "Results from the LSND neutrino oscillation search," *Nucl. Inst. and Meth*, vol. A388, 1997.

[68] A. Aguilar-Arevalo *et al.*, "Event excess in the MiniBooNE search for $\bar{\nu}_\mu \rightarrow \bar{\nu}_e$ oscillations," *Phys. Rev. Letter*, vol. 105, 2010.

[69] R. Dharmapalan, "Antineutrino Neutral Current Interactons in MiniBooNE," Ph.D. dissertation, TUSCALOOSA, ALABAMA University, 2012.

[70] D. Schmitz, "A measurement of hadron production cross sections for the simulation of accelerator neutrino beams and a search for $\bar{\nu}_\mu \rightarrow \bar{\nu}_e$ oscillations in the $\delta m^2 \approx 1ev^2$ region," Ph.D. dissertation, Columbia University, 2008.